UNIVERSIDAD DE INVESTIGACIÓN DE TECNOLOGÍA EXPERIMENTAL YACHAY

Escuela de Ciencias Físicas y Nanotecnología

TÍTULO: Antibacterial Properties of Silver Triangular Nanoplates deposited on Graphene Oxide

Trabajo de integración curricular presentado como requisito para la obtención
del título de Ingeniería en Nanotecnología

Autor:

Benalcázar Jaramillo Joselyn Synei

Tutor: Ph.D. Sarah Briceño
Co-tutor: Ph.D. Julio C. Chacón-Torres

Ingeniería en Nanotecnología - Benalcázar Jaramillo Joselyn

Urcuquí, Julio 2020

SECRETARÍA GENERAL
(Vicerrectorado Académico/Cancillería)
ESCUELA DE CIENCIAS FÍSICAS Y NANOTECNOLOGÍA
CARRERA DE NANOTECNOLOGÍA
ACTA DE DEFENSA No. UITEY-PHY-2020-00004-AD

A los 8 días del mes de abril de 2020, a las 15:00 horas, de manera virtual mediante videoconferencia, y ante el Tribunal Calificador, integrado por los docentes:

Presidente Tribunal de Defensa	Dr. ZAMORA LEDEZMA , CAMILO , Ph.D.
Miembro No Tutor	Dra. LOPEZ GONZALEZ, FLORALBA AGGENY , Ph.D.
Tutor	Dra. BRICEÑO ARAUJO, SARAH ELISA , Ph.D.

El(la) señor(ita) estudiante **BENALCAZAR JARAMILLO, JOSELYN SYNEI**, con cédula de identidad No. **1003418314**, de la **ESCUELA DE CIENCIAS FÍSICAS Y NANOTECNOLOGÍA**, de la Carrera de **NANOTECNOLOGÍA**, aprobada por el Consejo de Educación Superior (CES), mediante Resolución **RPC-SO-13-No.156-2015**, realiza a través de videoconferencia, la sustentación de su trabajo de titulación denominado: **Antibacterial Properties of Silver Triangular Nanoplates deposited on Graphene Oxid**, previa a la obtención del título de **INGENIERO/A EN NANOTECNOLOGÍA**.

El citado trabajo de titulación, fue debidamente aprobado por el(los) docente(s):

Tutor	Dra. BRICEÑO ARAUJO, SARAH ELISA , Ph.D.

Y recibió las observaciones de los otros miembros del Tribunal Calificador, las mismas que han sido incorporadas por el(la) estudiante.

Previamente cumplidos los requisitos legales y reglamentarios, el trabajo de titulación fue sustentado por el(la) estudiante y examinado por los miembros del Tribunal Calificador. Escuchada la sustentación del trabajo de titulación a través de videoconferencia, que integró la exposición de el(la) estudiante sobre el contenido de la misma y las preguntas formuladas por los miembros del Tribunal, se califica la sustentación del trabajo de titulación con las siguientes calificaciones:

Tipo	Docente	Calificación
Presidente Tribunal De Defensa	Dr. ZAMORA LEDEZMA , CAMILO , Ph.D.	9,4
Miembro Tribunal De Defensa	Dra. LOPEZ GONZALEZ, FLORALBA AGGENY , Ph.D.	10,0
Tutor	Dra. BRICEÑO ARAUJO, SARAH ELISA , Ph.D.	10,0

Lo que da un promedio de: **9.8 (Nueve punto Ocho)**, sobre 10 (diez), equivalente a: **APROBADO**

Para constancia de lo actuado, firman los miembros del Tribunal Calificador, el/la estudiante y el/la secretario ad-hoc.

Certifico que *en cumplimiento del Decreto Ejecutivo 1017 de 16 de marzo de 2020, la defensa de trabajo de titulación (o examen de grado modalidad teórico práctica) se realizó vía virtual, por lo que las firmas de los miembros del Tribunal de Defensa de Grado, constan en forma digital.*

BENALCAZAR JARAMILLO, JOSELYN SYNEI
Estudiante

Dr. ZAMORA LEDEZMA , CAMILO , Ph.D.
Presidente Tribunal de Defensa
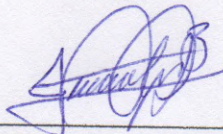
Dra. BRICEÑO ARAUJO, SARAH ELISA , Ph.D.
Tutor

Dra. LOPEZ GONZALEZ, FLORALBA AGGENY , Ph.D.
Miembro No Tutor

CIFUENTES TAFUR, EVELYN CAROLINA
Secretario Ad-hoc

AUTORÍA

Yo, **JOSELYN SYNEI BENALCÁZAR** , con cédula de identidad 100341831-4, declaro que las ideas, juicios, valoraciones, interpretaciones, consultas bibliográficas, definiciones y conceptualizaciones expuestas en el presente trabajo; así cómo, los procedimientos y herramientas utilizadas en la investigación, son de absoluta responsabilidad de el/la autora (a) del trabajo de integración curricular. Así mismo, me acojo a los reglamentos internos de la Universidad de Investigación de Tecnología Experimental Yachay.
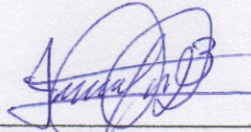
Urcuquí, Julio 2020.

Joselyn Synei Benalcázar Jaramillo
CI:100341831-4

AUTORIZACIÓN DE PUBLICACIÓN

Yo, **JOSELYN SYNEI BENALCÁZAR JARAMILLO,** con cédula de identidad 100341831-4, cedo a la Universidad de Investigación de Tecnología Experimental Yachay, los derechos de publicación de la presente obra, sin que deba haber un reconocimiento económico por este concepto. Declaro además que el texto del presente trabajo de titulación no podrá ser cedido a ninguna empresa editorial para su publicación u otros fines, sin contar previamente con la autorización escrita de la Universidad.

Asimismo, autorizo a la Universidad que realice la digitalización y publicación de este trabajo de integración curricular en el repositorio virtual, de conformidad a lo dispuesto en el Art. 144 de la Ley Orgánica de Educación Superior

Urcuquí, Julio 2020.

Joselyn Synei Benalcázar Jaramillo
CI: 100341831-4

Dedication

I want to dedicate this hard work to my family, who with their patience and love have accompanied me during this project. To my parents for motivating me to study what I am passionate about, for teaching me to be persevering, for supporting me in my studies, and for being so generous with their advice and experiences. To my dear brothers for teaching me to share happy moments, and to tolerate bad moments. Finally, I dedicate this work to my grandmother who has been very attentive and generous to me, always supporting me in my studies and in life.

Acknowledgements

First, I would like to thank my Ph.D. tutor Sarah Briceño who guided me in the best way in carrying out this work, and financed part of the project. I also want to thank my co-tutor Ph.D. Julio C. Chacón Torres who generously gave me the opportunity to do a research stay at the Free University of Berlin-Germany. Thanks to this, a complete characterization of the project could be made. He also support this project with the graphene oxide powder. I would also like to thank Ph.D. Nelson Vispo for directing the antibacterial part of this work, for supplying the E. coli bacteria needed for the antibacterial tests, and for allowing me to use the biology laboratory when necessary. In addition, I would like to thank Eng. Karla Miño for instructing me about anti-bacterial testing.

I would like to thank the Free University of Berlin (FU), for the characterization performed, under the supervision of Prof. Stephanie Reich. I want to extend my most sincere thanks to Prof. Stephanie Reich for receiving me at the FU and allowing the characterization. To Ph.D Katty Hubman for the attention received and for teaching me how to use UV-Vis spectrometer. To Ph.D Antonio Setaro for instructing me in the handling of the photoluminescene characterization technique. To Ph.D Svitlana Trotsenko for leading the TEM characterization, Ph.D student Sabrina Juergensen for instruction in the photoluminescence technique, and Ph.D student Georgi Gordeev for the instruction in the Raman Spectroscopy.

I thank the School of Physical Sciences and Nanotechnology for funding the airplane ticket for the research stay. Also, I want to thank Ph.D. Gema Gonzalez who contributed to the development of this work with her expertise in antibacterial properties. Finally, a deep gratitude to my research partners José Arcos and Esteban Lasso, with whom I worked experimentally and theoretically during the development of this project, and the development of my career. Thanks to their companionship and generosity, this research was possible.

Abstract

In this work, we report the antibacterial properties of a nanocomposite formed by silver triangular nanoplates deposited on graphene oxide (AgTNPs/GO). This study proposes an innovative and sustainable method to growth silver triangular nanoplates onto graphene oxide using a light-induced process. The nanocomposite was synthesized by an *in-situ* photoreduction method at different irradiation wavelengths (440, 540, 650 and 200-700 nm) at room temperature. AgTNPs/GO was characterized using: Scanning Electron Microscopy (SEM), Transmission Electron Microscopy (TEM), Raman Spectroscopy, UV-Vis Spectroscopy and Photoluminescence (PL). The antibacterial properties were observed against Gram-negative Escherichia coli by antimicrobial disk diffusion test and optical density. The results show that the AgTNPs/GO nanocomposite has enhanced the antibacterial properties compared with silver nanoparticles. This is due to the synergistic effect resulting of AgTNPs and GO; AgTNPs by the high reactivity of the constituent facets (111), and GO for its strong adsorption property originating from the oxygen functionalities. These results demonstrated that AgTNPs/GO nanocomposite are promising for a wide range of biomedical applications.

Keywords: Silver nanoparticles, silver triangular nanoplates, graphene oxide, and antibacterial properties.

Resumen

En este trabajo, reportamos las propiedades antibacterianas de un nanocomposito formado por nanoplatos triangulares de plata depositados en óxido de grafeno (AgTNPs/GO). Este estudio propone un método innovador y sostenible para el crecimiento de nanoplatos triangulares de plata en óxido de grafeno usando un proceso inducido por luz. El nanocomposito fue sintetizado por un método de foto-reducción *in-situ* utilizando diferentes longitudes de onda de irradiación (440, 540, 650 y 200-700 nm) a temperatura ambiente. Se caracterizó los AgTNPs/GO usando: Microscopía Electrónica de Barrido (SEM), Microscopía Electrónica de Transmisión (TEM), Espectroscopía Raman, Espectroscopía UV-Vis y fotoluminiscencia (PL). Las propiedades antibacterianas contra la Escherichia coli Gram-negativa se observaron por medio de la prueba de difusión de discos antimicrobianos y la prueba de densidad óptica. Los resultados muestran que el nanocomposito AgTNPs/GO mejora las propiedades antibacterianas en comparación con nanopartículas de plata. Esto se debe al efecto sinérgico resultante de los AgTNPs y GO; los AgTNPs por la alta reactividad de las facetas constituyentes (111), y GO por su fuerte propiedad de adsorción originada por los grupos funcionales. Estos resultados demostraron que los nanocompositos AgTNPs/GO son prometedores para una amplia gama de aplicaciones biomédicas.

Palabras Clave:

Nanopartículas de plata, nanoplatos triangulares de plata, óxido de grafeno y propiedades antibacterianas.

Contents

List of Figures

List of Tables

Chapter 1

Introduction

1.1 Nanotechnology

The miniaturization of electronic devices is one of the scientists aims since 1965[1]. Scientists proved that by arraying large numbers of microscopic transistors on a single chip, microelectronic circuits could be built with improved performance, functionality, and reliability without neglecting costs. G. Moore informed that the number of transistors on integrated circuits has been doubling approximately every 2 years since 1965[2]. On the other hand, Richard Feynman presents the first concept of nanoscience as a talk to the American Physical Society in 1959 under the title ″ There's plenty of room at the bottom ″. In this talk, Richard Feynman described the exciting possibilities that would open up if scientists could learn how to control single atoms and molecules, and improve the performance of instruments, such as electron microscopes[1].

The invention of a scanning tunneling microscope (STM) in 1981 was a breakthrough in the investigation of material with atomic resolution and the atom–by–atom manipulation[2]. These events allowed nanotechnology to emerge as the science that handling the matter at the atomic scale. Besides, the nanotechnology is defined as the understanding, control, and restructuring of matter at the nanoscale (1-100 nanometers), remembering that one nanometer equals a billionth part of a meter ($10^{-9}m$), to create materials with fundamentally improved properties and functions[3].

1.2 Nanomaterials

With the improvement of electron microscopes, scientists were able to study the materials at nanoscale called nanomaterial field. A nanomaterial is characterized by having at least one dimension in the nanometer range, and thus it can be classified as (i) 0D when the three dimensions are less than 100nm (nanoparticle, nanoclusters, quantum dot), (ii) 1D when two dimensions are in the nanoscale range (nanowire, nanotube), (iii) 2D when just one dimension is less than 100nm (monolayer) and (iv) 3D when any dimension is at nanoscale (nanostructured materials)[4].

Besides, nanomaterials can be classified by the kind of constituent materials as organic, inorganic, and carbon-based. These nanomaterials have great importance due to the small size of the building blocks and the high surface–to–volume ratio[5]. These characteristics allow having unique structural, optical, thermodynamic, electronic, spectroscopic, electromagnetic, and chemical properties[4]. The control method of the properties is subjected to the preparation of nanomaterials. There are two types: the first is top-down in which larger structures are reduced in size to the nanoscale while maintaining their original properties without atomic–level control. The second is the bottom-up method or molecular manufacturing, in which materials are designed from atoms or molecular components through a process of assembly or self-assembly[3].

Several methods are used to fabricate nanomaterials to have a controlled synthesis, top-down: Lithography, grinding, bottom-up: Chemical Vapor Deposition (CVD), laser ablation, thermal decomposition, hydrothermal synthesis, photochemical synthesis, and others. Controlled synthesis benefited to the industry allowing some critical nanomaterials applications which are the following: (i) nanopowders of ceramics, (ii) nanocomposite, (iii) nano electrochemical systems, (iv) applications of nanotubes for hydrogen storage, (v) DNA chips, (vi) gene targeting/drug, and (vii) nanoelectronics and nanodevices[4].

1.2.1   Silver Nanoparticles

Nanoparticles have advantageous properties such as high surface area to volume ratio, which is inversely proportional to the radius of the nanoparticle, and it is related to the reactivity[6]. Noble metal nanoparticles (Ag, Au, Pt) are of great interest due to their are resistant to corrosion and oxidation[7]. In addition, they have useful and advantageous electronic and optical properties for a wide range of applications[8]. Their properties were used since ancient times for example in stained glasses[9]. Medieval artists dabbled in alchemist, they mixed gold and silver metal chloride with the molten glass to give dyes as yellow and red, which shines with the sun light[9]. One example of its optical properties is the Notre Dame Catedral of Paris stained glass[10]. When the sunlight touched the stained glass, the silver and gold nanoparticles present act as reflectors; they catch all the wavelengths that come from the sunlight and, then they reflects one[10]. The wavelength reflected is in the visible range of the spectra, and it depends on the particle size and shape[10]. Thus, the optical properties of metal nanoparticles are strongly dependent on their size and shape[11]. Optical properties are unique of noble metal nanoparticles and have potential applications such as chemical sensors, catalysis, antibacterial agent, optoelectronic devices, surface enhanced Raman spectroscopy, molecular diagnostics, among others[8]. Among the noble metals, silver is of great importance owing to it is photo-sensitive to light; it has the most effective light trapping potential[11], and it has been recognized as an effective antibacterial agent[12].

Silver Triangular Nanoplates

Depending on the method used to produce nanoparticles, either top-down or bottom-up, different shapes as nanoprisms can be obtained[11]. Nanoprisms term involves anisotropic structures such as hexagonal, pentagonal, polyhedron, tetrahedron, octahedron, planar twinned, right bipyramid, and triangular nanoplates shapes[13]. When the lateral dimension of silver triangular nanoplates is much larger than the thickness, they possess an extreme degree of anisotropy[14]. Figure 1.1 shows a scheme of different anisotropic structures with the facets that constitute them as

(100) and (111)[13].
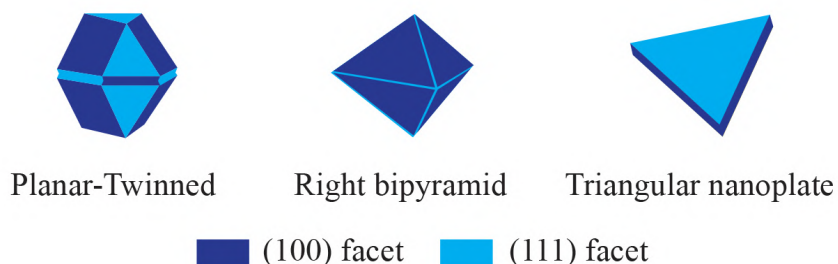
Figure 1.1: Scheme of different anisotropic structures. Adapted from Zhang J. *et al..*[13]

The facets (111) are high-atom-density coming from the face centered cubic (fcc) configuration that silver nanoparticles have. Figure 1.2 shows the fcc structure and (111) facets.
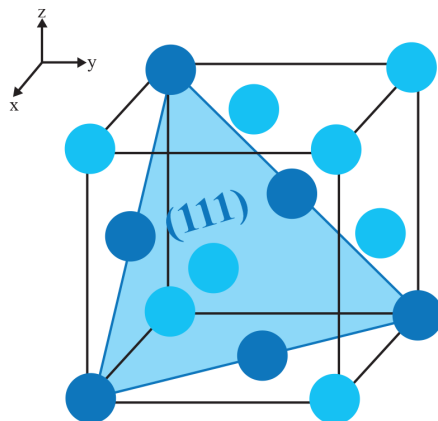
Figure 1.2: Scheme of face centered cubic configuration and (111) facet. Adapted from Escudero Maria[15]

The optical behavior of metal nanoparticles results from the interaction of their free conduction electrons with the incident light[16]. Then, when the oscillating electric field given by the incident light resonantly couple with the conduction electrons, it results in a surface plasmon resonance (SPR)[10]. SPR appears as an intense band in the absorbance spectra and depends on the structural characteristics of the nanoparticles, such as their size and shape[17]. It has been reported that anisotropic shaped nanoparticles can have more than one band in their spectra due to the different resonance modes that their structural configurations can generate[16]. Figure 1.3 shows the characteristic resonance modes for silver triangular nanoplates.
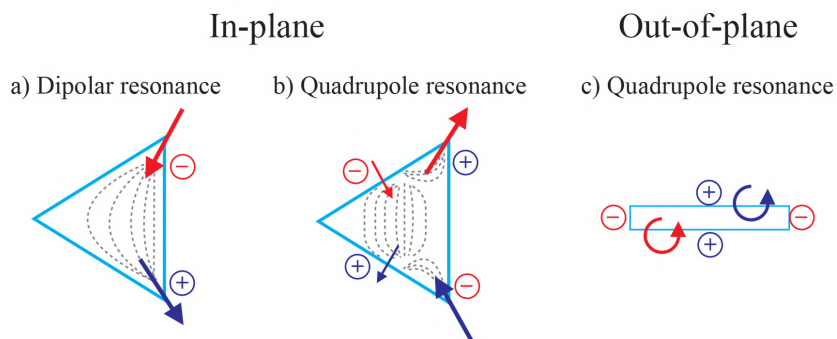
Figure 1.3: Illustration of different resonance modes for silver triangular nanoplates (a) in-plane dipolar resonance, (b) in-plane quadrupolar resonance and (c) out-of-plane quadrupole resosnance. Adapted from Yao H. and Shiratsu T.[18]

Figure 1.3 shows three main resonance modes corresponding to the triangular nanoplates anisotropic structure. 1.3(a) present the in-plane dipolar resonance, here can be seen two polarities (due to the electric field applied) represented with the symbols + and -, also, the dashed lines indicate the geometrical orientation of collective electrons oscillations[18]. When these resonance modes oscillates at the same frequency of the light induced, results in a surface plasmon resonance (SPR) which appears as a strong band absorption in the UV-Vis spectra[16]. It is assumed that the magnetic field applied is perpendicular to the page[18]. Fig. 1.3(b) shows the in-plane quadrupole resonances in which four polarities causing four different orientations for the electron oscillation are observed[16]. Finally, Fig. 1.3(c) exhibits out-of-plane quadrupole resonance that generates weak SPR in the UV-Vis spectra[18].

Synthesis of Silver triangular Nanoplates

The synthesis method used to obtain silver triangular nanoplates have allow to control of nanoparticles size and shape[11]. The best candidates are the chemical reduction method[19] and the photochemical reduction method[11]. Figure 1.4 presents an scheme of the two methods used to control the size and shape of silver nanoparticles.
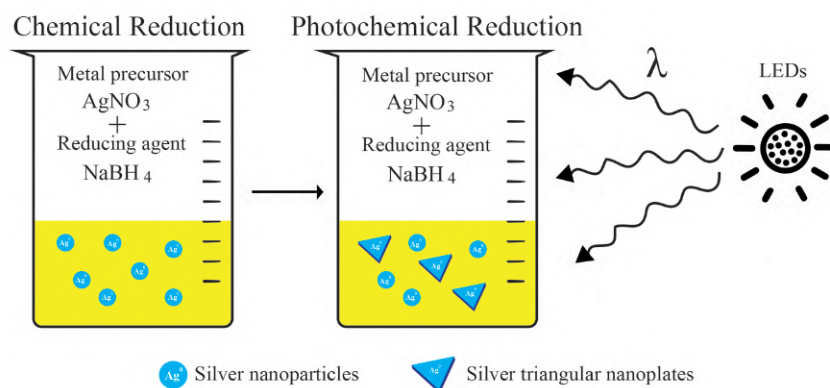
Figure 1.4: Chemical reduction and photochemical reduction methods to synthesize silver triangular nanoplates.

Fig. 1.4 shows the two methods to control the size and shape of nanoparticles. The chemical reduction method needs two main components: a metal precursor that usually is silver nitrate ($AgNO_3$), and a reducing agent that commonly is the sodium borohydride ($NaBH_4$)[11]. While the photochemical reduction method uses the chemical reduction to produce silver nanoparticles seeds, as a colloidal suspension, and then they are irradiated with light, generally by lamps, or high power light emission diodes (LEDs) to promote an oriented growth of nanoparticles[19]. Saade and Araújo[11] used LEDs to irradiate the sample with a selected wavelength λ from the visible spectra[11].

The oriented light-induced (photochemical) growth depends of the silver nanoparticles seeds shapes[13]. Generally, seeds nanoparticles have a very small size, around from 5-8 nm[20]. Pal S. *et al.* reported that small silver nanoparticles around 5-8 nm has quasi-spherical and planar twinned anisotropic shapes, which are results of defects present such as stacking faults and planar twin[19]. Therefore, the pathway of growth depends on the initial shape of AgNPs[13]. Figure 1.5 shows the growth pathways from quasi-spherical and planar twinned, to triangular nanoplates.
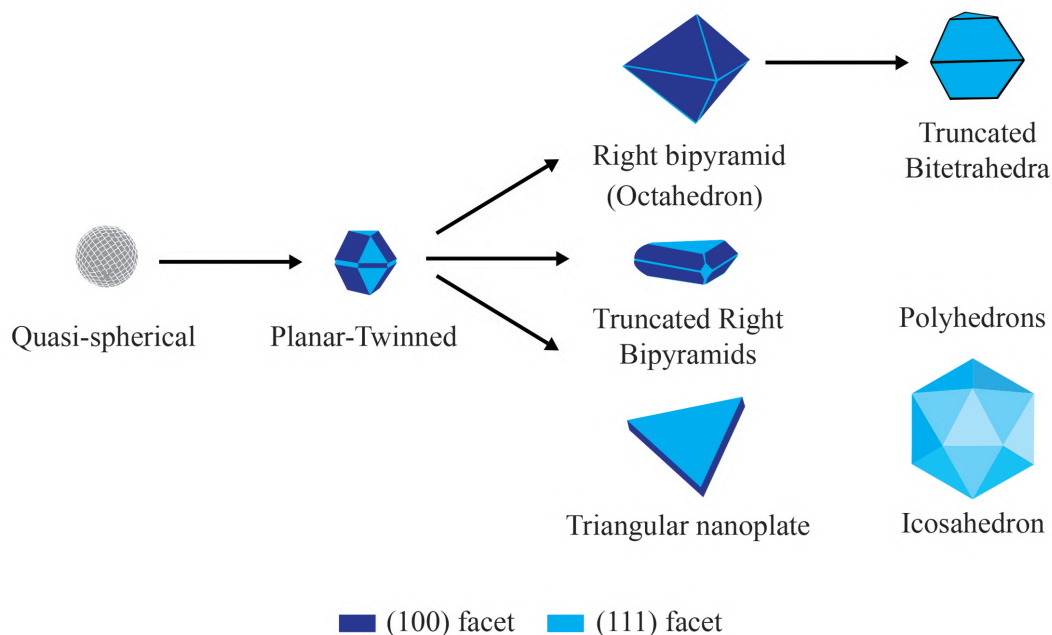
Figure 1.5: Growth pathways from quasi-spherical and planar twinned, to triangular nanoplates. Adapted from Zhang J. *et al.* [13].

Fig. 1.5 exhibits the growth pathways of quasi-spherical and planar twinned seeds. From the quasi-spherical form, through the photo-induced process a planar twinned shape is obtained [13]. Then, over time progresses, several shapes can result such: right bipyramid, truncated bitetrahedra, truncated right bipyramids, and triangular nanoplates [13]. The anisotropic shapes contain different facets represented as: light blue the (111), and the dark blue (100). Therefore, the oriented growth by photochemical reduction method is applied to produce specific structures containing preferential facets as desired [11]. Others polyhedrons shapes such as tetrahedron, icosahedron, decahedron and octahedron can results, due to the final nanoparticle shape is mainly dependent of the initial structure [19].

Size and shape of nanoparticles depend on the variation of the metal precursor and the reducing agent amounts, as well as the time, light intensity and irradiation wavelength [19]. Other components are used in the chemical synthesis to promote anisotropic structures such as hydrogen peroxide reported by Zhang Q. *et al.* [19], and capping agents-stabilizers such as trisodium citrate (TSC) reported by Saade & Araujo [11]. TSC additional component create a capping agent which charges negatively the nanoparticle, creating repulsive electrostatic forces between them [11]. Several combination of components are reported [11,13,19], the variation of all of them influence in the final size and shape of nanoparticle.

1.2.2 Graphene Oxide

Carbon-based nanomaterials are those made up of carbon atoms with different structural configurations such as fullerenes, carbon nanotubes, graphite, graphene and diamonds[21]. Different hybridization states such as sp, sp2, or sp3 are also responsible for several types of structures.[22]. Especially, graphene carbon-based nanomaterial present extraordinary advantageous physical, chemical, mechanical, and electronic properties for applications such as sensors, antimicrobial agents, surface enhanced Raman spectroscopy, etc[21].

Graphene oxide (GO) is a 2D carbon-based nanomaterial that has a monolayer of carbon atoms packed into a honeycomb crystal structure. Because of its unique nanostructure and fascinating properties, GO sheets are attractive as potential nanoscale building blocks of new nanocomposites. One of the most common methods to prepare GO is the chemical exfoliation of graphite in an aqueous medium, which produces oxygen functional groups in graphene sheets. Figure 1.6 shows the graphene oxide structure, in which the functional groups resulted from the chemical exfoliation of graphite are indicated.
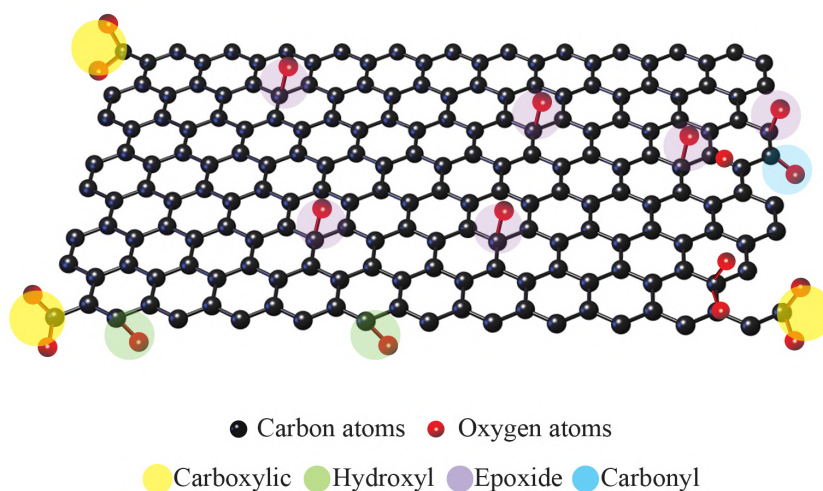
Figure 1.6: Illustration of graphene oxide (GO) with oxygen funtionalities at the surface and edges such as carboxylic, hydroxyl, epoxide and carbonyl. Adapted from Nanografi[23].

The presence of the oxygen functionalities at the graphene surface provides reactive sites for the nucleation and growth of metal nanoparticles (Au, Ag, Cu)[24]. Thus, graphene oxide is an ideal support material for the dispersion of metal nanoparticles[25]. Besides, the polar oxygen functional groups on the surface make it hydrophilic and dispersible in water[26]. The significant effects produced in the association of graphene oxide with metallic nanoparticles promise potential applications such as chemical sensors, energy storage devices, antibacterial agents, among others, that have attracted the attention of researchers[12,24,27–29].

1.3   Nanocomposite

Nanocomposite is constituted by the combination of two materials, where at least one of them is in the nanoscale[30]. One of these materials acts as a base, matrix, template, or support material, and the other is the reinforcement nanomaterial added to improve physical or chemical properties either optical, magnetic, electrical, chemical, mechanical, catalytic, among others[31]. Therefore, the nanocomposites are multifunctional materials promising many applications in chemical sensing, hydrogen storage, biomedicine, drug delivery, tissue engineering, energy storage, antibacterial activity, coatings, etc.[32].

Depending of the base material used, the nanocomposites can be classified as: polymer-based, metal-based, ceramic-based, metal-based, and graphene-based[31]. Polymer-based nanocomposites consist of a polymer o copolymer having a nanomaterial dispersed in the polymer matrix[31]. One example of a polymer-based nanocomposite is the dispersion of carbon nanotubes in the polymer matrix, in order to reinforce thermosetting (epoxy) and thermoplastic polymers (polyethylene)[32]. Carbon nanotubes reinforced nancomposites improve mechanical properties of polymer materials[30]. Another example of polymer-based nanocomposites is the addition of copper at the surface of cotton fiber, to enhace antimicrobial, antiviral, and antifungal properties[20]. Besides, polymer-based composites are significant for biomedicine applications, due to its capability of interact with biomolecules[33]. One of the most important advances in medicine is the use of biocompatible polymers (PHAs, PLGA)[34] as coatings to carry the drug for specific sites of the human body, as an alternative for cancer treatment[33].

Another type of nanocomposites is ceramic-based, which has significant commercial applications in highly efficient gas turbines, aerospace materials, automobiles, etc[30]. The nanocomposite matrix is constituted of ceramic, and it occupies most of the volume[32]. Examples of ceramics are often from the group of oxides such as nitrides, borides, silicides, whereas the second material is usually a metal[31]. Ideally, both components are finely dispersed in each other, in order to obtain specific optical, electrical, magnetic, and protective properties[31]. Ceramic combined with metal offers a solution for ceramic materials problems, such as fracture toughness and strength, degradation of mechanical properties at high temperatures, and poor resistance to creep[30]. For example, the incorporation of metal nanoparticles into ceramics such $BaTiO_3$, ZnO, or cubic ZrO_2, can significantly improve mechanical strength for electric devices operating in several environmental conditions[30].

Metal-based nanocomposites consist in a metal matrix with the integration of semiconductor or metal oxide components[35]. These nanocomposites exhibit enhanced optical properties, photocatalytic activities, and ultrafast carrier dynamics[28]. Among the base metals, platinum Pt is the most effective electrocatalyst for methanol oxidation reaction, formic acid oxidation reaction, and oxygen reduction reaction[35]. Metal-based nanocomposites composed by iron and chromium with aluminum oxide are used to enhace the strength of materials, it has applications in automobile, and aerospace industries[36]. In this type of nanocomposite, metal nanoparticles can be included. For example, metal nanoparticles are coated with polymers[33]. Gold nanoparticles covered with polymer (chitosan, PVP) are used for cancer treatments[37]. The functionalization of gold nanoparticles with polymers has the aim of performing

localized targeted treatment, and represents an alternative for non-invasive treatments avoiding secondary damages[37].

Finally, graphene-based nanocomposites are generally made of metal nanoparticles dispersed on graphene layers[38]. Graphene oxide (GO) is preferred to make these nanocomposites, due to the oxygen functionalities present at the surface and edges, which are reactive sites for the dispersion of metal nanoparticles[28]. Graphene oxide with metal nanoparticles system has applications in energy storage, chemical sensing, catalysis, and antibacterial activity[39]. One example of these nanocomposites involve the presence of silver nanoparticles (AgNPs), which are recognized by their antibacterial properties and applications in biomedicine[26]. Figure 1.7 shows a nanocomposite graphene oxide with silver nanoparticles (AgNPs/GO).
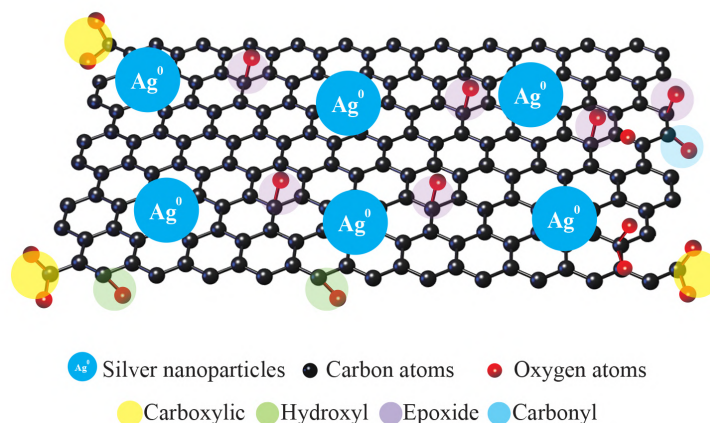
Figure 1.7: Example of graphene-based nanocomposite, silver nanoparticles dispersed on graphene oxide nanocomposite(AgNPs/GO). Adapted from Huang L. *et al.*[39].

Fig.1.7 shows silver nanoparticles dispersed on graphene oxide flake, which acts as a support material[40]. The dispersion is made by electrostatic attractions due to different charged of nanomaterials[28]. These kind of nanocomposites have three advantages:; first the graphene oxide prevents the oxidation of silver nanoparticles, and thus enhance the chemical stability, second the graphene oxide provides reactive sites for nanoparticles dispersion, and third this hybrid material is suitable for further functionalizations[41]. Within the wet-chemistry methods the last decade, have become a powerful tool to direct the synthesis of these (AgNPs/GO) nanocomposites[30].

1.4 Synthesis of AgNPs/GO Nanocomposite

Several methodologies have been used to synthesized AgNPs/GO. One of the most used is the chemical reduction method; it consists of two steps: the first one is the dispersion of graphene oxide in a solvent (water, ethylene glycol)[42], and the second one is the addition of silver precursor and a reducing agent to form nanoparticles on the

graphene oxide[43]. Another way to use this chemical reduction method is by a separated procedure, in which first the graphene oxide (GO) is dispersed, while silver nanoparticles are sepparatelt formed. Finally the GO solution and silver nanoparticles colloids are pocked in the same container and mixed by stirring[44]. Figure 1.8 shows an scheme of the chemical reduction method for synthesize silver nanoparticles in the presence of GO.
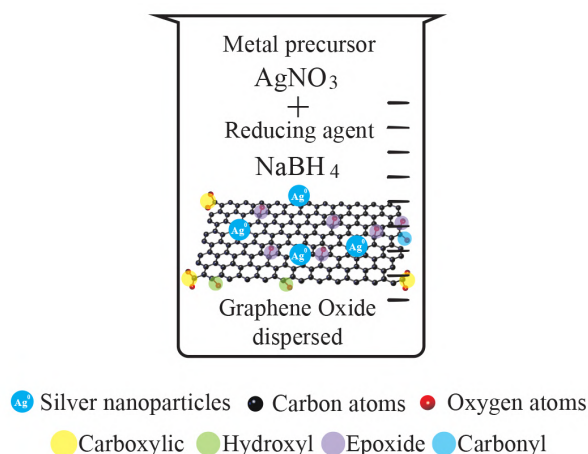
Figure 1.8: Scheme of the chemical reduction method, silver nanoparticles formed in the presence of graphene oxide.

Fig.1.8 shows a representation of silver nanoparticles as blue light spheres, graphene oxide with their oxygen functionalities as carboxylic, hydroxyl, epoxide, and carbonyl which are reactive sites for the dispersion and growth of metal nanoparticles[24]. Beside, the scheme exhibits a common beaker with three main components to synthesize AgNPs/GO nanocomposite. The first component is a dispersed GO. Graphene oxide can be dispersed in water, with stabilizer agents as polyvinyl alcohol[26]. Then, a metal precursor silver nitrate $AgNO_3$ is added as to be reduced by sodium borohydride $NaBH_4$ in the presence of GO. However, due to the use of a reducing agent in the presence of the GO, different results can be obtained as the reduction of functional groups[44]. Silver nanoparticles are deposited on graphene oxide through physical adsorption, in which electrostatic attractions play an important role[41]. Graphene oxide is negatively charged and nanoparticles ends with a neutral charge, due to the reduction of silver ions Ag^+ to Ag^0[45]. Some researchers have been reported this method: Huang L. *et al.*[39] reported the synthesis of AgNPs/GO nanocomposite through chemical reduction, they used $AgNO_3$ on the GO matrix, and NaBH4 directly reduced them. Moraes A. *et al.*[46] reported a chemical reduction process, they first dissolved GO flakes and then, they added silver precursor and reducing agent to produce silver nanoparticles. Tang J. *et al.*[27] used the chemical reduction method, as well as mentioned above, silver precursor $AgNO_3$ powder was added to the GO solution and reduced.

Unlike the reduction of silver precursor in the presence of GO method, the method in which the silver nanoparticles synthesized are mixed with GO, ensures that the properties of GO are more likely to be maintained[47]. Figure 1.9 exhibits an scheme of the chemical reduction method for synthesize silver nanoparticles apart from graphene oxide.
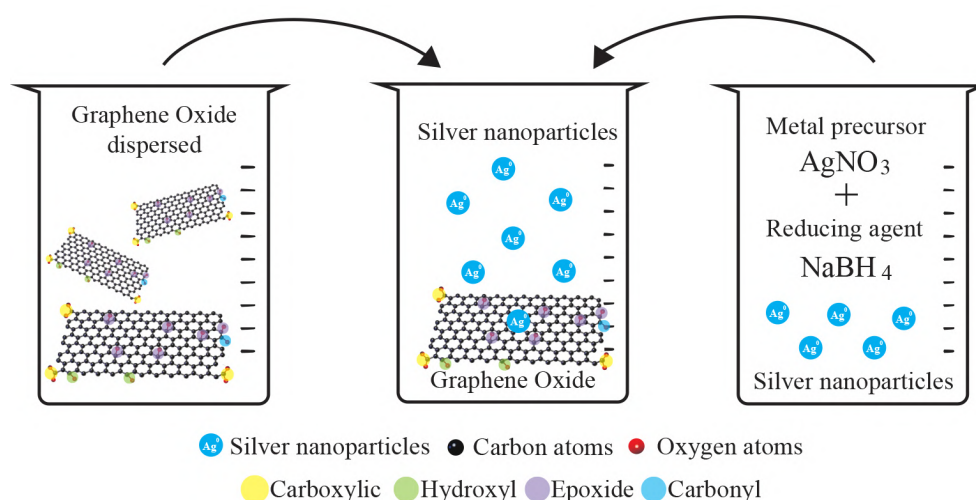
Figure 1.9: Scheme of the chemical reduction separated method, silver nanoparticles formed apart from graphene oxide.

In the Fig.1.9 it is exhibited three beakers (from the left to the right): the first beaker represents graphene oxide dispersed in water, the third beaker contains the colloidal solutions of silver nanoparticles, generally formed by the reduction of a metal precursor AgNO$_3$ by sodium borohydride NaBH$_4$. Reports that use this kind of chemical reduction method are: Zhang D. *et al.*[44] reported a separated chemical reduction method, silver nanoprisms colloid was formed first, then graphene oxide is dispersed, and finally they were mixed together. Ma J. *et al.*[47] prepared silver-modified graphene oxide by the modification of GO with Ag nanoparticles previously prepared using a glucose reduction method.[47]

1.5 Antibacterial properties and synergistic effect of AgNPs/GO Nanocomposite

It is known that silver nanoparticles (AgNPs) show strong inhibitory and antibacterial effects[48] due to their posses higher surface-to-volume ratio as compared to bilk materials, which directly influence in the antibacterial activity[49]. However, when the nanoparticles come into contact with the bacteria cell membrane, they tend to agglomerate and lose this important property[47]. In order to protect the high surface reactivity of nanoparticles, graphene oxide (GO)[50] is an ideal support material. In addition, due to GO has strong adsorption properties for its oxygen functionalities, bacterial cells could be attracted, increasing the contact between them and improving the antibacterial activity of AgNPs and GO[51]. It should be considered that E. coli bacteria membrane and GO sheets are negatively charged, so they would repel each other[39]. Nevertheless, the lipopolysaccharide subunits in the outer membrane of E. coli contain sugars, phosphates, and lipids[47], while GO have oxygen functionalities and therefore hydrogen bonding

could be formed[52]. Hydrogen bonding contributes with the adhesion of E. coli cells onto GO and so, as a first cell damage, it blocks the cells from intaking nutrient[47].

The antibacterial contribution of graphene oxide is given by adhesion properties, which depend on sheet size, layer number, and hydrophilic surface[53]. Bacteria can be isolated from the nutrient media when it is wrapped (small sheet) or entrapped (large sheet >20 μm) by GO sheets, leading to cell death[53]. The layer number determines the bending stiffness, as the layer number decreases the absorptive capacity increases[54]. Bacteria prefer hydrophobic surfaces which creates strong binding forces, in contrast hydrophilic interactions are a reversible/irreversible process, which is a vulnerable adhesion[54]. Additionally, since GO has thin sharp edges they can pierce the bacteria membrane, resulting in a disruption of membrane permeability which alters the passage control of extracellular things, beneficial for the nanoparticles antibacterial activity[54].

Graphene oxide antibacterial activity is also altered when they act alone, they tend to aggregate due to strong inter-plane interactions, decreasing their surface area property[53]. The deposition of AgNPs on GO produces a decrease in the negative charge and hydrophilicity facilitating the contact between the E. coli cells and AgNPs/GO nanocomposite[47], and enhancing the antibacterial activity of AgNPs. The first damage is to the bacterial cell membrane due to silver nanoparticles interact with the sulfur containing proteins of cell walls[50]. Intracellular antibacterial effects are given by the addition of silver ions coming from the oxidation reaction of silver nanoparticles[45]. Positively charged silver ions interrelate with negatively charged lipids and proteins on cell membranes, due to electrostatic attraction[51], resulting in the increase of membrane permeability[55,56]. Selective permeability of membrane controls the substances passing in and out, therefore an alteration can change the cells morphology and their function[7].

Besides, silver ions are more likely to interact with transport or respiratory chain enzymes that are vital to the cell function and they are localized in the inner mitochondrial membrane[57]. E. coli possesses two different NADH dehydrogenases enzymes[58], which produce possible sites for Ag^+ binding[57]. This binding in the respiratory chain causes an inefficient passage of electrons to oxygen at the terminal oxidase, which produces reactive oxygen species (ROS), such as superoxide anion radical, hydrogen peroxide and hydroxyl radical[51], as a disturbance of bacterial antioxidant defense[54]. At high concentrations they interact with biomolecules causing oxidative damage, such as denaturation, fracture and cross linking[51]. Other intracellular affections are related to DNA damage and protein deactivation[51]. When the silver ions interact with the DNA, they turned into a condensed form affecting the ability to replicate[59]. While for proteins thiol group is responsible for enzymatic activity and when they react with Ag^+ ions result in the inactivation of proteins[60].

Figure 1.10 shows a scheme of Ag^+ ions antibacterial activity in the bacteria cell that it can be membrane disruption, DNA condensation, protein damage, and ROS species[51].
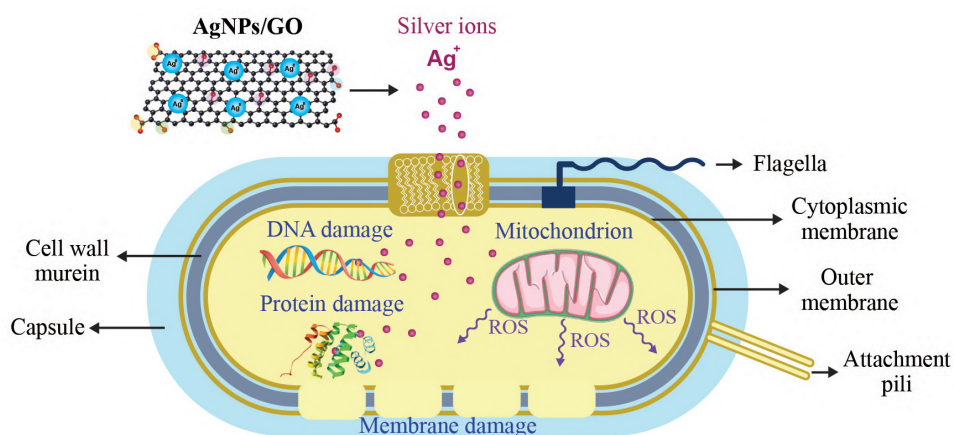
Figure 1.10: Scheme of bacteria cell structure and antibacterial activity of AgTNPs/GO nanocomposite. Silver ions coming from the nanocomposite have a disruptive interaction with the cell membrane of bacteria, resulting intracellular antibacterial effects. Adapted from Song B. *et al.*[51]

Described in four phases: i) the first stage consists in the oxidation of AgNPs deposited on GO, by dissolved oxygen[61], ii) the second phase requires the contact between Ag^+ ions and bacterial cells[55,62], iii) the third phase involves a disruptive interaction of silver ions with bacteria, through binding membrane proteins or phospholipid bilayer, then more silver ions or even the nanocomposite are allowed to pass[59], finally iv) the fourth phase consists in the direct binding of Ag^+ ions with proteins, lipids, enzymes, DNA, and the oxidation of them by generating ROS[63].

Antibacterial properties of silver nanoparticles deposited on graphene oxide are strongly dependent on the synergistic effect of these nanomaterials[50]. synergistic effect is a simultaneously antibacterial contribution from AgNPs and GO. This effect is also called the capturing-killing process, and it depends on the strong adsorption properties of graphene oxide[51]. The capturing-killing process is due to the functional groups present at the surface and edges of the graphene sheets[28]. On the other hand, silver nanoparticles antibacterial activity depends of their shape[49]. It has been reported that anisotropic nanoparticles have better antibacterial efficiency than spherical, due to the presence of (111) high-atom-density facets on its structural configuration[49], as Fig. 1.2 shown.

1.6 Antibacterial Applications

Metal nanoparticles have great importance in the biological field, specifically in antibacterial studies[26]. Silver is most attractive due to its low cost and small negative environmental impact[64]. It has been known as an antibacterial agent for centuries. Silver nanoparticles (AgNPs) themself can directly cause bacterial cell membrane damage, leading to increased permeability, and eventually result in cell death[47]. An excellent example of the antibacterial properties use is the wound dressing for skin repair and regeneration; it acts against infections caused by E. Coli or

Staphylococcus aureus bacterias[65]. The AgNPs are incorporated with other polymers as PVA to enhance stability, this final composite was found biocompatible and significantly inhibited the growth of bacterias[65]. Further, these are used as nanoporous silver powders with particle size between 50-100 nm encapsulated for gradual release[66]. Graphene is also an attractive material for these dressings, due that it affects the proliferation of prokaryotic cells and promotes healing by lowering infection and enhance proliferation of fibroblasts[65].

Medical devices have also taken advantage of the silver nanoparticles. The catheter is the best example since it must have to avoid infections, due it is placed in the human body for a prolonged time[66]. This device is described as any small tube that is inserted into the body for medical purposes either for providing a route for drainage, to provide medicine, diagnostic treatment, among others[67]. Silver nanoparticles coatings have been developed to prevent infections in catheters[66]. The advantage is that silver nanoparticles are produced by a proprietary process and do not require a binder since the nanoparticles adhere to the material by surface forces. Silver coatings are also used for imaging enhancement, drugs, or electrical stimulation[66].

Ag/Graphene nanocomposites have been used as membrane antibacterial agents[68]. This combination can improve the hydrophilicity, mechanical property, and permeability which exhibited significant antibacterial adhesion property[41]. The modified membrane can be used in the separation-desalination membrane process for water purification. Another application of this nanocomposite is in plant protection and nutrition. The DNA-directed AgNPs grow on GO composite and acts as an antibacterial agent against Xanthomonas performans, which is useful in tomatoes cultures[41]. In another way, the nanocomposite could increase surface enhanced Raman spectroscoyp (SERS) activity, electro catalytically active surface area, and stability for sensors[41]. Ag/Graphene can improve the signal in EM sensors based on the enhancement of localized electromagnetic field that comes from the localized surface plasmon resonances (LSPRs) of noble metal nanoparticles[41].

1.7   Reported Studies of AgNPs/GO antibacterial properties

Ag/GO nanocomposites research field promises the improvement of optical, electronical, mechanical, and antibacterial properties. Different methodologies are used to produce these nanocomposites which generate applications in wound dressing, medical devices, coatings, catalysis, SERS, and antibacterial agents[28,62,65]. The study of antibacterial properties is very useful and important for the field of biomedicine. Currently, bacteria are showing resistance to traditional antibiotics such as ampicillin[50]. Its instability limits its application, and Ag/GO nanocomposites, which are inorganic materials with stable properties[50], becomes an alternative antibacterial agent. Therefore, the synthesis, characterization, and antibacterial properties study of Ag/GO nanocomposites are critical issues these days.

Graphene-based nanocomposites have been widely studied to improve their properties and applications. The deposition of silver nanoparticles on graphene (acting as a supporting material) results in enhanced antibacterial properties[26]. Few studies of this nanocomposite have been published[12,12,27,28,40] taking focusing on different synthesized methods, nanostructural studies, and antibacterial applications. He *et al.*[41] reported the advancement of Ag graphene-based nanocomposites in which an overview of the synthesis and its applications are detailed. The methods used to synthesize Ag/GO and Ag/rGO are; the reduction method of silver nanoparticles in the presence of GO (detailed in Fig. 1.8), and the reduction method separated (detailed in Fig. 1.9), respectively[69,70]. In the

deposit method, AgNPs are prepared firstly and then deposited on GO sheets and, in the chemical reduction method, various reductants such as borohydride, sodium citrate, ascorbic acid, and dopamine are used. They conclude that nanocomposites improve antibacterial activity than the individual nanomaterials.

Jaworski *et al.* [28] present a nanocomposite with silver nanoparticles (Ag NPs) on the surface of graphene oxide (GO) as an antifungal material. The nanocomposite was synthesized by an ultrasonic coating of polyurethane foils with suspensions of Ag NPs and GO. The antibacterial results showed that the decoration of GO with Ag NPs promotes a synergistic effect that reaches an inhibition growth of 88.6% of E. coli [28]. Shao *et al.* [12] reported a green synthesis to prepare GO decorated with Ag NPs based on chemical reduction, which involves reduction and stabilization by glucose and starch. The nanocomposite showed an antibacterial ratio of 98.36% E.coli. (based on the numbers of bacteria colonies incubated). Huang *et al.* [39] reported an *in-situ* chemical reduction method to prepare Ag NPs/GO that consists mainly of reducing different volume $AgNO_3$ solution on the surfaces of GO with $NaBH_4$ as reductant. The results of the nanocomposite showed that the loading of AgNPs in the nanocomposites is a crucial parameter for antibacterial activity. The antibacterial activity against E.coli is tested by measuring in the diameter of inhibition zone (DIZ) in a disk diffusion test, resulting in that clear and significantly larger DIZs surrounded the disks supporting AgNPs/GO nanocomposites.

Chapter 2

Motivation

The motivation for this project is focused on two points: the study of the antibacterial properties of silver triangular nanoplates deposited on graphene oxide nanocomposite comparing with silver nanoparticles, and the synthesis of the nanocomposite by photoreduction method.

As was discussed above, several reports have have been published about the synthesis, characterization and antibacterial properties of Ag/GO nanocomposites. All of these reports present silver nanoparticles with a spherical shape, with no focus on changing the morphology of the nanoparticles. However, Pal S. *et al.*[49] reports the influence of the shape on the antibacterial properties of silver nanoparticles, concluding that the facets (111) are beneficial. For this reason, we decided to change the shape of the nanoparticles in the nanocomposite and study their antibacterial properties, comparing them with AgNPs (spherical nanoparticles or triangular alone). On the other hand, most of the reports described use the chemical reduction method to synthesize AgNPs/GO nanocomposites, due to it is a quick and easy method of obtaining well-dispersed nanoparticles. However, this method does not allow control of the size and shape of the nanoparticles, and sometimes change the properties of graphene oxide resulting in reduced graphene. Thus, the photochemical reduction method is used to promote anisotropic forms containing the facet (111) as triangular nanoplates, and to maintain the properties of graphene oxide.

The aim of this research graduation project is to study the antibacterial properties of nanocomposite silver triangular nanoplates deposited on graphene oxide (AgTNPs/GO), and compared with AgNPs. This will be achieved through 3 steps; first the nanocomposite AgTNPs/GO is synthesized by a different, facile and low cost *in-situ* photoreduction method. Second, the nanocomposite is characterized with Scanning Electron Microscopy (SEM), Transmission Electron Microscopy (TEM), Raman Spectroscopy, UV-Vis Spectroscopy, and Photoluminescence (PL) techniques. Finally, AgTNPs/GO antibacterial properties are tested with the antimicrobial disk diffusion test and optical density, against E. coli as bacteria model. Experimental results showed that AgTNPs/GO nanocomposite enhanced the antibacterial properties as compared to AgNPs.

2.1   Problem Statement

Silver triangular nanoplates deposited on graphene oxide enhanced the antibacterial properties against E. coli than silver nanoparticles either spherical or triangular nanoplates, alone.

2.2   General and Specific Objectives

2.2.1   General Objective

Study the antibacterial properties of AgTNPs/GO nanocomposite.

2.2.2   Specific Objectives

- Synthesize the AgTNPs/GO nanocomposite.

- Characterize the AgTNPs/GO samples using: SEM, TEM, Raman, UV-Vis and PL techniques.

- Test and compare the antibacterial properties of AgTNPs/GO nanocomposite and AgNPs against E. coli.

Chapter 3

Characterization Techniques

3.1   Scanning Electron Microscopy (SEM)

Scanning Electron Microscopy (SEM) obtains two-dimensional topographic images with magnifications of 10 to 10,000x in various materials surfaces[71]. The operation of the SEM can be described by the working principle of the main components, and various subsystems[71]. Figure 3.1 shows the essential components of the SEM, which are the electron gun, the lens system, the electron detectors, and the Digital Image Scanning system (DISS).
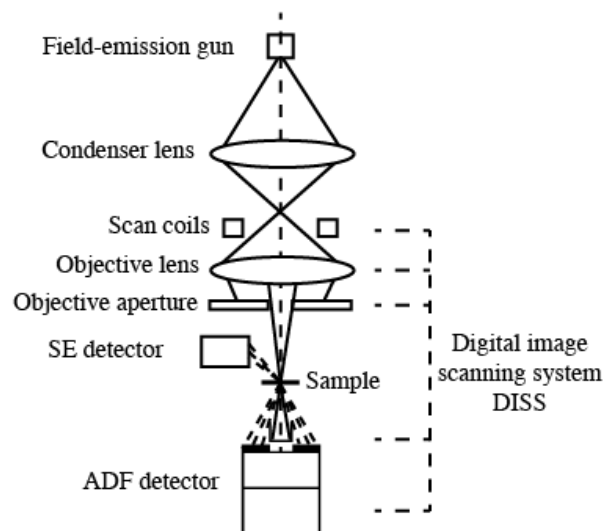
Figure 3.1: Typical lens system of a conventional SEM, electron gun, deflection system, apertures, DISS and the electron detector. Adapted from Krzyzanek V. *et al.*[72]

The area of the sample to be analyzed is irradiated with a finely focused electron beam, which can move across the surface of the sample to form images or can be static to obtain a spot analysis[73]. The electron beam is produced by an electron gun, which generates and accelerates the electrons to an energy in the range 0.1-30 keV[74]. This energy is adjustable to provide a stable beam of electrons[74]. The electron gun is responsible of the probe size at the sample, if it is large the image will be not sharp[73]. Therefore, a electrostatic or electromagnetic field is needed to focus the electrons[71]. Electromagnetic lenses are used due to its smaller aberrations, they demagnify the image of the beam crossover in the electron gun to promote sharpness[74]. There are two main types of electromagnetic lenses: condenser and objective.; condenser lenses controls the amount of demagnification for a particular imaging mode[73]. While objective lenses focuses the electron probe onto the sample surface, and contributes additional demagnification[71]. Between these lenses, there are the scan coils used to sweep the beam across the specimen[73]. Then, the objective aperture controls the aperture angle that minimizes not desired effects of aberrations on final probe size, promoting sharp images[73].

The final electron probe interacts with the sample at high depth of field allowing to obtain topographic images of the surface, as well as qualitative information of the elemental composition[74]. From the interaction of electron beam and specimen, a current is released and amplified to be collected by an electron detector[71]. The resulting current is mainly composed by scattered electrons, which are dependent of the measurement conditions (electron beam energy, probe size, demagnification, objective aperture), and sample composition[71].

As the beam electrons enter the sample, they interact as negatively charged particles with the electrical fields of the specimen atoms[73]. The beam-specimen interaction can deflect the beam electrons, causing them to scatter[73]. When the electrons leaves the specimen, the process is called backscattering[74]. Backscattered electrons results from an elastic scattering, where the kinetic energy is conserved[73]. The probability of elastic scattering increases strongly with atomic number, due to heavier atoms have a much stronger positive charge on the nucleus[73]. The beam electron loose energy while it is propagating through the sample, this energy is transferred to the specimen atoms causing inelastic scattered[73]. Inelastic scattering give useful imaging signals such as secondary electrons, and analytical signals such as rays[74]. For low atomic number, inelastic scattering is relatively more probable, the beam tends to penetrate the specimen and the electron energy decreases[71]. This decrease allows elastic scatters to occur now[71]. Backscattered and secondary electrons are the principal signals used to form images[73]. These signals carry information mainly about specimen composition and topography[73].

SEM images are formed by the simultaneous contribution of backscattered and secondary electrons signals[71]. Both scattered electrons travel through the specimen to get out or back to the surface, so they can be influenced by subsurface features[73]. Then, these electrons signals carry information about the topographic characteristics of specimen[74]. On the other hand, the probability of having backscattered electrons depends on the atomic number, therefore this signal carries information about the composition of the specimen[73]. SEM image is formed by the signals intensity derived from the electron detector, and they are used to adjust the brightness[73]. Brightness is responsible of the contrast in SEM images, and it is dependent of the variation of secondary and backscattered electrons over the surface of sample[71]. Figure 3.2 shows a SEM micrograph image example.
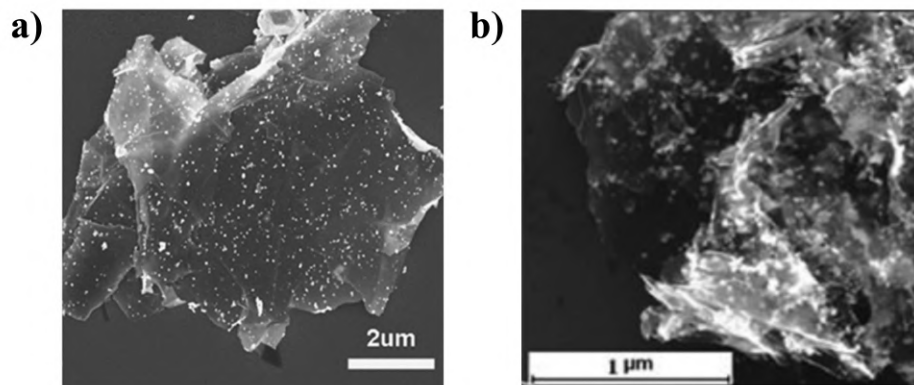
Figure 3.2: SEM micrograph example of silver nanoparticles deposited on graphene, adapted from Jiang B. *et al.*[40](a), and silver nanoparticles on graphene oxide, adatpted from Liu H. *et al.*[26](b).

Figure 3.2 (a) shows a graphene flake as a template for silver nanoparticles. Graphene flake is identified by a low brightness present in the micrograph, due to the low atomic number of carbon atoms[73]. Besides, topographic features of graphene flake can be seen owint to the contribution of backscattered and secondary electrons. On the other hand, silver nanoparticles are observed by they high brightness contrast due to its high atomic number[73]. White dots in the micrograph correspond to heavier silver atoms. Fig. 3.2 (b) exhibits silver nanoparticles deposited on graphene oxide. The micrograph reveals nanoparticles attached at the surface and edges of graphene oxide. Graphene is composed by carbon atoms, with a low atomic number, while silver nanoparticles has a high atomic number. Therefore, a high contrast image is obtained as Fig. 3.2 shown.

3.2 Transmission Electron Microscopy (TEM)

Electron microscopes were developed since optical light microscopes have limited image resolution[75]. Transmission Electron Microscopy is a technique in which an electron beam interacts and passes through an ultra thin-specimen[76]. Image resolution and information depend relatively of the initial conditions used in the equipment[76]. For this reason, is important to understand the working principle of TEM[75]. A conventional TEM consists of an electron gun, condenser and objective lenses and apertures, intermediate lenses, selected aperture area, projector lens, and imaging, as shown in Figure 3.3.
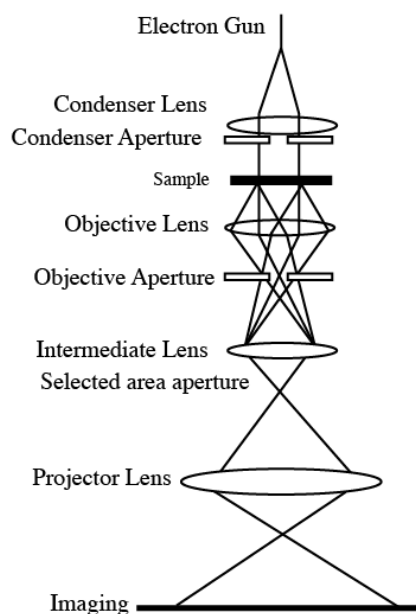
Figure 3.3: Typical lens system of a conventional TEM, aperture, deflection system and imaging. Adapted from Lubk A. *et al.*[77]

Electrons are emitted by an electron gun, their sources can be thermionic, which is based on heat a filament, field-emission which needs a large electric potential to produce electrons, and Schottky that combines both thermionic and field emission[75]. Then, electron lenses are needed to focus, change the intensity of illumination or change the magnification[78]. Figure 3.3 shows the condenser lenses after the electron beam, since they control the current ejected[75]. Next, a condenser aperture defines the size of the final beam, and therefore the angular range of the probe[78]. Then, the electron beam and the specimen interacts and electron scattering process take place[77]. Elastic scattering results from two interactions: electron-electron which produces relatively low scattering angle, and electron-nucleus that cause higher scattering angles[78]. Other type of electron scattering is an inelastic way, in which some of the incident electron beam lose energy[79]. Since electrons beam interacts with the atoms of the specimen, specifically with the conduction or valence bands, secondary electrons are also ejected[75]. Other types of inelastic scattering signals are rays or Auger electrons, emissions caused by an ionized atom returning to its ground state[78].

The electron beam passes through the sample and is focused by the objective lenses[75]. Objective lens form the images, and it is also the most difficult to construct since the specimen is close[75]. Then, the objective aperture below the objective lens allows to control the resolution of the image formed by the lens, depth of field and focus, the image contrast, and so on[78]. Next, intermediate lens are used to magnifying and it determines whether the viewing screen of the microscope shows a diffraction pattern or an image[76]. For diffraction pattern a selected area aperture is required, due to it can limit the region which generates the diffraction pattern[80]. After this, a

projector lens is used to magnified the image and to project it onto the phosphorus screen[75]. Finally, the resulting information that can be obtained is about the topography of the sample or diffraction pattern of a selected area[78]. Image mode can be formed using the central spot or all of the scattered electrons[75]. There are two types of image modes; bright-field and dark-field, and these are dependent of the intermediate lens strength[78]. For bright-field image mode, the direct beam is selected. While for a dark-field image just electrons outside of the direct beam are selected[75].

Small magnifications image contrasts are due to the absorption of electrons that depends on the thickness and composition of the specimen[76]. In contrast, at high magnifications, the wave interactions modulate the intensity of the image[76]. The different modes allow TEM to observe crystal orientation, electronic structure, chemical identity, and regular absorption-based imaging[80]. Figure 3.4 presents two example of a bright-field TEM micrograph showing silver nanoparticles deposited on graphene oxide flake (a), and silver nanoprims(b).
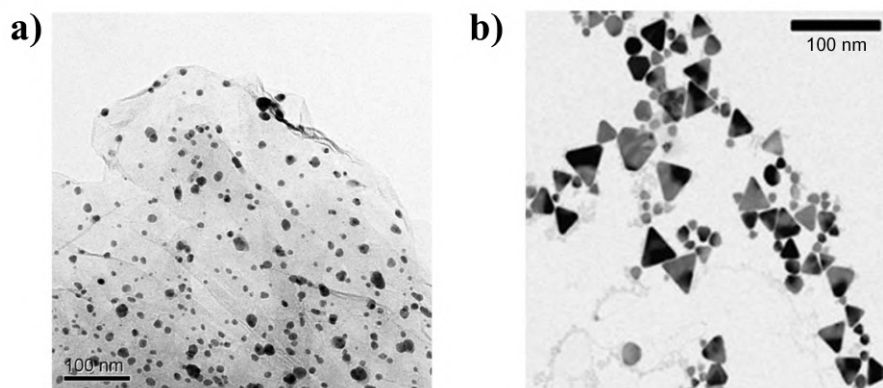

Figure 3.4: Bright-field TEM micrographs examples of silver nanoparticles deposited on graphene oxide adapted from Song B. *et al.*[51](a), and silver nanoprisms adapted from Saade J. and Araujo C.[11](b).

Fig. 3.4 (a) shows silver nanoparticles deposited on graphene oxide. Graphene oxide flake appear with a low contrast due to the low atomic number of carbon atoms that composed the graphene layer. While silver nanoparticle due to their high atomic number[78], presents high contrast as black dots. Fig. 3.4 (b) reveals silver nanoprisms with several anisotropic shapes as triangles. Darkness is used to evaluate the thickness of the silver nanoprisms. The darker it is, the thicker the nanoprisms. More information about the thickness can be obtained by tilting the sample[78].

3.3 Raman Spectroscopy

Raman is the interaction study between a kind of radiation and matter in the function of wavelength[81]. When light interacts with matter, the photons may be absorbed or scatter, or may not interact with the material[81]. For the

absorption process the photon requires to have the energy gap between the ground state of a molecule and an excited state[82]. While for scattering process the photon does not need to has the energy gap, and the the scattered photons can be observed by collecting light at an angle to the incident light beam[81]. The scattering process is originated from a polarization induced in the molecule by the oscillating electric field of the incoming light[83]. In the scattering process the incident light interacts with phonons or other excitations of the system molecules, causing a shift in the photons energy[83]. These shifts gives information about the vibrational modes of the molecules in the system[82]. Figure 3.5 shows possible vibrational modes of molecules.
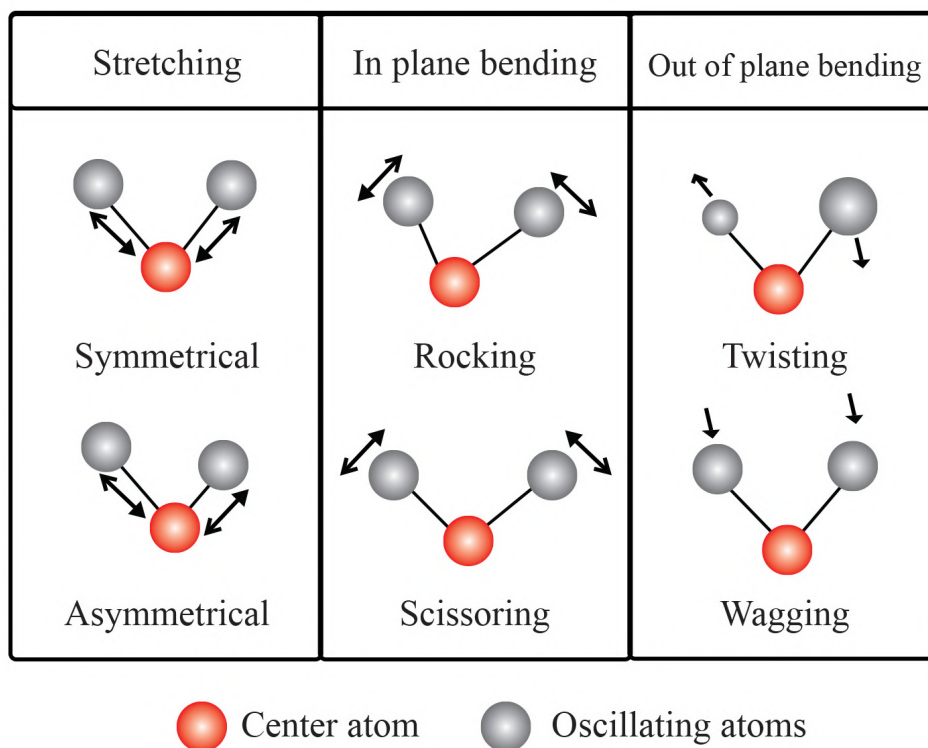
Figure 3.5: Possible vibrational modes of triatomic molecule when they are excited with an incident light beam. Adapted from Mohammad J.[84]

Figure 3.5 shows three different possible vibrational modes for molecules with three atoms. The first vibrational mode is the stretching, in which the oscillating atoms moves symmetrical and asymmetrical with respect to the center atom[84]. Symmetrical oscillation of atoms involves a movement of them in the same direction. While asymmetrical oscillation shows atoms moving in opposite directions[84]. The second mode is In plane bending, two types of this mode are shown; rocking that describes an asymmetrical lateral oscillation-while one atom turns sideways to the left, and scissoring in which the movement of atoms are in same-directional synchronized[81]. The third mode is the

out of plane bending, this has two types of oscillation: the first is the twisting in which the atoms are moving in op-posite directions, on and off the plane. The second is the wagging where atoms oscillates both in the same direction[84].

To excite the electrons of molecules, an incident beam of monochromatic light (laser) in the visible, near, infrared or near ultraviolet, is used[82]. Usually it is discussed in terms of radiation[81]. Radiation is characterized by its wavelength, since Raman spectroscopy analyse vibration of molecules present in a sample, results will be in terms of energy, then it is expressed as a frequency or wavenumber scales[81]. Raman spectroscopy uses a single frequency (monochromatic) of radiation to irradiate the sample, then it is scattered from the molecule changing its energy what is detected[83]. Depending of the frequency detected, there are different scattering process such as: Stokes, Rayleigh, and anti-Stokes. Figure 3.6 shows the scattering process for one molecule vibration.
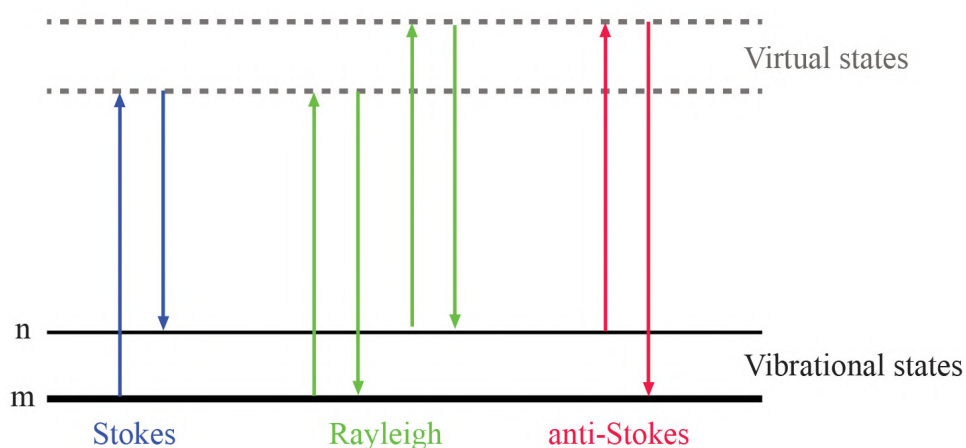
Figure 3.6: Stokes, Rayleigh, and anti-Stokes scattering processes for one molecule vibration. Adapted from Smith E. *et al.*[81]

Fig.3.6 shows three scattering processes: (i) Stokes scattering occurs when the electron is excited with the incident beam, and it scatters in an inelastic way, in which it loose energy as a phonon[83]. Fig. 3.6 shows the excitation of the electron from the ground state m to virtual excited states, then the electron returns to the n level and not to the m due to the loss of energy[83]. (ii) Rayleigh scattering happens when the electron excited scatters in an elastic way, which means that the electron does not loose energy and follow a recombination process[81]. In the Fig. 3.6 this process is shown as green arrows indicating that the electron returns to the initial ground state m. Anti-Stokes scattering is the result of an inelastic scatter of the electrons, in contrast to Stokes scattering, in this process the electron is already in an excited state n, then it gains energy as phonon[81]. With the gain of energy, it is capable to return to the ground state m[81].

The working principle of experimental measurements is explained in Figure 3.7:
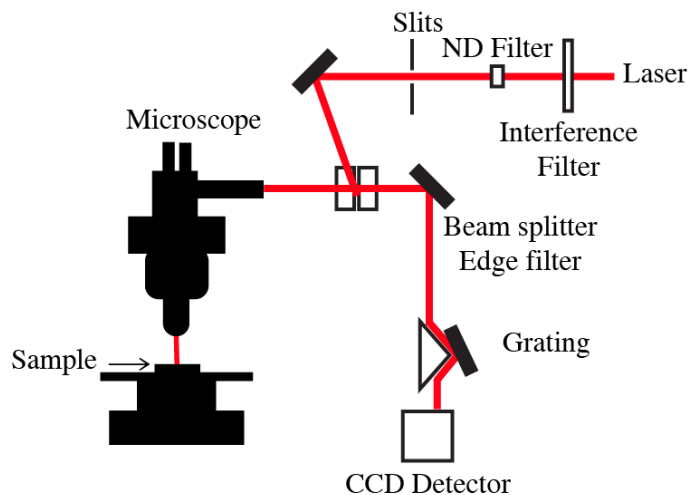
Figure 3.7: Raman spectrometer and microscope, using a visible laser, notch filter, spectrometer, Neutral Density Filter (ND)and CCD detector.

A pinhole focuses on the laser, and it is collected as a parallel beam to fill the optics of the microscope[81]. This is due to the plasma filter removes weak emission and background radiation from the laser[85]. Then, the radiation passes through a notch filter, which is an interference one, and works well when the beam is perpendicular to the filter[85]. The light is completely reflected in the microscope, and the scattered radiation is collected[81]. Finally, the light is then passed into the monochromator and onto the CCD detector[81].

Raman scattering is widely used to provide information on chemical structures, to identify substances from the characteristic spectral patterns called "fingerprinting."[81]. Raman spectra shows peaks at specific wavenumbers which represents different vibrational modes of the material[86]. The amount of the substances present in the sample are determined qualitatively or semi-qualitatively by Raman spectra[82]. A Raman spectra consists of scattered intensity-dependent of the energy, each peak corresponds to a given Raman shift from the incident light energy[81]. The range in which it works is in the visible range between ultra-violet and infrared spectra[83]. Figure 3.8 shows two examples of Raman spectra for graphite, graphene, graphene oxide and reduced graphene with silver nanoparticles.
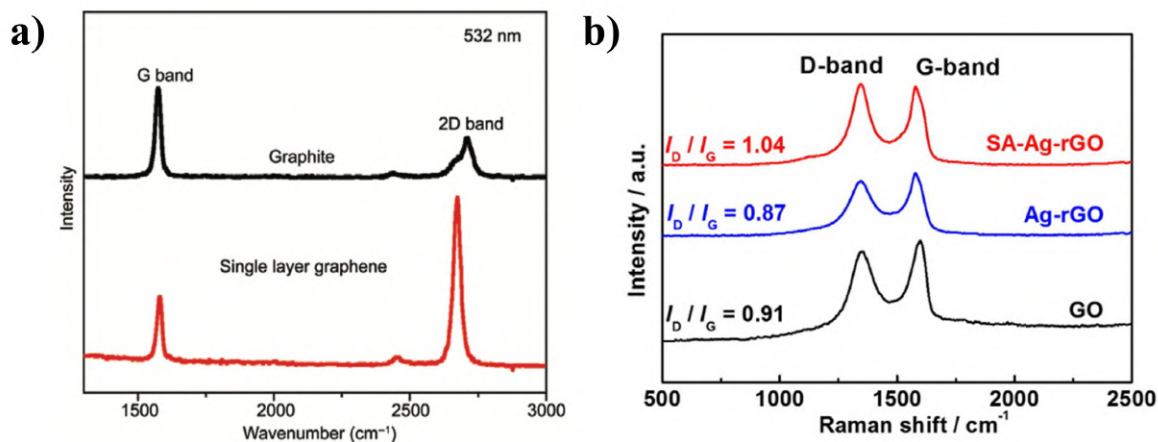
Figure 3.8: Raman spectra of graphite and graphene (a), and comparison between reduced graphene with silver nanoparticles Ag/rGO and graphene oxide (GO). Adapted from Ni Z. *et al.*[87] and Lou X. *et al.*[64], respectively.

Figure 3.8 (a) shows the spectra of graphite, which exhibits the characteristic G and 2D bands coming form the vibrational modes of graphene[87]. Also, single-layer graphene is presented. Fig. 3.8 (b) reveals Raman spectra of reduced graphene with silver nanoparticles (Ag/rGO) and graphene oxide (GO). Both spectra show the D and G band peaks, which are attributed to the defects of the GO structure, and the bond stretching of carbon sp^2 atoms[87], respectively. Also, Fig.3.8(b) shows the I_D/I_G ratio that corresponds to the D and G band intensities for characterizing the disorder of the graphitic structure in carbon materials[64].

The vibrational modes corresponding to the G, D, and 2D bands of graphene Raman spectra are shown in Fig. 3.9
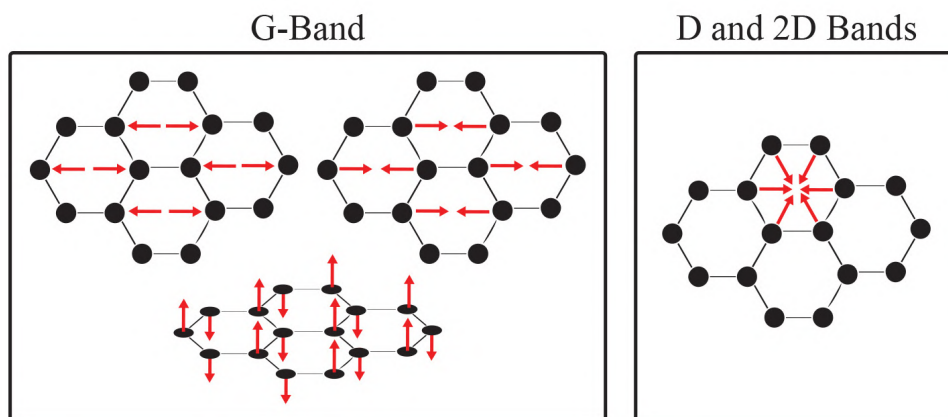
Figure 3.9: Vibrational modes of graphene which generates the G and D band of Raman spectra. Adapted from Wagner S. *et al.*[86]

G band comes from the vibrational modes shown in Fig. 3.9, in plane vibrations are the two modes that are up, lateral vibrations towards the centre of each hexagon and outwards can be seen[86]. While out of plane mode corresponds to the one on the bottom and the vibrations are observed vertically out of plane[86]. For D and 2D bands the vibrational mode is directed to the center of an carbon hexagon, note that the atoms vibrate just in one direction since other hexagons do not vibrate[86].

3.4   UV–Visible Spectroscopy (UV–Vis)

The importance of spectroscopy in the industry field of liquids, lies in the determination of the concentration of solid material diluted in a liquid medium[88]. Besides, through the refractive index this technique can provide detailed information about the properties of the molecules, and it is used in the physical and chemical sciences[89]. UV-Vis spectroscopy received its name due that it works in the visible range of the spectra, which goes from 300 nm to 700 nm[88]. The measuring principle consists of a beam of light of intensity I_0 incident on some absorbing sample, only a small fraction of the light is absorbed (assuming that losses caused by light scattering are negligible) and the transmitted light intensity I follows the Beer-Lambert law:

$$A = log(\frac{I_0}{I}) = \varepsilon(v)cl \tag{3.1}$$

where A is known as the absorbance[88]. The absorbance is directly dependent on the concentration (c) of absorbing species, the optical path length (l), and the molar absorption coefficient (ε)[89]. The molar absorption coefficient is a measure of the intrinsic absorbing power of the sample to analyze, and is frequency dependent ($\varepsilon(v)$)[89].

The interaction of the electric field with a liquid phase is essential, and the magnetic field interaction is usually neglected in practical optical metrology[90]. An external electric field, such as light can disturb the charge distribution of electrons resulting in a coulombian interaction[88]. The interaction of UV−Vis light with liquids is related to electronic polarization[88]. This depends on the displacement of electrons concerning the nucleus of an atom[89]. The displacement is caused by the distortion of the electron cloud that move around the nucleus[90]. The electronic polarization of charges occurs in all dielectrics[88].

The spectra is measured with an absorption spectrometer which has a scheme showed in figure 3.10.
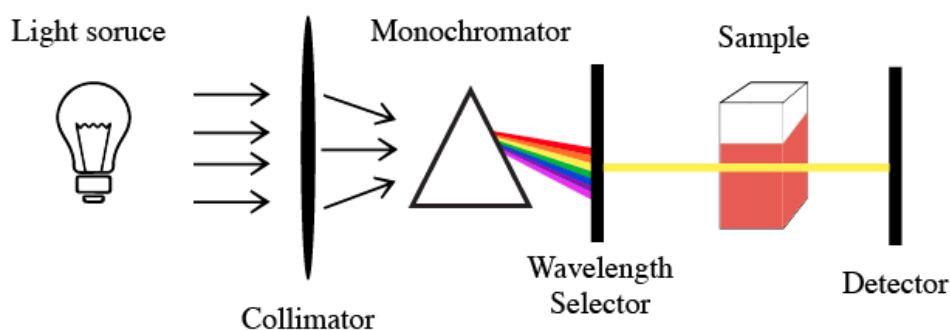
Figure 3.10: Schematic of a conventional grating-based absorption spectrometer, light source, collimator, monochromator, wavelength selector and detector.

Ideally, the light source is continuous over the region of interest, and resistively heated filaments (as tungsten) are good sources of near continuum light[88]. A wavelength selector is central to the spectrometer, the most used is a monochromator built around a diffraction grating, allowing tunability[89]. The spectra obtained is a function of the light intensity transmitted through the monochromator and dependent on the incident radiation[88]. The light intensity is measured by a photomultiplier tube (PMT), a photodiode, or some other light-detecting device[89].

From the perspective of nanotechnology, the incident light beam interacts with nanomaterials such as nanoparticles[91]. The electric field applied cause a oscillation of the free conduction electrons located at the surface of the nanoparticles[14]. Figure 3.11 shows the oscillation of free conduction electrons at the surface nanoparticles due to the effect of the external electric field applied[91]. Figure 3.11 exhibit the oscillation of electrons with respect to the nucleus of a nanoparticle.
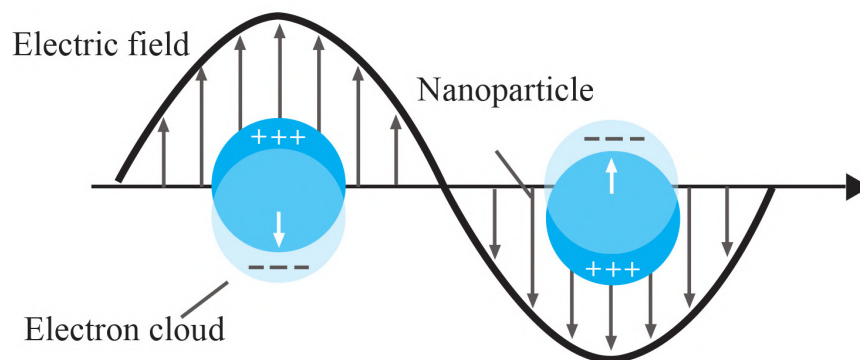
Figure 3.11: Oscillation of free conduction electrons with respect to the nanoparticle nucleus due to an external electric field applied. Adapted from Kumar C.[91].]

In the Fig. 3.11 we can observe the electric field as a wave, the spherical nanoparticle like the blue circle, the oscillations of electrons as the light blue circle with the charges densities, and the electron cloud negatively charged. When the electrons oscillate coherently with the electric field, a surface plasmon resonance is produced[14]. Different surface plasmons resonances can be generated depending of the particle composition, size, and shape[17], as Fig.1.3 shows. An example of a UV-Vis spectra for silver nanoparticles and silver nanoplates is shown in Fig. 3.12.
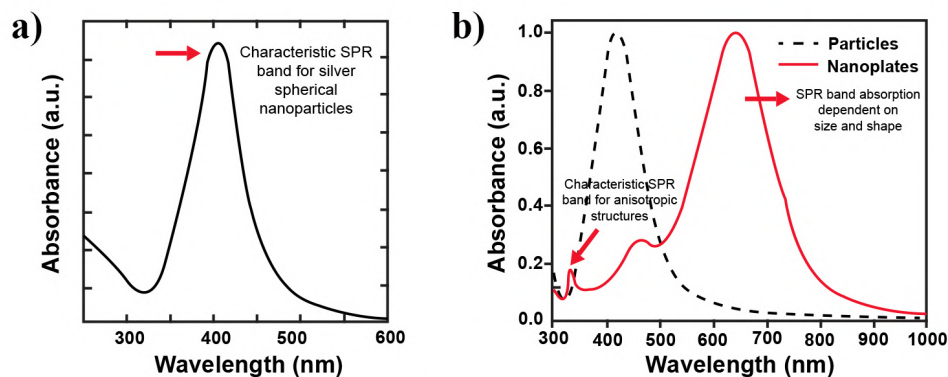
Figure 3.12: Examples of UV-Vis spectra of silver nanoparticles (a) adapted from Liu H. *et al.*[26], silver nanoparticles and silver nanoplates adapted from Zhang Q. *et al.*[19].

Fig. 3.12 (a) exhibits a common spectra for silver nanoparticles; the principal absorption band is centered at 400 nm, according to Liu H. *et al.*[26]. Fig. 3.12 (b) shows a comparison spectra between silver nanoparticles and silver nanoplates. As well as Fig. 3.12 (a), silver nanoparticles present an absorption band centered at 400 nm, while silver

nanoplates exhibits two absorption bands, one at ≈ 330 nm characteristic of anisotropic structures, and the second at ≈ 650 nm corresponding to a surface plasmon resonance mode dependent on size and shape of silver nanoparticles[14]. According to Mies theory[92], only a single SPR band is expected in the absorption spectra of spherical nanoparticles. In contrast, anisotropic particles could give rise to two or more SPR bands depending on the shape of the particles[49]. Besides, broadening changes in the absorption bands means a variation of the size distribution, and therefore an increase or decrease of the nanoparticles and structure sizes[6]. Another indicator of nanoparticle size is the shift to higher (big) or lower (small) wavelengths of the visible spectra[6].

3.5 Photoluminescence (PL)

The optical behavior of the materials has critical characteristics as the level of oxidation, size, and shape[93]. The photoluminescence phenomenon is the process in which the valence electrons at the surface of a nanoparticle are excited when they absorbs a photon (in the visible region)[91]. Then, the excited electrons return to a lower stable energy releasing energy in a photon way[91]. Figure 3.13 shows the two types of photoluminescence: absorption and emission.
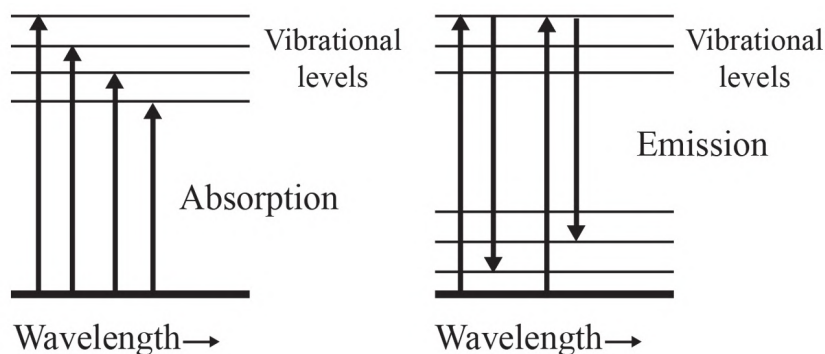
Figure 3.13: Absorption and emission process in Photoluminescence. Adapted from Kumar C. *et al.*[91].

Fig. 3.13 shows the two photoluminescence process: the absorption when the electrons absorb the photons and leads an excited state, and emission when the excited electrons return to a lower energy level realising energy in a light way[88]. Besides, the dependence of the irradiation wavelength is presented[91]. For absorption-at higher wavelengths, the electrons excited leads to higher energy vibrational levels, while for emission process- at higher wavelengths, the excited electrons return to increasingly stable levels[91].

Emission light photoluminescence is a radiative process and it works in the ultraviolet and visible regions[75]. The photoluminescence emission spectra comes from the measurement of the intensity of emitted radiation. Radiation is a function of either the excitation wavelength or the emission wavelength. For the emission spectra, a fixed wavelength is used to excite the molecules, and the intensity emitted is recorded as a function of wavelength[94]. The PL emission spectra can be obtained by steady-state PL measurements, time-resolved PL, and quantum yield[91]. A

basic scheme of instrumentation is shown in Figure 3.14.
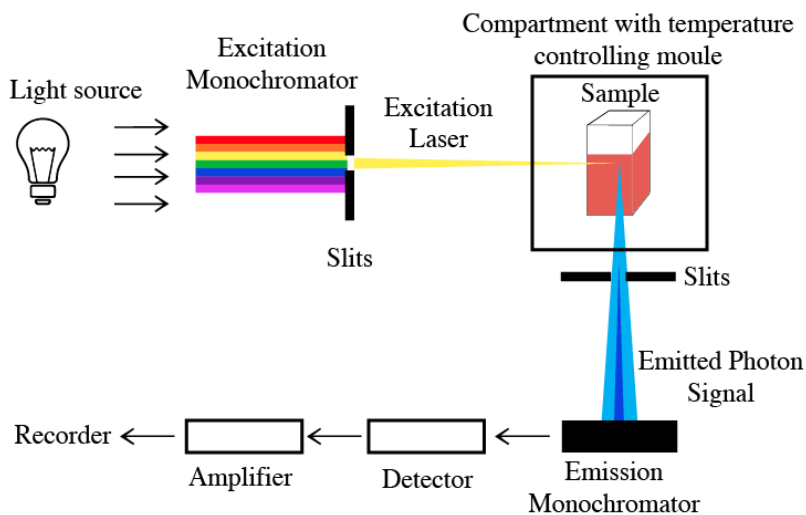
Figure 3.14: Schematic of a conventional fluorescence spectrometer. Adapted from Harris D. *et al.*[95]

Fig. 3.14 presents an schematic of a conventional fluorescence spectrometer. An excitation wavelength is selected by one monochromator, usually positioned at 90° to the incident light to minimize the intensity of scattered light reaching the detector[95]. Then, the sample is irradiated with the excitation wavelength and the photoluminescence emission process occurs[91]. If the excitation wavelength is fixed and the emitted radiation is scanned, an emission spectra is produced[95]. Emitted light passes through an emission monochromator, and finally emission light is detected and amplified to be recorder[95].

Figure 3.15 shows PL spectra for silver nanoparticles (Ag), graphene oxide (GO), and silver nanoparticles with graphene oxide (GO-Ag) samples.
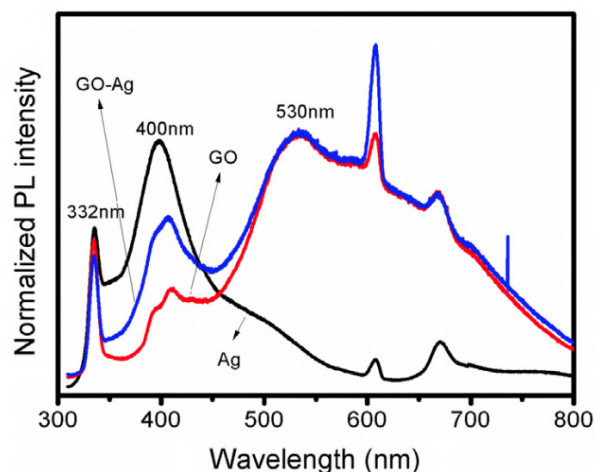
Figure 3.15: Example of PL spectra of silver nanoparticles (Ag), graphene oxide (GO), and silver nanoparticles with graphene oxide (GO-Ag). Adapted from Lan N. *et al.* [93]

Figure 3.15 shows a PL spectra for Ag showing a main characteristic peak at 400 nm. GO exhibits a strong peak at 530 nm attributed to the boundary of oxidized carbon atoms [93]. Finally, GO-Ag spectra shows two peaks: the first at 400 nm corresponding to silver nanoparticles, and the second at 530 nm attributed to graphene oxide. The weak peak at 332 nm is due to water [93].

3.6 Antimicrobial Disk Diffusion Test

The publication on penicillin by Alexander Fleming in 1928 is a milestone in the history of medicine [96]. Antimicrobial compounds were discovered owing to eliminate infectious diseases; unfortunately, the development of bacterial resistance to these antimicrobials [97] results in the need for physicians to request the microbiology lab to test a patients pathogen against various concentrations of a given antimicrobial to determine susceptibility or resistance to that drug [96]. Antimicrobial disk diffusion procedure is used to determine the susceptibility of bacteria to antimicrobials [98].

Different procedures are proposed depending on the needs in the laboratories, the factors that can be varied are media, inoculation concentration, incubation time, incubation temperature, and concentration of the antimicrobial compound [96]. The analysis of susceptibility and resistance are based only on the presence or absence of a zone of inhibition surrounding the disk [99]. Figure 3.16 shows an illustration of the antimicrobial disk diffusion test.
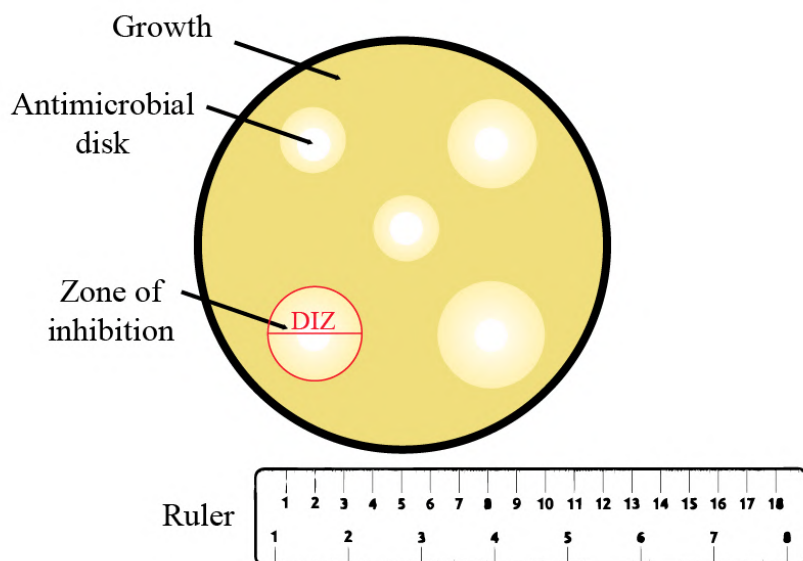
Figure 3.16: Illustration of the anitmicorbial disk diffusion test. The growth of bacteria is presented as yellow, the antimicrobial disk corresponds to the white color as well as the inhibition zone.

The diameter of the inhibition zone is related to the susceptibility of the diffusion rate of the drug through the agar medium[100]. These results are qualitative, the advantages of this test method are the test simplicity that does not require any special equipment, flexibility in the selection of disks for testing[100], and rapid results for the determination of antibacterial activity. Figure 3.17 shows an example of the antimicrobial disk diffusion test for silver nanoparticles.
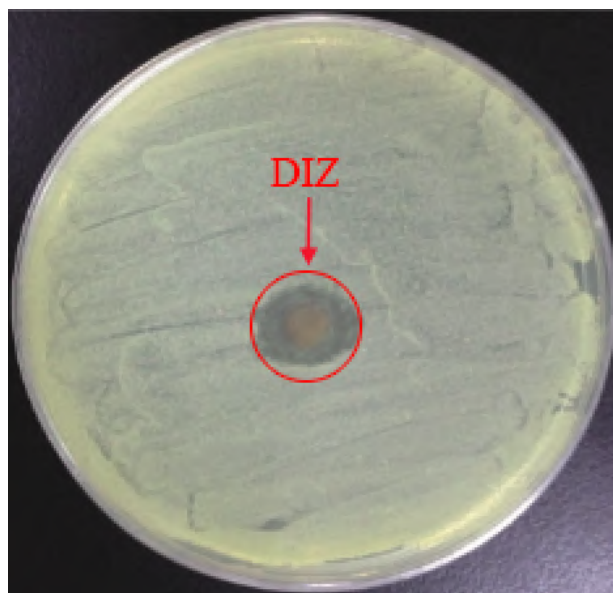
Figure 3.17: Example of antimicrobial disk diffusion tests for silver nanoparticles, where diameter of inhibition zone is the halo in the agar petri plate. Adapted from Huang L. *et al.* [39].

Fig. 3.17 exhibits a petri dish with cell culture as white background, and the diameter on inhibition zone (DIZ) identified by the halo. It is indicated by the red arrow and marked with a the red circle. A real interpretation of resistance and susceptibility to antimicrobials is determined through in vivo testing of blood and urine. These to calculate the level of a given antimicrobial that results in the resolution of an infection [96].

3.7 Optical Density (OD)

The absorbance is directly dependent of the concentration and chemical composition of the sample, so it is used in the analytic chemistry for the characterization of liquids. The optical density is the measurement of the absorbance per unit of length that the light travels when it passes through the sample, this is described in the following equation [101]:

$$OD_\lambda = \frac{A_\lambda}{l} = \frac{1}{l} log \frac{I_0}{I} \tag{3.2}$$

In the case of homogeneous colloidal suspensions, the optical density is a function of the concentration, equivalent to absorbance values. Equation 3.2 presents l being the sample thickness, I_0 initial absorbance, and I final absorbance value [102]. The optical density is useful to describe the dynamics of bacterial growth, where the bacterial density is defined as the dry weight of cells per unit volume of a culture or as the number of doubling of bacterial density per unit time [103]. The curve obtained illustrates the events occurring through time, and it is shown in figure 3.18.
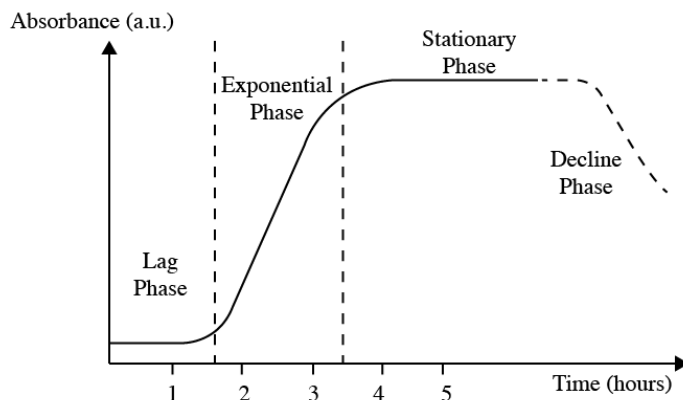
Figure 3.18: Bacterial growth curve showing the four phases: lag, exponential, stationary and decline phase. Adapted from Huang L. *et al.* [39]

Figure 3.18 describes the dynamics when a sample of bacteria cells is transferred to a tube of fresh broth (nutrient), and four phases are distinguishable: the lag phase, the exponential phase, the stationary phase, and the decline phase [103]. The lag phase is the first portion of the curve and represents the time in which the bacterial cells are adapting to the new environment (nutritional conditions), some of them die, and others take up nutrients and replicate their DNA [104]. The length of the lag phase depends on the metabolic activity of the microbial population. The exponential phase is given by the exponential growth of bacteria cells, which are also undergoing binary fission [103]. The number of cells doubles, and the stage rises in a logarithmic shape. Balanced growth is present because the metabolism and physiology remain constant [104]. In this stage, the application of antibiotics is visible due that it affects the metabolic processes. The stationary phase shows the limitation of nutrition sources, therefore over time, the broth starts having scarce, and waste products accumulate, and the cells enter a plateau [104]. Now the number of viable cells equals the number of nonviable cells [103]. Finally, the decline phase is due to that the cells enter a death phase, where the number of viable cells declines logarithmically. Also, there is the possibility that few members of the population can escape death by entering a state of dormancy [104]. An example of microbial growth obtained through optical density measurements is shown in Figure 3.19.
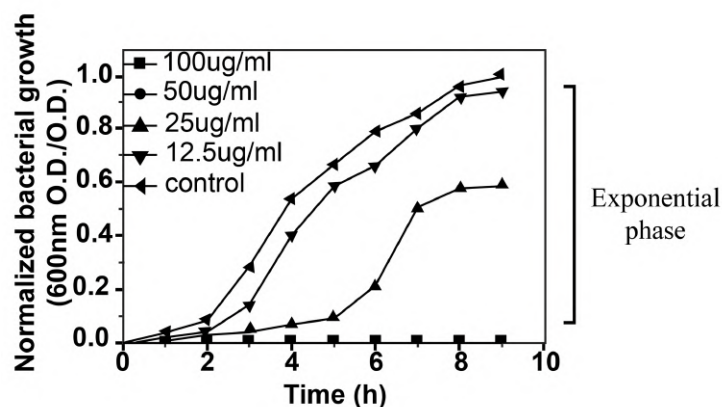
Figure 3.19: Example of a bacterial growth curve for silver nanoparticles with different silver precursor concentration. Adapted from Xu W. *et al.*[50].

Figure 3.19 shows two main phases: the lag phase and the exponential. The curves reveal that: highest concentration of silver precursor, highest antibacterial efficiency results. The bacterial growth can be quantified with three main growth constants: total growth, exponential growth rate, and the lag time and growth lag. The total growth is the difference between initial (x_0) and maximum (x_{max}) bacterial density[103].

$$G = x_{max} - x_0 \tag{3.3}$$

The exponential growth rate (R) is given by the expression

$$R = \frac{log_2 x_2 - log_2 x_1}{t_2 - t_1} \tag{3.4}$$

The exponential growth rate is a general and sensitive physiologic test which can be used for the study of effects, and quantitative interpretations[103].

Chapter 4

Methodology

4.1 Chemicals

Hydrogen peroxide (H_2O_2) 30 wt% and Trisodium citrate (TSC) 99% were purchased from Lobachemie. Silver nitrate ($AgNO_3$), Sodium borohydride ($NaBH_4$), and Polyvinyl alcohol (PVA) were purchased from Sigma Aldrich. Ammonium hydroxide (NH_4OH)1% was purchased at M&M representations. All chemicals were used as received without further modification, and they were of analytical reagent grade. Demineralized water TDS 5 ppm was obtained at a local store, and 0.5 g Graphene oxide powder was obtained from Abalonyx Innovative materials[105] with a C/O atomic ratio = 2.5 - 2.6. Requires an ultrasound bath 0.5 h to form a dispersion. When diluted to 0.1 weight % the suspension has a pH of 2.9. Miller Luria Bertani Agar (LB AGAR) TM MEDIA 40 g/L was purchased from Novachem as well as Lennox L Broth Base (LB Broth Base) Invitrogen 20 g/L. Gram-negative (G−) bacterial strain E. coli glycerol TG1 was performed according to the book Combinatoria Molecular[106].

4.2 *In-situ* method for AgTNPs/GO

4.2.1 Light chamber cameras

High power light emission diodes LEDs chambers were designed, taking into account the procedure done by Saade & de Araújo[11]. High power LEDs (5 W) were used as the light source for the photoconversion. These chambers were made using PVC, aluminum foil, and high power LEDs. LED chambers setup is shown in Figure 4.1.
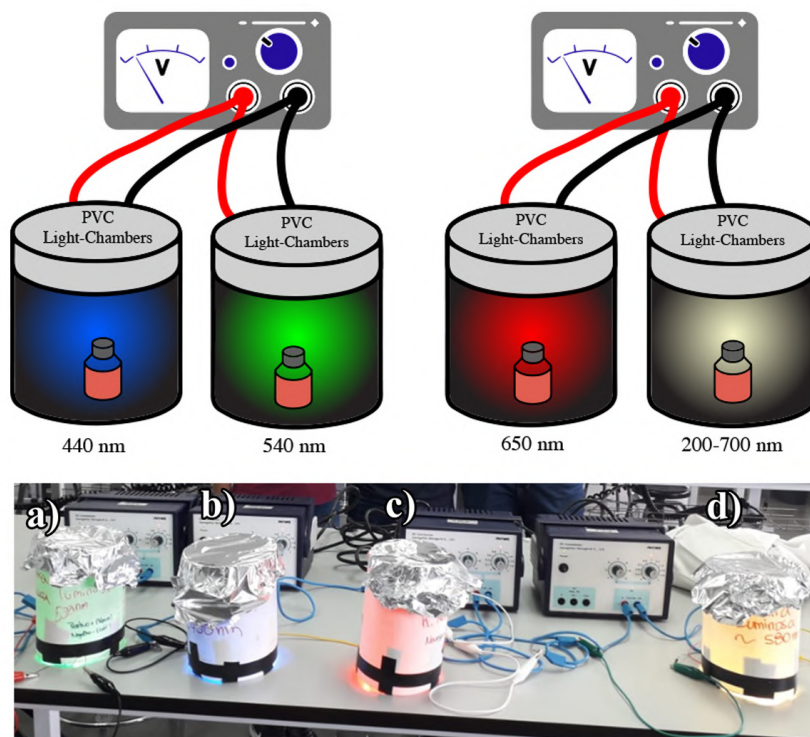
Figure 4.1: High power LED chambers setup. Two chambers were connected in parallel to a power supply.

PVC tubes, aluminum foil, and high power LEDs were purchased at a local store. PVC dimensions were 17 cm of longitude and 11.5 cm of diameter. Inside PCV tubes, 6 high power LEDs (connected in parallel) were placed equidistant, forming a ring at the bottom of the tube to promote an equidistant energy fluence and better size distribution[12]. To avoid external radiation, aluminum foil was put at the top of the PVC tube and secured with tape as Fig. 4.1 shows. PVC chambers with LEDs are connected: between them in series, and to the power supply in parallel.

Different LEDs color were used, corresponding to the wavelengths at: 440 nm, 540 nm, 650 nm, and 200-700 nm. The wavelengths were chosen according to ones reported by Saade J. & de Araújo C.[11] work. The power of the LEDs is 3 W, and the applied current was 0.7 A. The viewing angle at which can be viewed with acceptable performance is 120°.

4.2.2   AgTNPs/GO *In-situ* Photo-chemical reduction method

The photo-chemical reduction method is described as a two step process: wet chemical synthesis and photo–reduction.

Wet chemical synthesis

The preparation of the following solutions performed chemical synthesis: 10 mL $AgNO_3$ (0.05 M), 10 mL TSC (75 mM) and 10 mL $NaBH_4$(100 mM). Hydrogen peroxide solution was used as received without changing its concentration.

In a typical reaction, 28.474 mL of demineralized water was put into a 50 mL beaker. Then, 150 μL of $AgNO_3$ and 400 μL of TSC were added and vigorously stirred for 3 min. Then, 4 μL of $NaBH_4$ was rapidly added, leading to a light yellow solution. After 2 min of stirring, 60 μL of (H_2O_2) were added, converting the yellowish solution to a colorless one. Next, 250 μL of $NaBH_4$ was rapidly injected, leading to a fast change in colors that ended up in reddish yellow as Figure 4.2 shows.

Figure 4.2: Silver nanoparticles final color solution of the wet chemical synthesis.

Fig. 4.2 reveals the final color after the we chemical synthesis of siver nanoparticles in an eppendorf tube. A reddish color is observed and it depends on the components used to synthesize silver nanoparticles. For samples of triangular silver nanoparticles (AgTNPs). Reddish final color solution will be further referred as silver nanoparticles (AgNPs) suspension.

Graphene oxide

To reach GO 0.1 wt% and dispersion, 10 mL PVA (1 wt%) was prepared. 100 μL of PVA was put into a glass flask, and 9,9 mL of water was introduced to the suspension. Then, 0,013 g of GO are dispersed on it. Finally, the glass flask was put under sonication for 2 h at room temperature. Figure 4.3 shows the graphene oxide dispersed in water and PVA.

Figure 4.3: Graphene oxide dispersed in water and PVA suspension.

Fig. 4.3 shows a brown color solution, characteristic for GO dispersion[28]. The dispersion of GO flakes is to promote low number of GO layers.

AgNPs/GO nanocomposite

To obtain the initial nanocomposite, silver nanoparticles deposited on graphene oxide (AgNPs/GO), 50 μL of NH_4OH, as a ligand, was added to the AgNPs solution. Next, 976 μL of GO dispersed were introduced. This final solution will be further referred as AgNPs/GO initial nanocomposite solution.

AgTNPs and AgTNPs/GO nanocomposite by *in-situ* Photoreduction method

For silver triangular nanoplates AgTNPs, first, the AgNPs solution synthesized in the wet chemical method was divided into 4 vials. These vials were put inside the LED chambers, and they were irradiated for 16 h. The photoconversion of silver triangular nanoplates (AgTNPs) prove that the proposed photoreduction method converts spherical nanoparticles into triangular nanoplates. Once the photoreduction method works, it is applied to the AgNPs/GO to obtain AgTNPs/GO.

For silver triangular nanoplates deposited on graphene oxide AgTNPs/GO, first, the AgNPs/GO initial nanocomposite solution was divided into 4 vials. These vials were put inside the LED chambers, and they were irradiated for 16 h. All irradiated samples ended with a different solution color. The same photoreduction assembly is used for AgTNPs/GO, as shown in Fig. 4.1. An illustration of the *in-situ* method steps is presented in figure 4.4.
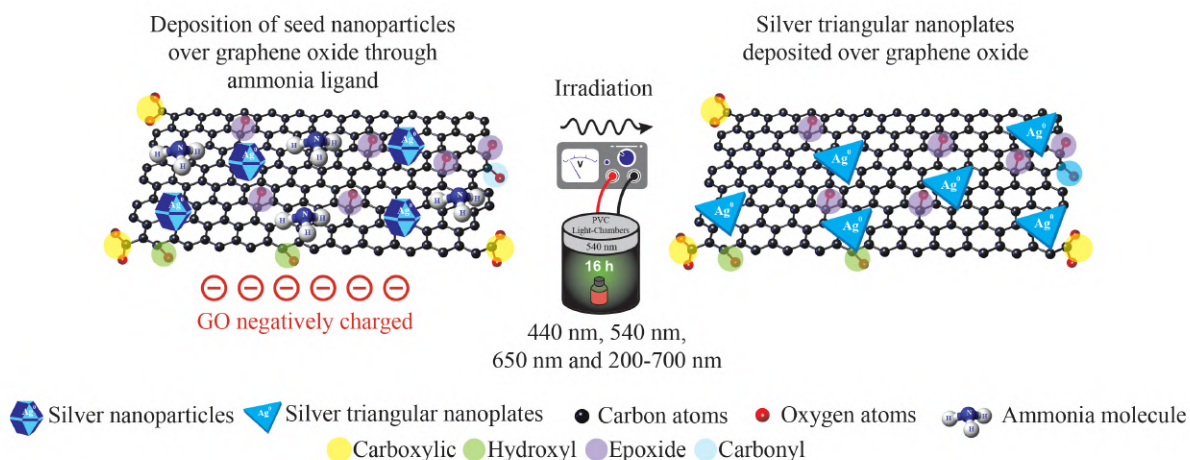
Figure 4.4: Illustration of the main three steps followed for the *in-situ* method of AgTNPs/GO.

After the wet chemical synthesis of silver nanoparticles, these are deposited on graphene oxide through the ammonium hydroxide ligand. Ligand is positively charged and by electrostatic attractions will promote the deposition of AgNPs on negatively charged GO. Then, this initial nanocomposite is irradiated with different wavelengths for 16 hours inside a PVC light chamber connected to a power supply. Finally, the silver nanoparticles are photoconverted to silver triangular nanoplates by photoreduction and in the presence of graphene oxide. This process is called as *in-situ* photoreduction method, in this project.

4.3 Antibacterial properties Tests

4.3.1 Antimicrobial Disk Diffusion Test

To prepare the liquid medium, 4 g of LB Broth base was mixed with 200 mL of distilled water and autoclaved for 1 h. For the solid medium, 5 g of LB AGAR was dissolved in 125 mL of distilled water in a glass bottle. Then, the bottle was autoclaved for 1 h. 100 μL of E.coli bacteria and 2 mL of liquid medium was inoculated in a shaker at 37 °C, 150 rpm for 24 h. After preparing the solid medium, it was evenly distributed in the Petri dishes and allowed to cool and solidify. Next, 150 μL of E.coli inoculation was well dispersed and let it dry. Then, 3 μL of ampicillin Amp^{-3} 0.05 g/L (as the control) and 3 μL of the graphene oxide (GO), silver nanoparticles (AgNPs), silver triangular nanoplates (Ag TNPs) and nanocomposite Ag TNPs/GO was placed over the bacterias in the Petri dishes. Finally, the Petri dishes were put under incubation at 37 °C for 24 h.

4.3.2   Optical Density (OD)

A bacteriological handle of E.coli was obtained from culture and inoculated with 2 mL of liquid medium (same procedure of above section) in a shaker at 37 $^\circ C$, 150 rpm for 24 h. The blank was prepared with 100 μL of the E.coli inoculation and 900 μL of liquid medium. For the samples, the same quantities of the blank was used with additional 10 μL of the sample to be studied. Then, it is left to grow in the shaker at 37 $^\circ C$, 150 rpm for 9 h. The measurements were taken every 30 minutes and measured in the Nanodrop spectrophotometer.

Optical density is calculated using the equation 3.2, where l is the sample thickness consider 1, I_0 is the initial absorbance value, and I is the final absorbance.

4.4   Characterization Equipment

4.4.1   Scanning Electron Microscopy(SEM)

SEM micrographs were taken with a Scanning Electron Microscopy Hitachi SU8030 belonging to the Freie Universitat Berlin (FU), Germany. Samples were prepared in a silicon substrate with a pure drop of each AgTNPs/GO sample. A photo of the equipment is shown in Figure 4.5

Figure 4.5: Scanning electron microscopy Hitachi SU8030 belonging to the Freie Universitat Berlin (FU), Germany.

4.4.2   Transmission Electron Microscopy(TEM)

A Transmission Electron Microscope FEI Tecnai G^2 was used to obtain micrographs of blue 440 nm and green 540 nm irradiation wavelengths for AgTNPs/GO samples. Samples solutions were diluted 100 μL in 1000 μL of distilled water and then sonicated at maximum frequency. A photo of the equipment is shown in Figure 4.6
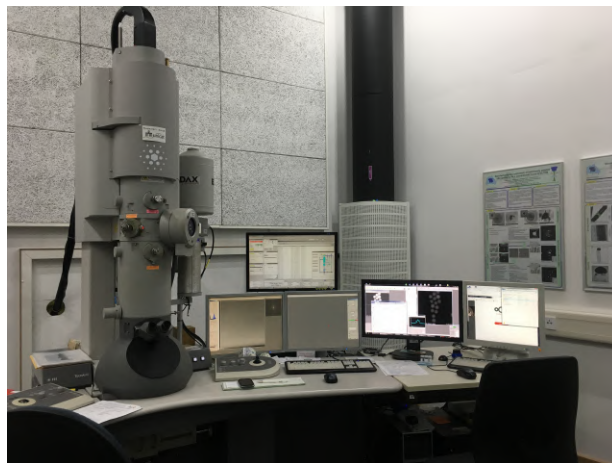
Figure 4.6: Transmission Electron Microscope FEI Tecnai G^2 belonging to the Technique University Berlin, Germany. This characterization was financed by the Free University of Berlin.

4.4.3   Raman Spectroscopy

For this analysis a Raman XPLORA spectrometer with microscopy was used to do the measurements. The samples were excited with a 638 nm wavelength red laser. Samples used for measurements were AgTNPs/GO nanocomposites irradiated with blue 440 nm, green 540 nm, red 650 nm, and white 200-700 wavelengths. The preparation samples was the same as for SEM. A photo of the equipment is shown in Fig. 4.7

4.4.4   UV–Vis Spectroscopy (UV–Vis)

UV-Vis characterization was carried out by Evolution Array UV-Visible Spectrophotometer by Thermo Fisher Scientific belonging to the Freie Universitat Berlin. A full spectra data acquisition is obtained from 200 nm to 1200 nm range. The samples were diluted 400 μL in 1000 μL of distilled water in order to avoid saturation. A photo of the equipment is shown in Figure 4.8

Figure 4.7: Raman XPLORA equipment belonging to the Freie Universitat Berlin (FU), Germany.

Figure 4.8: UV-visible spectrophotometer by Thermo Fisher Scientific equipment belonging to the Freie Universitat Berlin (FU), Germany.

4.4.5 Photoluminescence (PL)

The standard NanoLog Spectrofluorometer comes equipped with a double-grating monochromator in the excitation position. Double-grating monochromators offer a significant increase in sensitivity, resolution and stray-light rejection over single-grating ones. In the excitation position, the NanoLog is equipped with a single-grating iHR spectrometer. Samples preparation was the same used for UV-Vis, and were excited at 332 nm. A photo of the equipment is shown in Figure 4.9

Figure 4.9: Spectrofluorometer HORIBA Nanolog belonging to the Freie Universitat Berlin (FU), Germany.

4.4.6 Optical Density (OD)

Growth bacteria kinetics was followed by measure the absorbance at 600 nm. A Nanodrop 2000 Thermo Scientific Spectrophotometer is used to do the measurements. Figure 4.10 shows a picture of the equipment.

Figure 4.10: Nanodrop 2000 Thermo Scientific Spectrophotometer equipment used to measure the optic density for cell cultures, belonging to the YachayTech University, Ecuador.

Chapter 5

Results & Discussion

5.1 Synthesis and Photochemical Reduction Mechanism

A typical wet chemical method was followed for the synthesis of silver nanoparticles. In an aqueous medium as water(a), the silver source $AgNO_3$ is added (b) in the form of ions to be further reduced. Then, trisodium citrate (TSC) is incorporated (c) as a weak reducer and as a stabilizer[11]. Next, a small amount of 4 μmL of the strong reducing agent as sodium borohydride is affixing (d) to reduce silver ions to form metal nanoparticles fulfilling the nucleation step. Change color in the solution occurs, from noncolor to yellowish (d), confirming the formation of silver nanoparticles. After, hydrogen peroxide is added (e) as an oxidative etching agent to induce the formation of planar-twinned and quasi-spherical structures, and also to remove possible non twinned particles relatively unstable at this stage[19]. Since hydrogen peroxide is an etching agent, it will produce defects as stacking faults or planar twin breaking the isotropic symmetry of silver nanoparticle (fcc)[19]. Therefore, the defects are responsible of anisotropic structures and the final morphology of the nanoparticle[19]. Plate structures are more often observed on silver and gold metals due to their lowest stacking fault energies[19]. Figure 5.1 shows a scheme of the methodology followed to obtain AgNPs/GO.
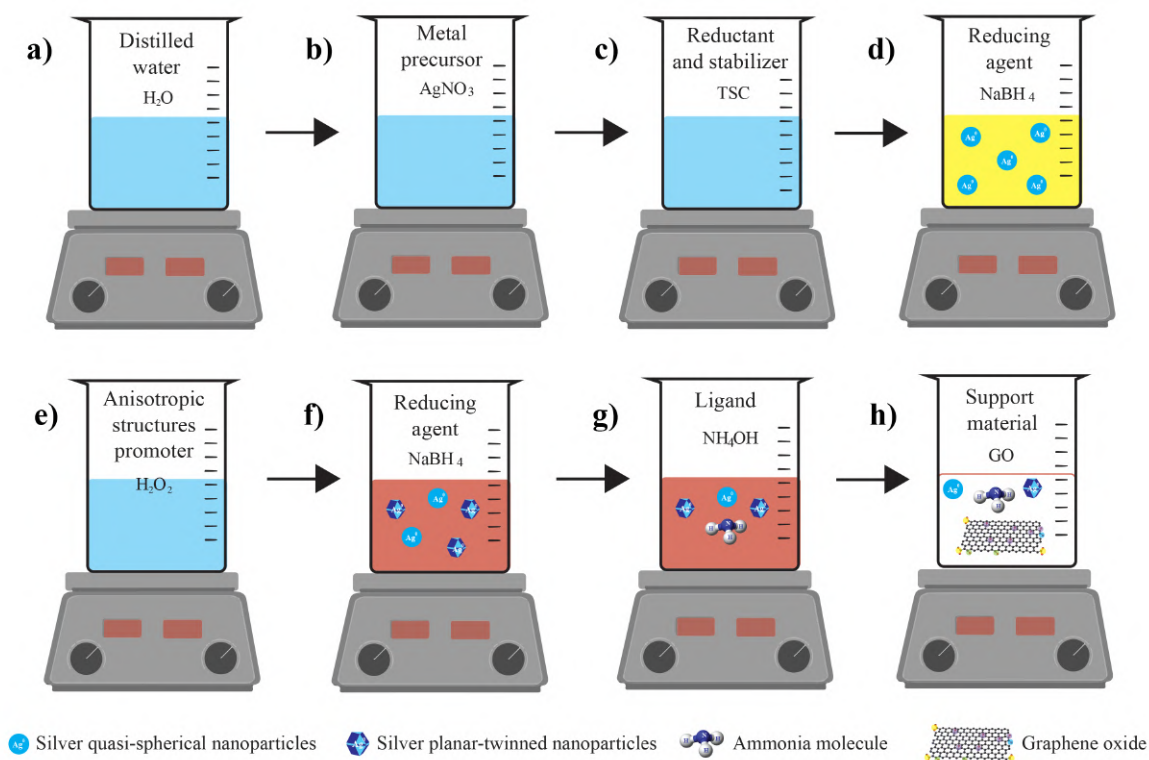
Figure 5.1: Scheme of the methodology described to obtain silver nanoparticles AgNPs/GO initial nanocomposite.

The etching promotes defects as stacking faults, which are responsible for the formation of plate structures[107].
The solution becomes colorless again (e). Then, a higher amount of sodium borohydride (250 μmL) is incorporated
(f) to achieve a complete reduction, the color of the solution undergoes some changes, from yellowish (nanoparti-
cles) to grayish yellow (aggregation), ending in reddish yellow (f) (quasi-spherical and planar twinned). Only small
nanoparticles as $\sim$ 5-8 nm can be photoconverted due to their lower redox potential[19]; in this project, the silver
nanoparticles are around 8 nm, and it ends capping by TSC molecules giving the nanoparticle a negative charge[45].
Next, ammonium hydroxide is incorporated as ligand (g) to combine negatively charged silver nanoparticles with
the negatively charged graphene oxide[41]. Finally, graphene oxide dispersed is added as a support material for the
dispersion of silver nanoparticles (h), this is referred as initial AgNPs/GO solution.

Initial AgNPs/GO suspension, was irradiated with different wavelengths to photoconvert the silver nanoparticles
into triangular nanoplates. Figure 5.2 (a) shows silver nanoparticles as planar twinned structures containing (100)
and (111) facets.
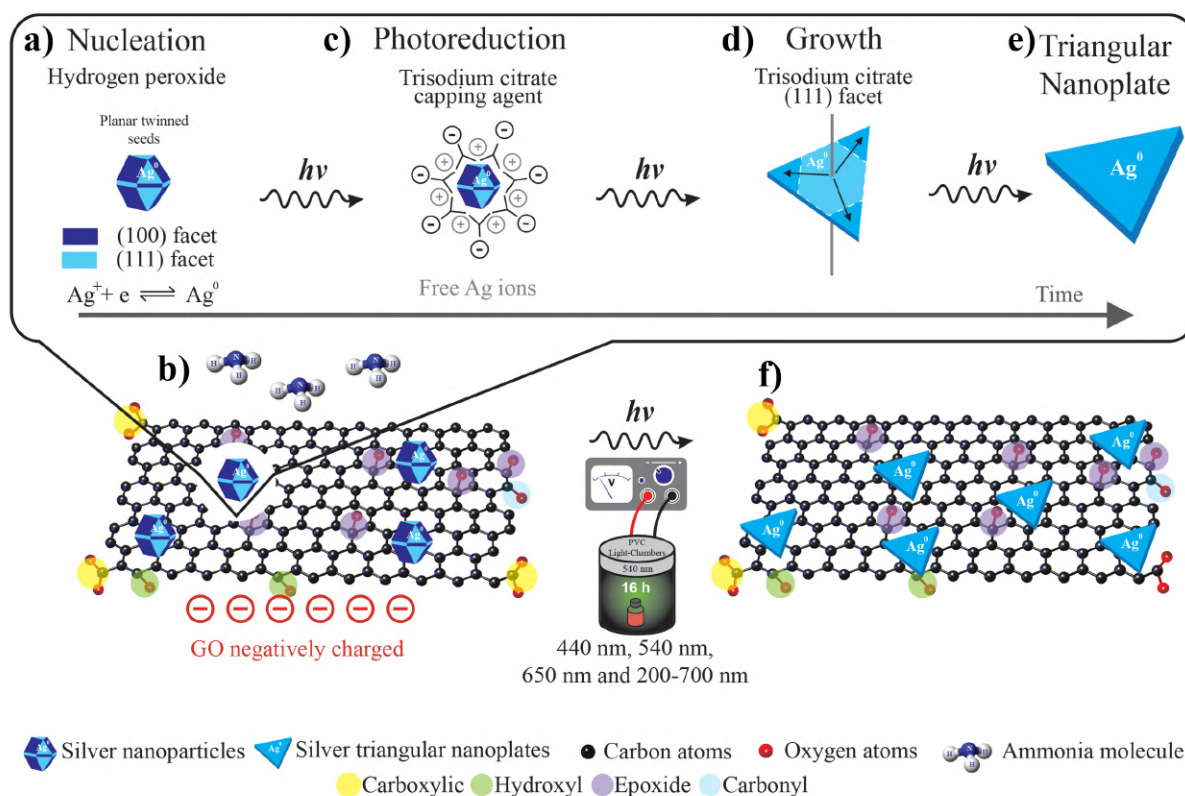
Figure 5.2: Illustration of the photoconversion mechanism from spherical to triangular nanoplates over graphene oxide through *in-situ* method, adapted from Saade & Araujo[11] and Zhang Y. *et al.*[19].

Then, the next step was the deposition of silver nanoparticles on the graphene oxide, through electrostatic attractions and physical adsorption, by the ligand Ammonium hydroxide hydroxide (b). Ammonium hydroxide plays an essential role in binding the negatively charged nanoparticles to the negatively charged graphene oxide as well. After this, the photochemical reduction method starts, the irradiation wavelength coming from the high power LED, gives the necessary energy[19] to reduce the remaining ions after the chemical synthesis. Step (c) shows the ions attached to the silver nanoparticles by electrostatic attraction as well as trisodium citrate (TSC). TSC has three carboxylic groups, and at least two of them selectively bind to (111) facets; the third group is oriented normal to the surface[11]. This component acts as a stabilizer, reducing, and capping agent for silver nanoparticles[11]. It works under the face-block theory, which states that the TSC will block the growth in the vertical axis and allows a rapid growth at the lateral direction[19]. Figure 5.2 (d) reveals the growth of nanoparticle in the (111) facet to produce silver triangular nanoplates (AgTNPs), finally (e). The nanoparticles are converted to triangular nanoplates (e) in the presence of GO by the photochemical reduction method (f).

Photoconversion or photo-light induced processes are based on the absorption of photons coming from the light, then the conduction electrons at the surface of the silver nanoparticle start to oscillate with respect to their nucleus [108]. Then, a redox reaction take place: electron flow allows the TSC to reduce silver ions from Ag^+ into Ag^0 allowing the nanoparticle growth, while holes are hot sites that oxidize citrate ions adsorbed on the particle surface [108]. The oscillation of electrons at the nanoparticle surface is defined as a surface plasmon [109], and when they oscillate with the same frequency than the irradiation light it is known as surface plasmon resonance [14]. The resonance between irradiation light and nanoparticle is dependent on the light frequency (wavelength) and nanoparticle size [108]. Specific sizes of nanoparticles are needed for each irradiation wavelength to enter into resonance, thus until the resonance is achieved, the nanoparticle is growing slowly which is beneficial for anisotropic shapes [109]. Then, when they enters into resonance, a fast growth of nanoparticle happens [109]. Finally, the wavelength irradiation dependence follows: increasing the wavelength increases the size and anisotropy of the final nanoparticle [108].

5.2   Characterization of Ag TNPs/GO

5.2.1   Scanning Electron Microscopy (SEM)

Scanning Electron Microscopy (SEM) technique was used to determine the graphene oxide flakes (GO flakes) sizes in terms of length, to confirm the deposition of silver nanoparticles (AgNPs) on GO, and to make an analysis of the AgNPs distribution size. The size of GO flakes was measured in ImageJ software tracing a diameter, as well as for the silver nanoparticles (AgNPs). Brightness contrast is given by the elements present and its different atomic number-the heavier the element, the brighter it will show up on the micrograph. Therefore, silver nanoparticles will exhibit more brilliance than graphene oxide. For brilliance parts of GO flakes an effect of overload may be present [73]. This is due to the distribution of the electron beam in the sample, promoting more elastic dispersion and therefore more backscattered electrons which are responsible of brightness [73].

Figure 5.3 shows the micrographs of blue 440 nm irradiation wavelength for AgTNPs/GO nanocomposite.
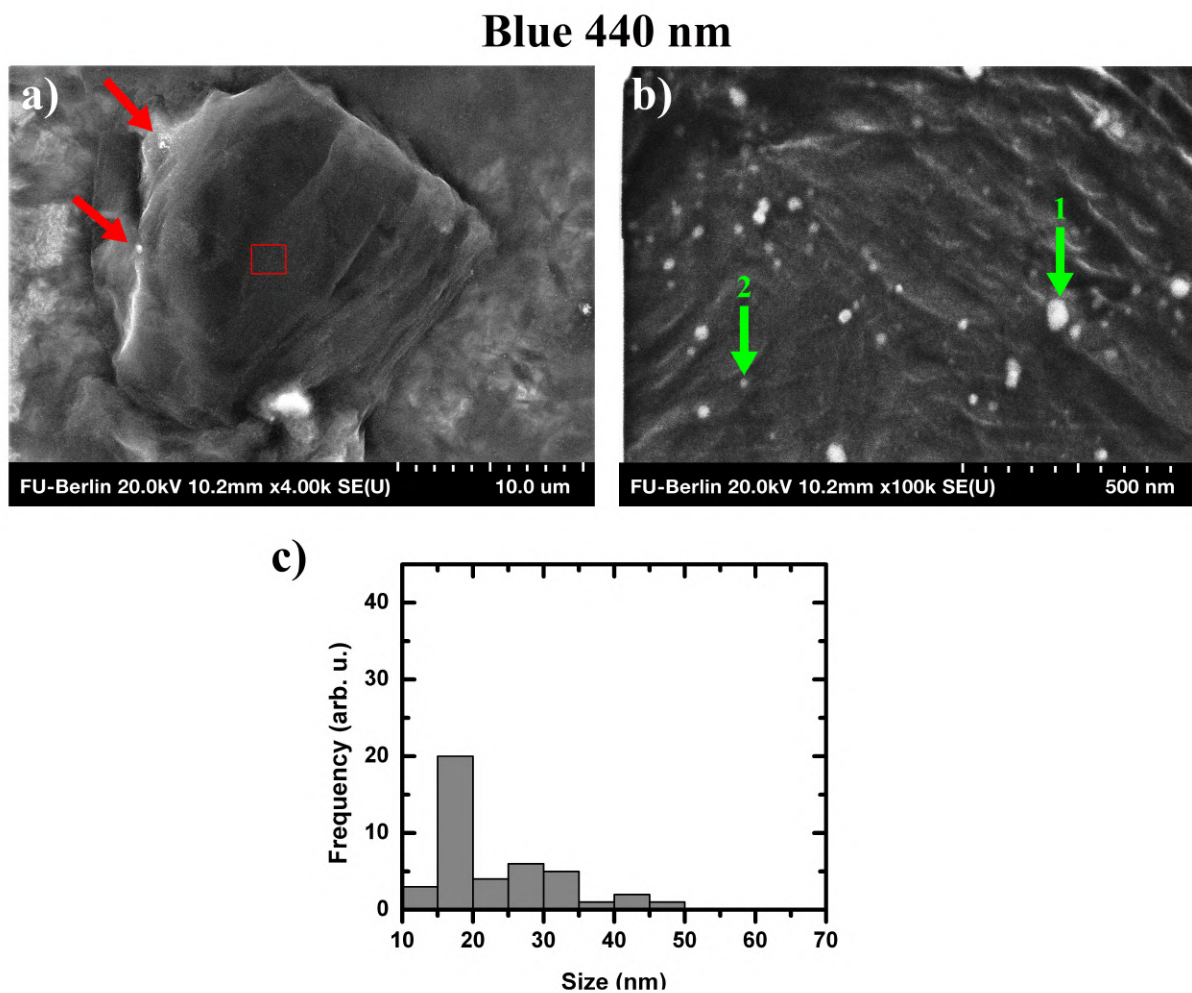
Figure 5.3: SEM micrographs of blue 440 nm irradiation wavelength for AgTNPs/GO nanocomposite in a) 10 μm and b) 500 nm scales.

Figure 5.3 (a) presents a SEM micrograph of a 20 μm GO flake. GO flake has low contrast due to the low atomic number of carbon atoms[73]. While silver nanoparticles appears as white dots, having higher contrast than GO since they have high atomic number[73]. The red arrows indicate the most representative sites of nanoparticles deposition. The red square shows the inset for the (b) micrograph. The nanoparticle deposition is due to GO functional groups located at the surface and edges of the flake[28]. Fig. 5.3 (b) micrograph reveals AgNPs deposited on GO. Fig. 5.3 (c) shows a histogram of nanoparticle sizes presented in (b). The total nanoparticles in (b) micrograph is 42, and the

47.6% are of 20 nm in size, being the highest bar in the histogram indicating a monomodal size distribution[110].

Figure 5.4 shows the micrographs of green 540 nm irradiation wavelength for AgTNPs/GO nanocomposite.
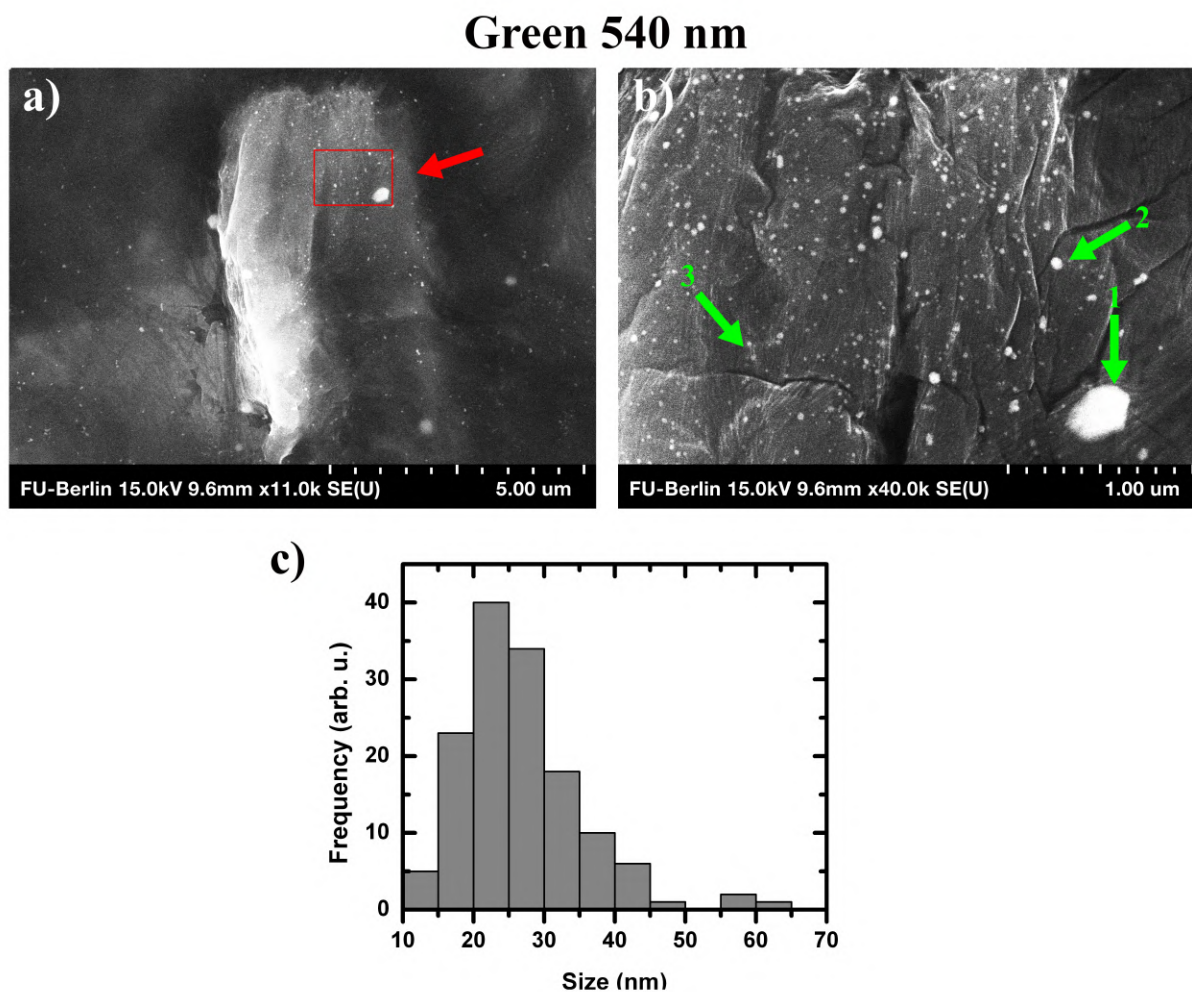
Figure 5.4: SEM micrographs of green 540 nm irradiation wavelength for AgTNPs/GO nanocomposite in (a) 5 μm and (b) 1 μm scales.

Figure 5.4 (a) shows a GO flake with a size of 7 μm. The micrograph shows the presence of nanoparticles on the GO surface. The red arrows points to a big brightness spot, attributed to an agglomeration of silver nanoparticles. The red square shows the inset for the (b) micrograph. Fig. 5.4 (b) reveals AgNPs deposited on graphene oxide. The first green arrow points to the agglomeration of AgNPs due to the big size around of 300 nm, and it is considered

agglomeration because the other nanoparticles are smaller in size. The second green arrow shows the biggest nanoparticles with a size of 40 nm, while the third arrow shows the smallest one with 5 nm of size. Fig. 5.4 (c) reveals the histogram of nanoparticles observed in (b). The total number of nanoparticles counted in the (b) micrograph is approximately 140. The 28.6% corresponds to 20-25 nm nanoparticle sizes, and the 24.3% represents nanoparticles around 25-30 nm, which are the majority in the histogram. The nanoparticle sizes are around 30 nm which indicates a monomodal size distribution[110].

Figure 5.5 shows the micrographs of red 650 nm irradiation wavelength for AgTNPs/GO nanocomposite.
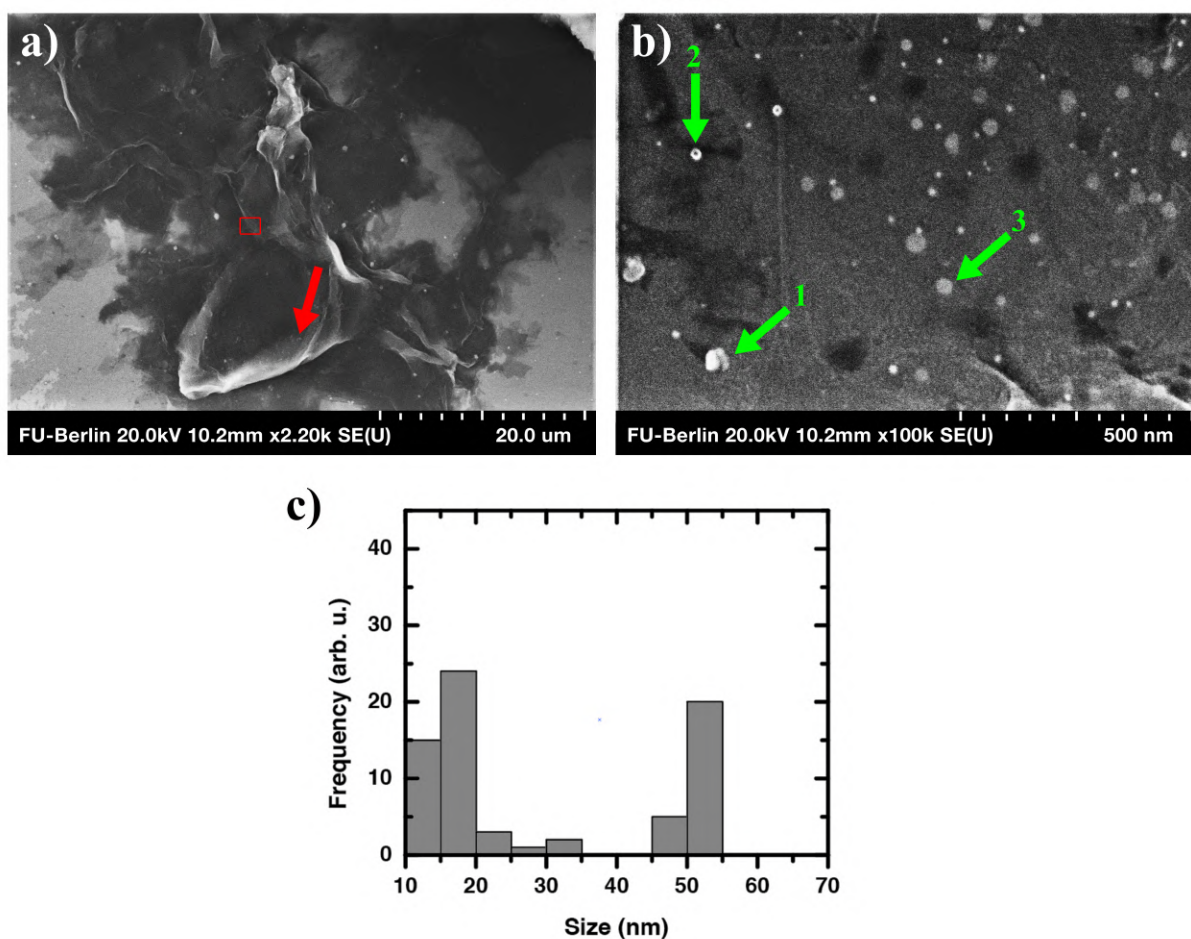
Figure 5.5: SEM micrographs of red 650 nm irradiation wavelength for AgTNPs/GO nanocomposite in (a) 20.0 μm and (b) 500 nm scales.

Figure 5.5 (a) presents a GO flake of size 30 μm. The red arrow points to AgNPs deposited on the flake. The red square represents the inset for (b) micrograph. Fig. 5.5 (b) also displays nanoparticles deposited on the surface of the GO flake. The first and second green arrows point to agglomerations of nanoparticles due to its brigthness and size. The third arrows point to spherical silver nanoparticle with a size around 50 nm. Fig. 5.5 (c) shows the histograma of the AgNPs seen in (b). The total nanoparticles counted is 70, and the 34% have sizes of 15nm, while the 29% corresponds to sizes around 50 nm. This shows a bimodal size distribution, which means a polydispersed system[111].

Figure 5.6 shows the micrographs of white 200-700 nm irradiation wavelength for AgTNPs/GO nanocomposite.
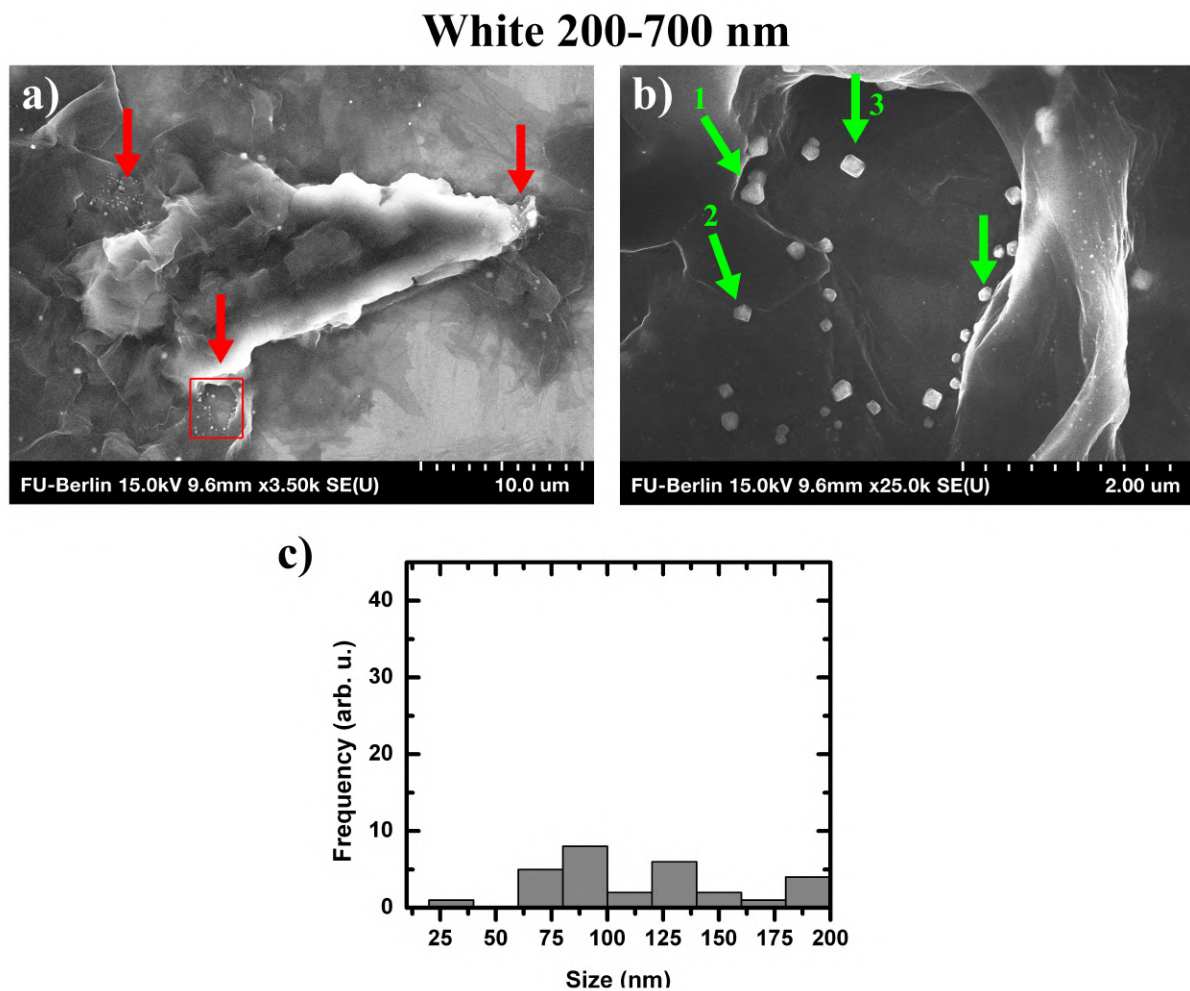
White 200-700 nm

Figure 5.6: SEM micrographs of white 200-700 nm irradiation wavelength for AgTNPs/GO nanocomposite in (a) 10 μm and (b) 2 μm scales.

Figure 5.6 (a) presents a GO flake of size 28 μm. GO flake presents the overload effect mentioned before[73]. The red arrows indicate the sites where the AgNPs are deposited due to its big sizes. The red square is the inset for (b) part. Fig. 5.6 (b) micrograph reveals AgNPs deposited on graphene oxide. The green arrows indicates nanoparticles with polyhedrons shapes, which comes from the pathways of silver nanoparticle growth during the photoreduction process[11,13]. The first green arrow indicates a pentagonal shaped nanoparticle, the second arrow shows a triangular truncated nanoparticle, and the third arrow points to a cubic silver nanoparticle. Fig. 5.6 (c) presents an histogram for

nanoparticles observed in (b). The total counted nanoparticles is 29, and the 27.6% of them have size around 75-100 nm. Since several sizes are observed, the system is polydispersed, and shows a multiple modal size distribution[111].

For all the samples, the part (b) was taken to make the histograms. For blue 440 nm sample, 42 nanoparticles were present, while for green 540 nm 140 were counted. For red 650 nm nanocomposite 70 nanoparticles are shown, while for white 200-700 nm sample, 29 nanoparticles were found. Therefore, the highest concentration is attributed to green 540 nm nanocomposite. In the other hand, biggest nanoparticles corresponds to white 200-700 nm sample, while the shortest corresponds to blue 440 nm; this due to - increasing the irradiation wavelength increase the size of nanoparticles[108].

The deposition of silver nanoparticles on graphene oxide depends of the physical adsorption. Physical adsorption is based on electrostatic forces[12], which vary according to the partial charge of the nanomaterials involved. In this case, the grown nanoparticles end up with a TSC capping, which gives a negative partial charge, and the presence of oxygen functionalities negatively charged the graphene oxide, then the Ammonium hydroxide , positively charged, allows the join of these nanomaterials. If the nanoparticle did not grow, it would not be completely surrounded by TSC, and its partial charge will be lower than the others with the larger size. This is why the blue sample does not show a high concentration of nanoparticles. Big nanoparticles can end with a higher negative charge, and the electrostatic attractions balanced can not works well.

5.2.2 Transmission Electron Microscopy (TEM)

TEM characterization was done in order to study the size distribution and morphology of silver nanoparticles deposited on the GO surface. Representative micrographs and size distribution histogram are shown in this section. For the performance of histogram complementary TEM micrographs were used, and they are exhibited in section Appendix A A.1 Fig. and Fig.A.2. For the size measurement, the Image J software was used, the diameter was measured for spherical nanoparticles, and the height for triangular shapes. Figure 5.7 shows representative micrographs for blue 440 nm AgTNPs/GO nanocomposite irradiation wavelength.
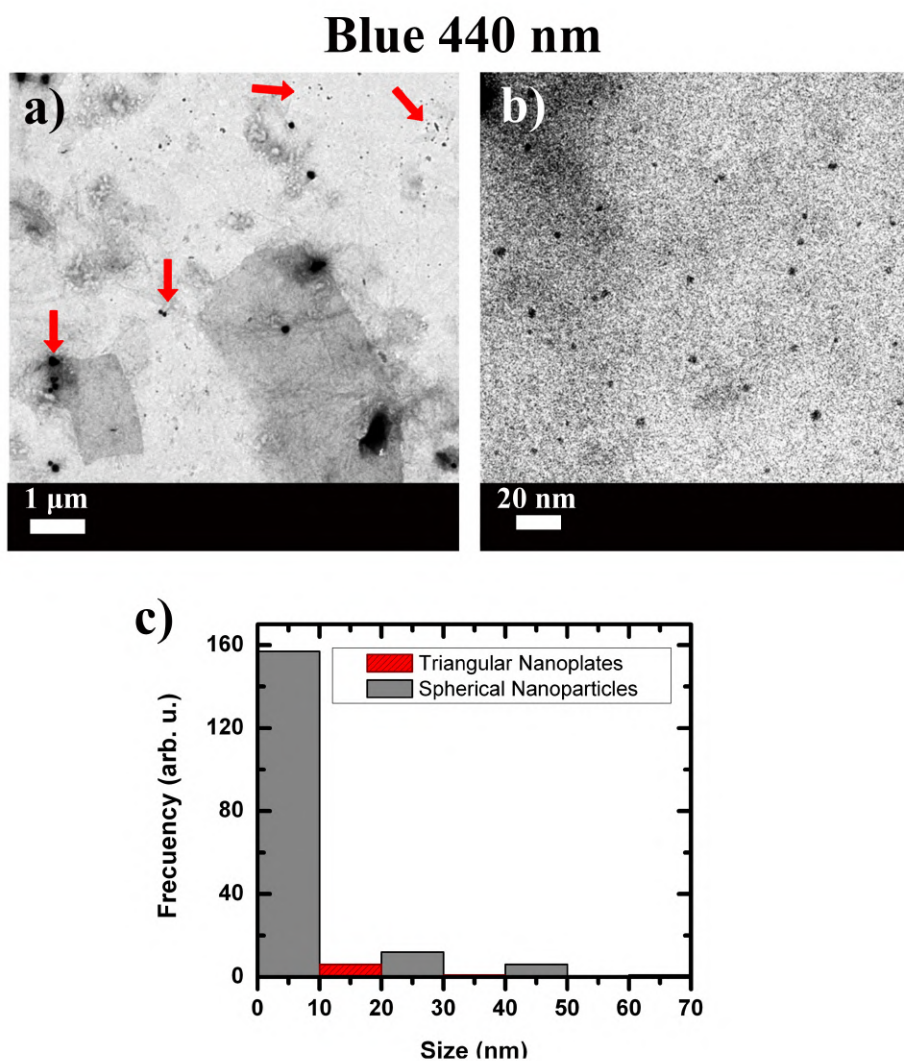
Figure 5.7: TEM micrographs of blue 440 nm irradiation wavelength for AgTNPs/GO nanocomposite (a) 1 μm^2 and (b) 20 nm scales, (c) Histogram of silver spherical nanoparticles and silver triangular nanoplates.

Figure 5.7 (a) shows AgNPs deposited on GO flake. Fig. 5.7 (b) presents very small spherical nanoparticles that can be quasi-spherical or planar twinned, with their size ranged of 5 nm. Also, they can be silver clusters formed by the photochemical reduction reaction of free silver ions[108]. Fig. 5.7 (c) presents an histogram which reveals that most of the nanoparticles found are spherical and around of 10 nm size indicating a monomodal size distribution[110]. The size is in agreement with the irradiation wavelength dependence[108], since 440 nm is the shorter one in this project, and with respect to anisotropy, slower processes with longer wavelengths are preferred[108].

Figure 5.8 for green 540 nm irradiation wavelength for AgTNPs nanocomposite.
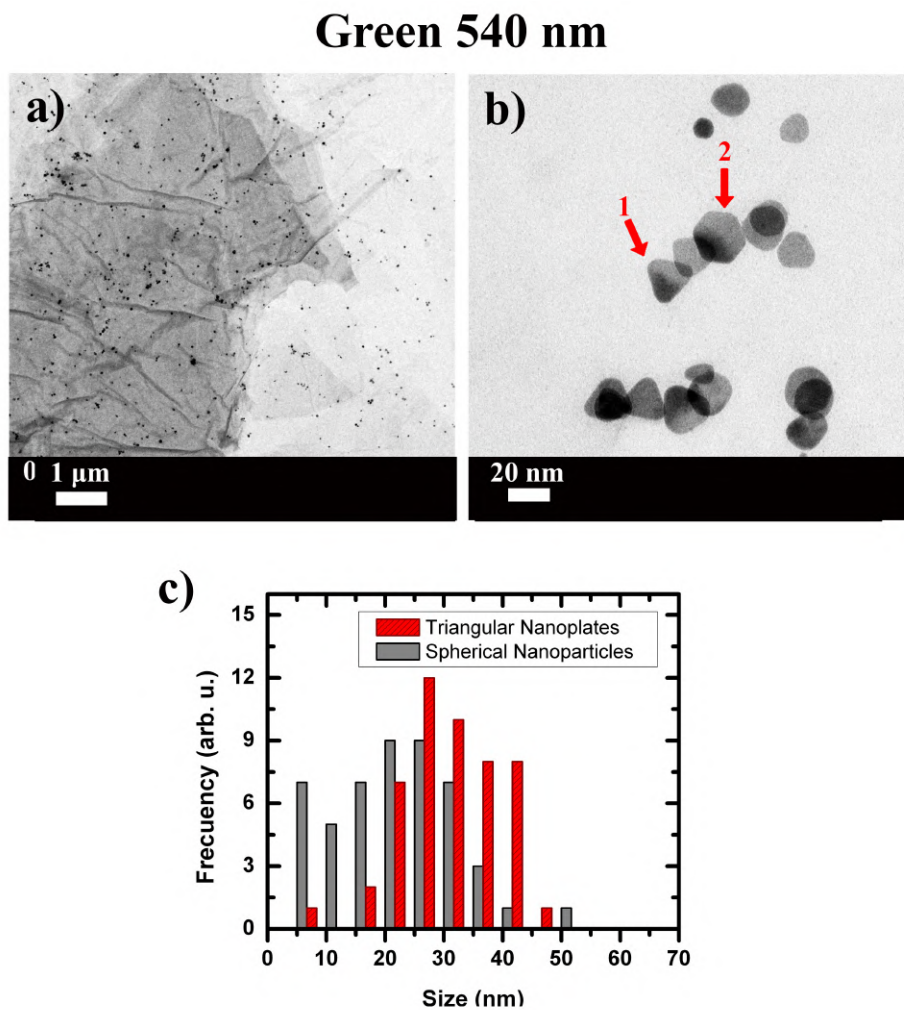
Green 540 nm

Figure 5.8: Bright-field TEM micrographs of green 540 nm irradiation wavelength for AgTNPs/GO nanocomposite (a) 1 μm and (b) 20 nm scales, (c) shows the size distribution histogram of silver spherical nanoparticles and silver triangular nanoplates.

Figure 5.8 (a) reveals AgNPs deposited on GO flake. Fig. 5.8(b) nanoparticles of different shapes can be observed where the triangular one predominates. The red arrows are examples of different anisotropic shapes. The first arrow points to a triangular shaped nanoparticle with a size of approximately 30 nm, while the second arrow indicates a hexagonal shaped nanoparticle with similar size than triangular nanoparticle. These shapes comes from the growth pathways for twinned silver nanoparticles occurring in the photoreduction process[13]. Fig.5.8 (c) shows

the size distribution histogram determining that most of the nanoparticles found are silver triangular nanoplates converted by the *in-situ* method proposed, with a size around of 30 nm showing a monomodal size distribution[111]. Rounded tips are present due to the presence of TSC molecules in excess, it can promote a low growth even without the irradiation process[19]. The deposition of nanoparticles can be attributed to the statement of Goncalves *et al.*[24] which says that GO oxygen functionalities are reactive sites for the nucleation and growth of metal nanoparticles and, also allows the formation of strong bonds with the material being deposited. Thus, we can assume that the *in-situ* photoreduction method can promote the deposition and growth of silver triangular nanoplates as shown in TEM micrographs of green 540 nm sample and histogram, Fig. 5.8. Besides, these data reveals that, between these two irradiation wavelengths, the most efficient for the photoconversion of the silver nanoparticles is the green 540 nm. This is due to the-increasing the wavelength of irradiation increases the anisotropy of the final nanoparticle[108].

5.2.3 Raman Spectroscopy

Raman spectroscopy reveals information about the structural features of graphene oxide (GO)[112]. The D band is attributed to the defects of the GO structure, while the G band corresponds to the bond stretching of carbon sp^2 atoms[85]. To characterize the disorder of the graphitic structure in carbon materials[28], the D and G band intensities ratio I_D/I_G are calculated. A center point from the full width at half maximum FWHM of the D and G bands was taken to obtain the position of the D and G band, as well as the respective intensity. The dashed lines shown in Fig.5.9 represent the way to obtain the intensity. Figure 5.9 exhibits the Raman spectra of AgTNPs/GO nanocomposites irradiated with different wavelengths.
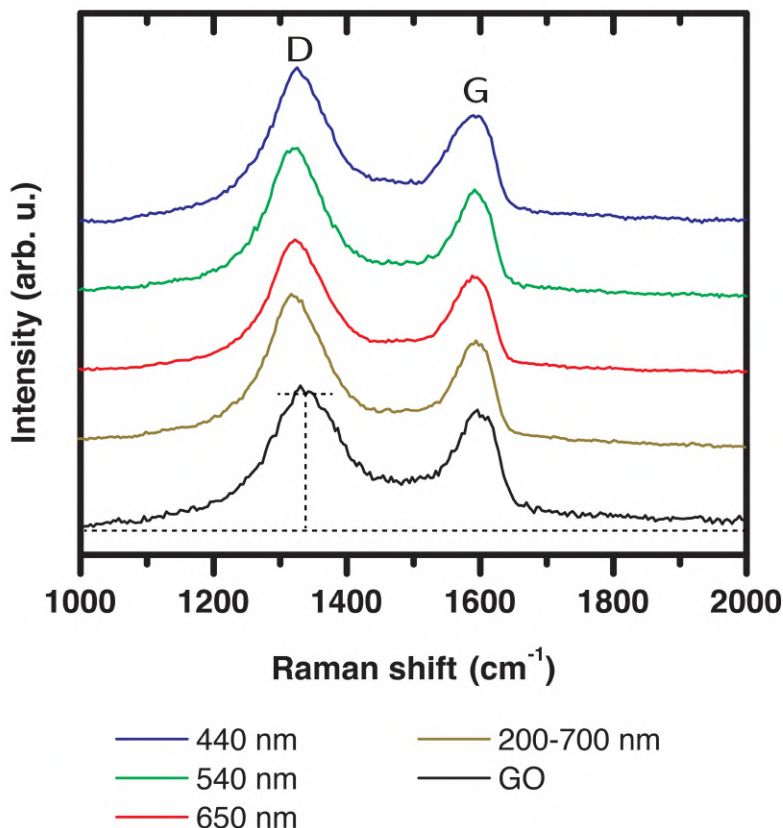
Figure 5.9: Raman spectra of AgTNPs/GO nanocomposites irradiated with blue 440 nm, green 540 nm, red 650 nm and white 200-700 nm wavelengths.

As can be seen in Fig. 5.9 GO has a highly disordered structure due to presence of functional groups in the structure, as result of the graphite powder oxidation[28]. The position of the D band is 1340 cm^{-1} and the G band 1600 cm^{-1}; the I_D/I_G ratio is 1.14 which is in agreement with Zhang et. al[43]. For the samples, the I_D/I_G ratio was calculated in order to compare the structural disorder caused by triangular nanoplates deposition. The presence of nanoparticles in the structure of graphene oxide can cause defects increasing the intensity of the D band. In addition, depending on the size of the nanoparticles, they will cause greater tensile stress on the bonds between the carbon atoms by increasing the G band intensity. Therefore, the increase in the I_D/I_G ratio means that the nanoparticles were effectively adsorbed onto both sides of the graphene oxide flakes, surface and edges[113]. It is corroborated with SEM characterization: Fig. 5.3, Fig. 5.4, Fig. 5.5, and Fig. 5.6.

For the Raman spectra of AgTNPs/GO nanocomposites irradiated with different wavelengths, the I_D/I_G ratio has an increased value which indicates the presence of nanoparticles in the structure of the GO[93]. The variation in

the intensity ratios is attributed to the amount of nanoparticles present in the GO flake and the size of these particles for each sample, which was discussed in the SEM characterization section. The shift to smaller wavenumber of nanocomposite D bands with respect to GO. Table 5.1 shows the D and G bands positions of graphene oxide and AgTNPs/GO nanocomposites iradiated with different wavelengths. The shift found of D band position between graphene oxide and nanocomposites is also revealed.

Sample	D (cm^{-1})	G (cm^{-1})	D Shift (cm^{-1})	I_D/I_G
Graphene Oxide	1340	1600	–	1.14
Blue 440 nm AgTNPs/GO	1330	1595	10	1.32
Green 540 nm AgTNPs/GO	1320	1595	20	1.37
Red 650 nm AgTNPs/GO	1320	1595	20	1.33
White 200-700 nm AgTNPs/GO	1320	1595	20	1.35

Table 5.1: D and G bands positions shifts between the graphene oxide and AgTNPs/GO nanocomposites irradiated with different wavelengths.

For blue 440 nm AgTNPs/GO the shift is 10 cm^{-1}, while for green 540 nm nanocomposite is 20 cm^{-1} as well as for red 650 nm and white 200-700 nm nanocomposites. All the AgTNPs/GO nanocomposites present a shift to smaller wavenumber, it is related to the oxygen content in the graphene oxide[114]. According to Claramunt S. *et al.*[114] the shift to lower wavenumbers of the contribution peaks observed in the fitting proposed, indicates a decrease in the oxygen content. Besides, a decrease in the oxygen content is recognized as a restoration of C-C/C=C bond process[115]. Another reports[116] use this photoreduction process to obtain reduced graphene from GO, decreasing its oxygen content by irradiating with visible light. G band does not shows significant shifts. With respect to nanocomposites I_D/I_G ratio, the lowest corresponds to the red 650 nm nanocomposite due to its low concentration of nanoparticles. While the highest ratio is attributed to green 540 nm nanocomposite owing to it has the highest concentration of nanoparticles, as we saw in Fig. 5.3 and Fig. 5.7. A high concentration of nanoparticles can produced greater amount of defects in the GO structure, and tensile strain in the stretching of carbon atoms[116].

5.2.4   Ultraviolet–Visible Spectroscopy (UV–Vis)

UV-Vis spectroscopy was used to study the optical properties and characteristic absorption bands for AgTNPs and AgTNPs/GO nanocomposite in aqueous medium. All irradiated samples ended with a different solution color than the initial red. The colors obtained of the final solutions of AgTNPs are shown in Figure 5.10.
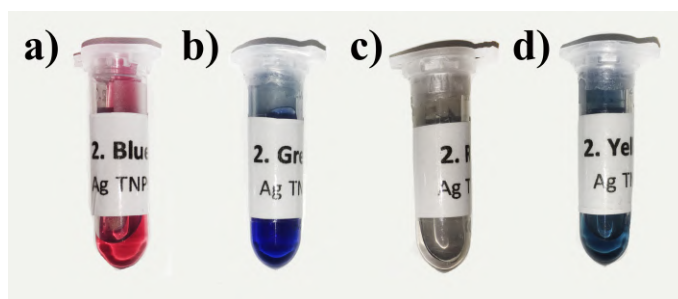
Figure 5.10: Final color solutions of silver triangular nanoplates AgtNPs irriadated with green at 540 nm (a), blue at 440 nm (b), red at 650 nm (d), and white at 200-700 nm (d).

Different colors are obtained for silver triangular nanoplates after the photoreduction process. These optical properties are related to the size and shape of nanoparticles. Different resonance modes are expected in UV-Vis spectra. Fig. 5.10 (a) exhibits a red color when silver nanoparticles suspension is irradiated at 440 nm blue LEDs, (b) shows a blue color with 540 nm green LED irradiation wavelength. Fig. 5.10 (c) reveals a gray color with 650 nm green LED wavelength, while (d) presents a light blue color with 200-700 nm white irradiation wavelength.

The colors obtained of the AgTNPs/GO nanocomposite final solutions are shown in Figure 5.11.
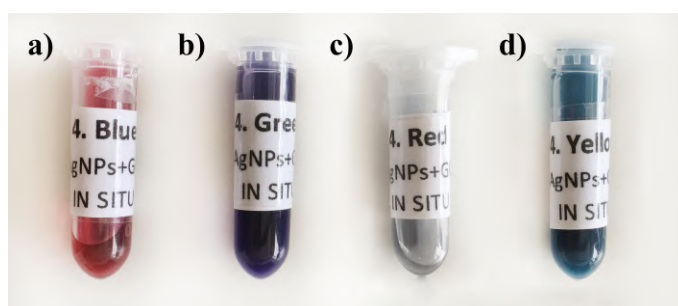
Figure 5.11: Final color solutions of *In-situ* method irriadated with blue at 440 nm a), green at 540 nm b), white at 200-700 nm c) and red at 650 nm d).

Similar colours can be seen for the nanocomposite as for silver triangular nanoplates. Fig. 5.11 (a) shows the same red color as AgTNPs, while (b) exhibits a darkner blue that can be attributed to GO flakes or AgTNPs agglomerations. Fig. 5.11 (c) shows a similar gray color, and (d) reveals a light blue color similar to the AgTNPs. The different colors obtained means different size and shapes, so we can conclude that the photoreduction method influence in the nanocomposite.

Figure5.12 shows the UV-Vis spectra of graphene oxide pristine (GO Pristine) (a) and silver nanoparticles (AgNPs) (b). Fig.5.12 (a) shows two main peaks of graphene oxide, the first peak at about 278 nm which corresponds to $\pi - \pi^*$ transitions of aromatic $C - C$ bonds, while the second peak at about 376 nm is attributed to $n - \pi^*$ transitions

of $C - O$ bonds[44]. Both are shifted to higher wavelengths due to the different elemental composition of the graphene oxide[105].
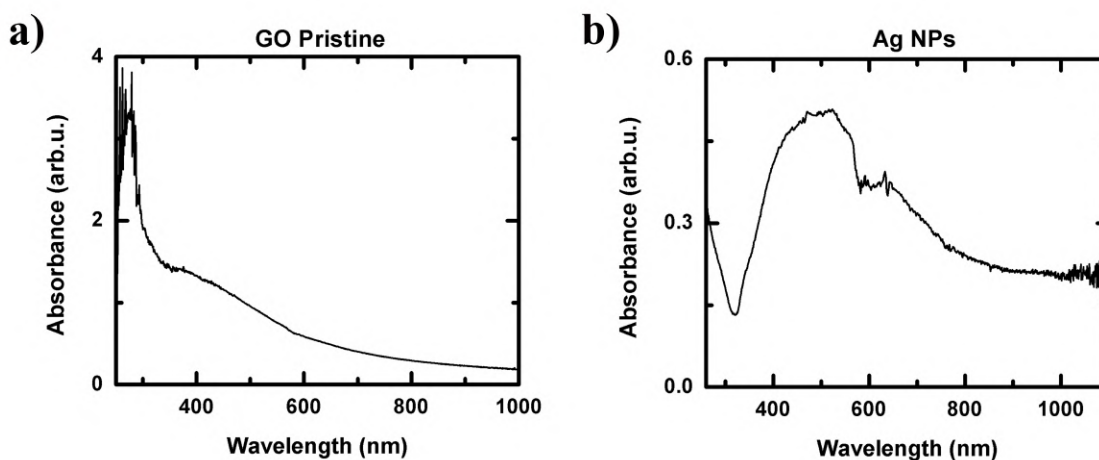
Figure 5.12: UV-Vis spectra of graphene oxide pristine (GO Pristine) (a) and silver nanoparticles (AgNPs) (b).

Figure 5.12 (b) exhibits a characteristic peak around 490 nm for silver nanoparticles and a shoulder at 650 nm, suggesting a polydisperse system[11]. Since an etching agent and flat structures promoter[19] were used for the wet chemical synthesis and, specifically for the nucleation step, the silver nanoparticles can shows planar structures that could be associated to the presence of two surface plasmon resonances (SPR). Table 5.2 indicates the absorption bands positions and its meaning for these samples.

Sample	Peak	Position[nm]	Assignment
Graphene oxide pristine (GO pristine)			
	1	278	$\pi - \pi^*$ transitions of aromatic $C - C$ bonds[44].
	2	376	$n - \pi^*$ transitions of $C - O$ bond[44].
Silver nanoparticles (Ag-NPs)			
	1	490	Characteristic SPR of silver nanoparticles[44]
	2	640	SPR different nanoparticle sizes[111]

Table 5.2: Table of UV–Vis SPR bands positions of graphene oxide pristine (GO Pristine) and silver nanoparticles (AgNPs) corresponding to Figure 5.12.

GO pristine spectrum has two absorption bandas: the first at 278 nm corresponding to $\pi - \pi^*$ transitions of aromatic $C - C$ bonds[44], the second peak is at 376 and it is attributed to $n - \pi^*$ transitions of $C - O$ bond[44]. For AgNPs the spectra shows two peaks: the first at 490 nm related to a characteristic absorption band of silver nanoparticles[44], the second at 640 nm ascribed to different nanoparticle sizes[111], that is a bimodal size distribution[29].

Figure 5.13 presents the UV-Vis spectra of silver triangular nanoplates (AgTNPs) (a) and silver triangular nanoplates deposited on graphene oxide (AgTNPs)/GO) nanocomposite by *in-situ* method (b), both irradiated with blue 440 nm, green 540 nm, red 650 nm, and white 200-700 nm wavelengths.
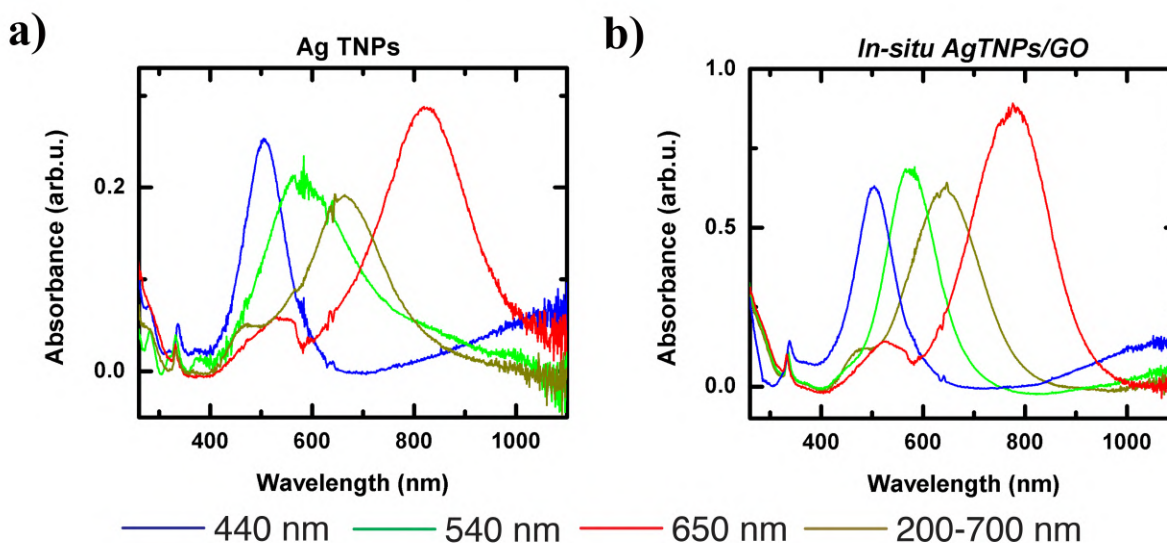
Figure 5.13: UV-Vis spectra of silver triangular nanoplates (AgTNPs) (a) and silver triangular nanoplates deposited on graphene oxide nanocomposite by *in-situ* method (*In-situ* AgTNPs/GO) (b).

Figure 5.13 (a) shows two main peaks for silver triangular nanoplates. According to Saade *et al.*[11], a weak absorption band SPR of silver nanoprisms is localized at 330 nm indicating a characteristic peak for anisotropic nanoparticles shape. This SPR is attributed to the out-of-plane quadrupole resonances[110]. The second SPR, the strong one, corresponds to the wavelength of the primary irradiation source[11], which shows that a longer primary irradiation wavelength produces larger particles[108]. This strong SPR is related to the in-plane dipole resonance and its red-shifted means the growth of nanoparticles (due to irradiation wavelength)[111]. Other weak SPRs are interpreted as in-plane quadrupole resonances, indicating different nanoparticle sizes corresponding to multiple modal size distribution[110]. Table 5.3 shows the absorption bands positions and its meaning for silver triangular nanoplates (AgTNPs) corresponding to Fig. 5.13 (a). In agreement with literature[11], AgTNPs has two main surface plasmon resonance bands.

Silver triangular nanoplates (AgT-NPs)	Peak	Position[nm]	Assignment
Blue 440 nm			
	1	337	Weak SPR characteristic peak of triangular nanoplates[11]coming from out-of-plane quadrupole resonances[110]
	2	505	Characteristic peak of triangular nanoplates depending on the irradiation wavelength used in the photoreduction process[110] and it comes from the in-plane dipole resonance[111]
Green 540 nm			
	1	285	Weak SPR corresponding to flat structures formed in the nucleation and it comes from the in-plane quadrupole resonances[16]
	2	331	Weak SPR characteristic peak of triangular nanoplates[11]coming from out-of-plane quadrupole resonances[110]
	3	380	Weak SPR attributed to different nanoparticle sizes[111], and spherical shape[117]. It comes from in-plane quadrupole resonances[110]
	4	580	Characteristic peak of triangular nanoplates depending on the irradiation wavelength used in the photoreduction process[110] and it comes from the in-plane dipole resonance[111]
Red 650 nm			
	1	334	Weak SPR characteristic peak of triangular nanoplates[11]coming from out-of-plane quadrupole resonances[110]
	2	533	Weak SPR attribute to different nanoparticle sizes[111] and plate-like structures[117]. It comes from in-plane quadrupole resonances[110]
	3	825	Characteristic peak of triangular nanoplates depending on the irradiation wavelength used in the photoreduction process[110] and it comes from the in-plane dipole resonance[111]
White 200-700 nm			
	1	335	Weak SPR characteristic peak of triangular nanoplates[11]coming from out-of-plane quadrupole resonances[110]
	2	450	Weak SPR attributed to different nanoparticle sizes[111], and spherical shape[117]. It comes from in-plane quadrupole resonances[110]
	3	680	Characteristic peak of triangular nanoplates depending on the irradiation wavelength used in the photoreduction process[110] and it comes from the in-plane dipole resonance[111]

Table 5.3: Table of UV–Vis SPR bands positions of silver triangular nanoplates (AgTNPs) SPR bands positions, corresponding to Fig. 5.13 (a)

Blue 440 nm AgTNPs spectra has two SPR: the first SPR is a weak peak located at 337 nm, it is attributed to a characteristic peak of anisotropic structures[11] and it comes from out-of-plane quadrupole resonances[110], and the second SPR is a strong peak located at 505 nm corresponding to characteristic peak of triangular nanoplates due to the irradiation wavelength[110]. Green 540 nm AgTNPs spectra has four SPR: the first weak SPR is located at 285 nm and it is related with flat structures coming from the nucleation. This absorption band is attributed to in-plane quadrupole resonances[16]. The second SPR at 331 nm is a characteristic peak of triangular nanoplates[11] as well as that observed for the blue 440 nm sample. The third peak located at 380 nm represent a weak SPR attributed to different nanoparticle sizes, and spherical shapes[111], it comes from in-plane quadrupole resonances[110]. The fourth SPR located at 580 nm corresponds to the irradiation wavelength used in the photoreduction process[110] and it comes from the in-plane dipole resonance[111].

Red 650 nm AgTNPs spectrum reveals three SPR: the first at 334 nm is a weak SPR characteristic peak of triangular nanoplates[11] also present in the above described samples. The second SPR is located at 533 nm and corresponds to different nanoparticle sizes indicating a bimodal size distribution[111]. Besides, it can be related with faceted nanoparticles which means a preferential facet (side) growth, that in this project produce plate-like structures[117]. The third SPR is at 825 nm and is associated with the irradiation wavelength used in the photoreduction process[110]. Finally, for white 200-700 nm AgTNPs the spectra reveals three peaks: the first peak at 335 nm is a characteristic weak SPR of anisotropic structures[11] and it is present in all the samples, demonstrating that anisotropic and plate-like forms were obtained after photoreduction process. The second peak is located at 450 nm and it is attributed to different nanoparticle sizes, and spherical shapes[111]. The third peak at 680 nm is the one that depends on the irradiation wavelength used in the photoreduction process, and it is directly related to nanoparticle size[110].

The surface plasmon located in the range 330-340 nm is characteristic of anisotropic structures[11]. The presence of SPR absorption bands before this range are attributed to plate-like structures that are formed during nucleation in the chemical synthesis and that have not grown during the photo reduction process. The location of SPR absorption bands after this range depends on the irradiation wavelength used in the photo reduction. For example, for the wavelength 440 nm, the SPR should be located by the same value with a slight shift towards higher wavelengths, this shows the growth of nanoparticles[110]. SPRs between 300 nm and the corresponding irradiation wavelength corresponds to different nanoparticles sizes, if it is located before 500 nm, it is attributed to spherical nanoparticles, while if the SPR is after the 500 nm, it indicates plate-like structures[117].

Among the samples, the red sample has the largest shift towards higher wavelengths, due to the irradiation wavelength at 650 nm. Also, agglomeration of nanoparticles are responsible for big sizes and therefore the red shift, as observed in Fig. 5.5. Another absorption bands between the characteristic peak of anisotropic structures and that corresponding to the irradiation wavelength indicate a multiple modal size distribution[29] as a result of the initial polydispersed system of silver nanoparticles, as Fig. 5.12 confirms. Other reason is the presence of different shapes that generate other SPRs, as a consequence of the internal crystal structure of silver nanoparticles which depends on the defects caused in the nucleation step[19]. These SPR absorption bands are attributed to the in-plane quadrupole

resonances [110]. The irradiation wavelengths green 540 nm, red 650 nm and white 200-700 nm reveals more than two SPR, due to a bimodal size and shape distribution [29].

Figure 5.13 (b) shows the UV-Vis spectra of AgTNPs/GO nanocomposite by *in-situ* method irradiated with different wavelengths. As in AgTNPs case, the spectra present two absorption bands characteristic of anisotropic structures. This confirms that the proposed *in-situ* method results in the formation of anisotropic shaped nanoparticles. Table 5.4 corresponds to the AgTNPs/GO nanocomposite by *in-situ* method spectra and describes the SPR bands positions observed.

In-situ method AgTNPs/GO	Peak	Position[nm]	Assignment
Blue 440 nm			
	1	340	Weak SPR characteristic peak of triangular nanoplates[11]coming from out-of-plane quadrupole resonances[110]
	2	500	Characteristic peak of triangular nanoplates depending on the irradiation wavelength used in the photoreduction process[110] and it comes from the in-plane dipole resonance[111]
Green 540 nm			
	1	330	Weak SPR characteristic peak of triangular nanoplates[11]coming from out-of-plane quadrupole resonances[110]
	2	570	Characteristic peak of triangular nanoplates depending on the irradiation wavelength used in the photoreduction process[110] and it comes from the in-plane dipole resonance[111]
Red 650 nm			
	1	330	Weak SPR characteristic peak of triangular nanoplates[11]coming from out-of-plane quadrupole resonances[110]
	2	520	Weak SPR attribute to different nanoparticle sizes[111], and plate-like structures[117]. It comes from in-plane quadrupole resonances[110]
	3	780	Characteristic peak of triangular nanoplates depending on the irradiation wavelength used in the photoreduction process[110] and it comes from the in-plane dipole resonance[111]
White 200-700 nm			
	1	330	Weak SPR characteristic peak of triangular nanoplates[11]coming from out-of-plane quadrupole resonances[110]
	2	460	Weak SPR attribute to different nanoparticle sizes[111], and spherical shape[117]. It comes from in-plane quadrupole resonances[110]
	3	640	Characteristic peak of triangular nanoplates depending on the irradiation wavelength used in the photoreduction process[110] and it comes from the in-plane dipole resonance[111]

Table 5.4: Table of UV–Vis SPR bands positions of *in-situ* method AgTNPs/GO nanocompposite SPR bands

Blue 440 nm nanocomposite spectra has two SPR: the first SPR is a weak peak located at 340 nm, it is attributed to a characteristic peak of anisotropic structures[11], and the second SPR is a strong peak located at 500 nm corresponding to characteristic peak of triangular nanoplates due to the irradiation wavelength[110]. With respect to the SPR observed in the AgTNPs spectra, no large shifts in the position of the peaks are noted indicating low growth.

Green 540 nm nanocomposite spectra has two SPR: the first weak SPR is located at 330 nm and it is a characteristic peak of triangular nanoplates[11]. The second peak located at 570 nm is a strong SPR associated with the irradiation wavelength used in the photoreduction process[110]. Unlike the AgTNPs spectra which has four SPR bands, this spectra has only two, indicating a monomodal size distribution due to the nanoparticles sizes are around 30 nm, which is corroborated with TEM characterization, review Fig. 5.8.

Red 650 nm nanocomposite reveals three SPR: the first at 330 nm is a weak SPR characteristic peak of triangular nanoplates[11]. The second SPR is located at 520 nm and corresponds to different nanoparticle sizes, and plate like shapes[111]. The third SPR is at 780 nm and is associated with the irradiation wavelength used in the photoreduction process[110]. Compared to AgTNPs, the SPR corresponding to irradiation wavelength for the nanocomposite has a blue-shift of 45 nm indicating a smaller size of nanoparticles than in AgTNPs.

Finally, for white 200-700 nm nanocomposite the spectra reveals three peaks: the first peak at 330 nm is a characteristic weak SPR of anisotropic structures[11] and it is present in all the nanocomposites samples, demonstrating that anisotropic and plate-like forms were obtained after photoreduction process. The second peak is located at 460 nm and it is attributed to different nanoparticle sizes indicating a bimodal size distribution[111]. With respect to AgTNPs, this peak shows a 10 nm red-shit associated with increased growth in nanoparticle size. The third peak at 640 nm is the one that depends on the irradiation wavelength[110] used in the photoreduction process. This SPR band has a blue-shift of 40 nm attributed to smaller nanoparticles than in AgTNPs. The red 650 nm and white 200-700 nm irradiation wavelengths presents more than two SPR related to different nanoparticles sizes, having an multiple modal size distribution. As we confirmed in the Fig. 5.5 and Fig. 5.6.

UV-Vis characterization showed that all nanocomposites made by the *in-situ* method contain nanoparticles with anisotropic structure. These shapes are observed for the green 540 nm and white 200-700 nm AgTNPs/GO nanocomposites, in the Fig. 5.8 and Fig. 5.6 characterizations, respectively.

5.2.5 Photoluminescence (PL)

Photoluminescen (PL) spectra were obtained with 332 nm excitation. PL was done in order to obtain information about the presence, size distribution, and concentration of nanoparticles in the nanocomposite. Size particles are analysed by the presence of peaks and its broadening[118], while concentration of nanoparticles is related to the peak PL intensity[93]. Figure 5.14 shows the PL spectra of graphene oxide pristine (GO Pristine) (a) and silver nanoparticles (AgNPs) (b). Fig. 5.14 (a) Shows three emission peaks at 380 nm, 550 nm and 700 nm which are in agreement with

Lan *et al.*[93]. The PL spectra of GO emission is caused by electron transitions of non–oxidized carbon region and oxidized carbon atoms[93].
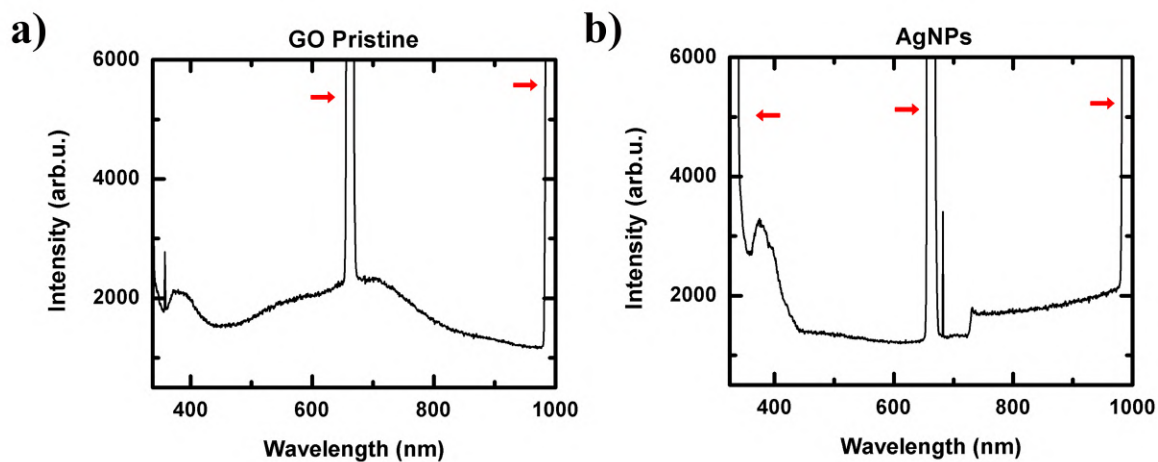
Figure 5.14: PL spectra of graphene oxide pristine (GO Pristine) (a) and silver nanoparticles (AgNPs) (b).

Fig. 5.14 (b) exhibits a characteristic peak of silver nanoparticles at 400 nm, Yeshchenko *et al.*[119] identify this peak as B giving information about the size of the nanoparticles. The B band present means that the silver nanoparticles have small sizes[119] around 8-11 nm, as we saw in Fig 5.7. The red arrows indicate the first and second modes signals coming from the lamp equipment and very thin peaks are considered noise. In the Table 5.5 the characteristic and main peaks of Figure5.14 are described.

Sample	Peak	Position[nm]	Assignment
Graphene oxide pristine (GO pristine)			
	1	380	Non- oxidized carbon region[93].
	2	550	boundary of oxidized carbon atoms[93].
	3	700	Water signal[93].
Silver nanoparticles(AgNPs)			
	1	375	Characteristic peak for silver nanoparticles 8-11 nm, corresponds to the B band given by to the interband sp $\rightarrow$ d radiative transitions[119]
	2	680	Noise

Table 5.5: Table of PL characteristic SPR bands of graphene oxide pristine (GO Pristine) and silver nanoparticles (AgNPs).

Graphene oxide PL spectra shows three emission bands: the first at 380 nm corresponding to non- oxidized carbon region[93]. The second peak is located at 550 nm and it os atrributed to boundary of oxidized carbon atoms[93]. The third peak at 700 nm comes from the water signal[93]. For silver nanoparticles a characteristic peak located at 375 nm is observed, this is related with the B band given by to the interband sp$\rightarrow$ d radiative transitions, the thinnest peak the smallest nanoparticles 8-11 nm[119].

Figure 5.15 shows the PL spectra of silver triangular nanoplates (AgTNPs) (a) and silver triangular nanoplates deposited on graphene oxide (AgTNPs/GO) by *in-situ* method (b), both irradiated at blue 440 nm, green 540 nm, red 650 nm and white 200-700 nm wavelengths. Fig. 5.15 (a) reveals the PL spectra of silver triangular nanoplates (AgTNPs).
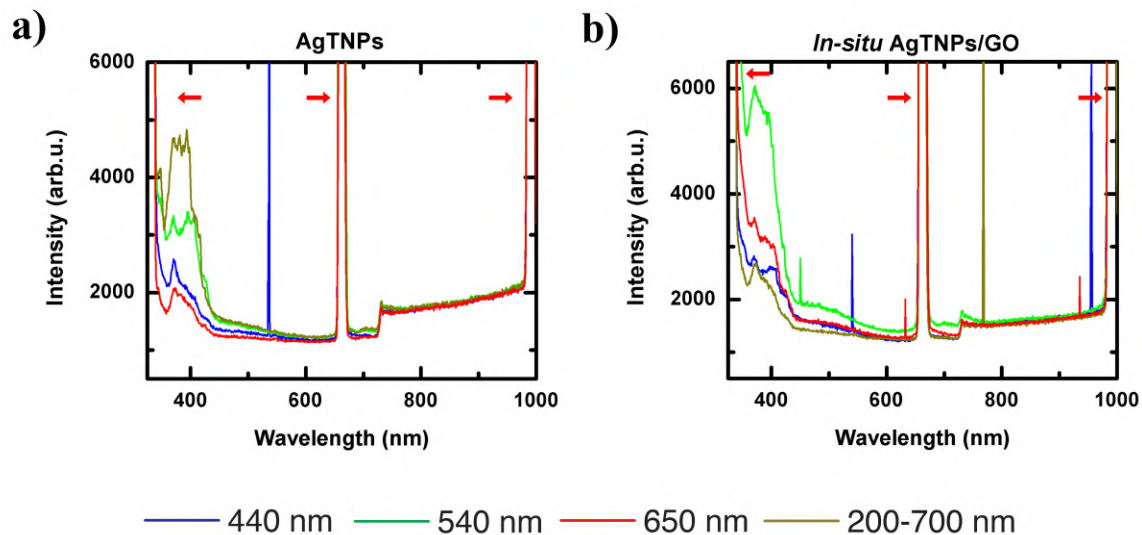
Figure 5.15: PL spectra of silver triangular nanoplates (AgTNPs) (a) and silver triangular nanoplates deposited on graphene oxide by *in-situ* method (*In-situ* AgTNPs/GO), both irradiated at blue 440 nm, green 540 nm, red 650 nm and white 200-700 nm wavelength.

For the analysis of these spectra, the red arrows indicate the first and second modes signals coming form the lamp equipment, and very sharp peaks are considered noise in the spectra. 5.15 a) Reveals a characteristic peak for silver nanoparticles, it is located around 375-400 nm, the thinnest peak the smallest nanoparticles 8-11 nm[119] as noted for silver nanoparticles 5.14b). In the Table 5.6 main characteristic peaks are described.

AgTNPs	Peak	Position[nm]	Assignment
Blue 440 nm			
	1	370	Characteristic peak for small silver nanoparticles 5-11 nm, corresponds to the B band given by to the interband sp $\rightarrow$ d radiative transitions [119]
	3	535	
Green 540 nm			
	1	340	Characteristic peak of bulk silver, it is atributed to direct radiative interband recombination of the conduction sp-band electrons with holes in the valence d band [120]
	2	400	Characteristic peak for silver nanoparticles, corresponds to the B band given by the coupling of the incoming exciting and outgoing emitted photons with SPR [119]
Red 650 nm			
	1	370	Characteristic peak for silver nanoparticles, corresponds to the B band given by the coupling of the incoming exciting and outgoing emitted photons with SPR [119]
White 200-700 nm			
	1	340	Characteristic peak of bulk silver, it is atributed to to direct radiative interband recombination of the conduction sp-band electrons with holes in the valence d band [120]
	2	400	Characteristic peak for silver nanoparticles, corresponds to the B band given by the coupling of the incoming exciting and outgoing emitted photons with SPR [119]

Table 5.6: Table of PL characteristic SPR bands of silver triangular nanoplates (AgTNPs), corresponding to figure 5.15 (a)

Blue 440 nm irradiation wavelength for AgTNPs shows one characteristic peak at 370 nm corresponding to the B band given by to the interband sp $\rightarrow$ d radiative transitions [119]. This peak is sharp indicating small nanoparticles of 5-11 nm of sizes. Green 540 nm AgTNPs reveals two peaks: the first peak at 340 nm, characteristic of bulk silver and it is attributed to direct radiative interband recombination of the conduction sp-band electrons with holes in the valence d band [120]. The second peak is located at 400 nm, characteristic of silver nanoparticles, it is atrributed to the B band given by the coupling of the incoming exciting and outgoing emitted photons with SPR [119]. Red 650 nm irradiation wavelength for AgTNPs shows one charactristic peak at 370 nm that corresponds to silver nanoparticles,it comes from the B band given by the coupling of the incoming exciting and outgoing emitted photons with SPR [119]. White 200-700 nm irradiation wavelength ehibit two peaks: the first at 340 nm attributed to bulk silver and the second peak located at 400 nm corresponding to characteristic peak for silver nanoparticles [93]. For green 540 nm,

red 650 nm and white 200-700 nm, the main peak is wider than blue 440 nm sample, this is associated with bigger nanoparticles sizes. Green 540 nm and white 200-700 nm PL peaks shows a saw shape which is related with different nanoparticles sizes[16].

Figure 5.15 (b) shows the PL spectra of AgTNPs/GO nanocomposites irradiated with different wavelengths. The red arrows indicates the first and second modes signals coming form the lamp equipment and the stand in 730 nm is atrributed to water signal[93]. PL spectra present a characteristic peak for silver nanoparticles located at 370-400 nm[119], the ragged shapes corresponds to different nanoparticles sizes[16] as discussed for AgTNPs (a). In the Table 5.7 characteristic peaks are described.

In-situ AgTNPs/GO)	Peak	Position[nm]	Assignment
Blue 440 nm			
	1	400	Characteristic peak for silver nanoparticles, corresponds to the B band given by the coupling of the incoming exciting and outgoing emitted photons with SPR[119]
Green 540 nm			
	1	370	Characteristic peak for silver nanoparticles, corresponds to the B band given by the coupling of the incoming exciting and outgoing emitted photons with SPR[119]
Red 650 nm			
	1	400	Characteristic peak for silver nanoparticles, corresponds to the B band given by the coupling of the incoming exciting and outgoing emitted photons with SPR[119]
White 200-700 nm			
	1	370	Characteristic peak for silver nanoparticles, corresponds to the B band given by the coupling of the incoming exciting and outgoing emitted photons with SPR[119]

Table 5.7: Table of PL characteristic SPR bands of silver triangular nanoplates deposited on graphene oxide by *in-situ* method (*In-situ* AgTNPs/GO), corresponding to figure 5.15 (b).

Blue 440 nm nancomposite exhibit the main characteristic peaks for silver nanoparticles, it comes from the B band given by the coupling of the incoming exciting and outgoing emitted photons with SPR[119]. Green 540 nm nanocomposite reveals the caracteristic peak for silver nanoparticles as well as for red 650 nm and white 200-700 nm nanocomposites samples. Its width, that is larger than blue nanocomposite, indicates bigger nanoparticles. As we saw in Fig. 5.8, Fig. 5.5 and Fig. 5.6. Besides, the PL spectra with highest intensity corresponds to green 540 nm nanocomposite samples due to the high concentration of nanoparticles observed in Fig. 5.8. AgTNPs vs AgTNPs/GO spectra shows that for the nanocomposite there are larger nanoparticles than for triangular silver nanoplates alone. The reason is that the graphene oxide can promote the growth of nanoparticles[24] due to its reactive sites at the edges and surface[28].

5.3 Antibacterial Properties

5.3.1 Antimicrobial Disk Diffusion Test

In this section we present the antibacterial behaviour of graphene oxide dispersed (1.4 GO), silver nanoparticles (1.1 AgNPs), silver triangular nanoplates (2. AgTNPs) and silver triangular nanoplates deposited on graphene oxide by *in-situ* method (4.*in-situ* AgTNPs/GO nanocomposite) irradiated with 440 nm (blue), 540 nm (green), 650 nm (red) and white 200-700 nm. Samples were tested by the antimicrobial disk diffusion test against E. coli, in order to make a qualitative analysis. As a result, an inhibition growth zone (halo) is present and it reflects the magnitude of susceptibility to microorganisms[39] Results are interpreted as: if the sample shows an inhibition zone, seen as halo, it has antibacterial properties, if it does not presents the halo, it does not have antibacterial behavior. This test is the first step to make quantitative tests as optical density showed later. 5. *Ex-situ* samples were conducted with a different method than the one presented, as this research is still ongoing. The analysis for these samples is not performed.

Ampicillin with a concentration of 10^{-2} g/L (Amp-2) and 10^{-3} g/L (Amp-3) were used as antibiotic controls. Ampicillin is a b-lactam antibiotic with excellent antimicrobial properties, but its instability limits its application[50]. It has been reported that Ag/GO nanocomposites have equivalent antibacterial efficiency in comparison to that of ampicillin[50]. For this reason is important to use ampicillin antibiotic as control, and for future comparison.

Figure 5.16 shows the zones of inhibition growth for the control ampicillin 10^{-3} (Amp-3), graphene oxide dispersed (1.4 GO) and silver nanoparticles (1.1 AgNPs).
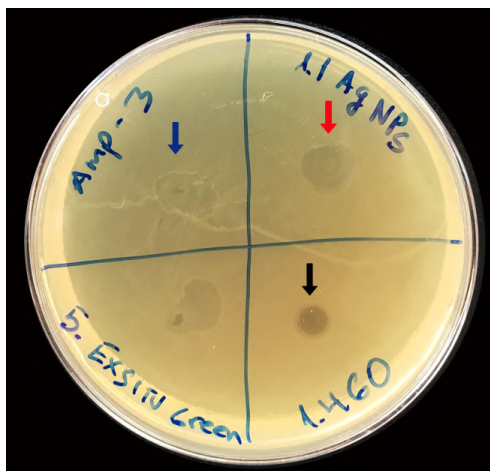
Figure 5.16: Zone of inhibition growth produced by ampicillin 10^{-3} (Amp-3) as the control, graphene oxide dispersed (1.4 GO) and silver nanoparticles (1.1 AgNPs), on agar petri plate.

The arrows indicates: the blue arrow shows the halo for the control ampicillin 10^{-3}, the red arrow reveals the inhibition zone for silver nanoparticles and the black arrow points to the halo from graphene oxide dispersed solution.

The presence of these halos confirms that silver nanoparticles and graphene oxide has antibacterial properties.

Figure 5.17 presents the inhibition zones for silver triangular nanoplates (2. AgTNPs) and silver triangular nanoplates deposited on graphene oxide by *in-situ* method, both irradiated with different wavelengths as blue 440 nm (blue), green 540 nm (green), red 650 nm (red) and white 200-700 nm (yellow).
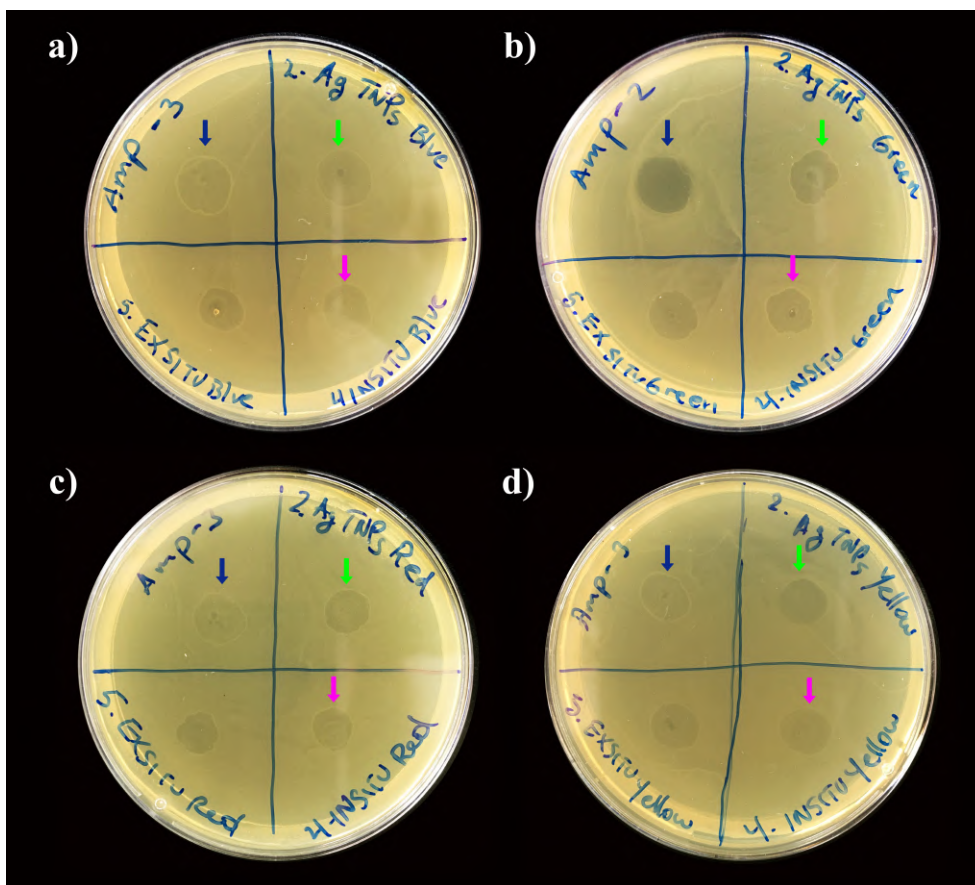
Figure 5.17: Zone of inhibition growth produced by ampicillin 10^{-3} and 10^{-2} as the controls, silver triangular nanoplates (2. AgTNPs) and silver triangular nanoplates deposited on graphene oxide by *in-situ* method, the last two irradiated at (a) blue 440 nm (blue), (b) green 540 nm (green), (c) red 650 nm (red), and (d) white 200-700 nm (yellow).

The green arrows shows the inhibition growth zone for silver triangular nanoplates , for all the irradiation wavelengths AgTNPs reveals antibacterial behaviour. The pink arrows indicates the inhibition growth zone, observed as halos, for AgTNPs/GO nanocomposites and all of them presents antibacterial activity.

After checking that the samples tested show antibacterial activity, the AgTNPs/GO nanocomposite vs AgNPs samples are quantified and compared in the following Optical Density section.

5.3.2 Optical Density(OD)

The microbial growth kinetics was studied based on the value of optical densities absorbance at 600 nm as a function of time. Optical density indicates the concentration of bacteria cells at each time. One drop of each sample was used to measure its absorbance in intervals of 30 minutes.

Gram-negative (G-) bacterial strain E. coli was chosen as the model organisms for evaluating antibacterial activity of samples. Figure 5.18 shows the microbial growth curve for the blank, that is the bacteria with out antibiotic or sample, silver nanoparticles (AgNPs), silver nanoparticles deposited on graphene oxide (AgNPs/GO), silver triangular nanoplates (AgTNPs), and AgTNPs/GO nanocomposites, the last two irradiated at different wavelengths.
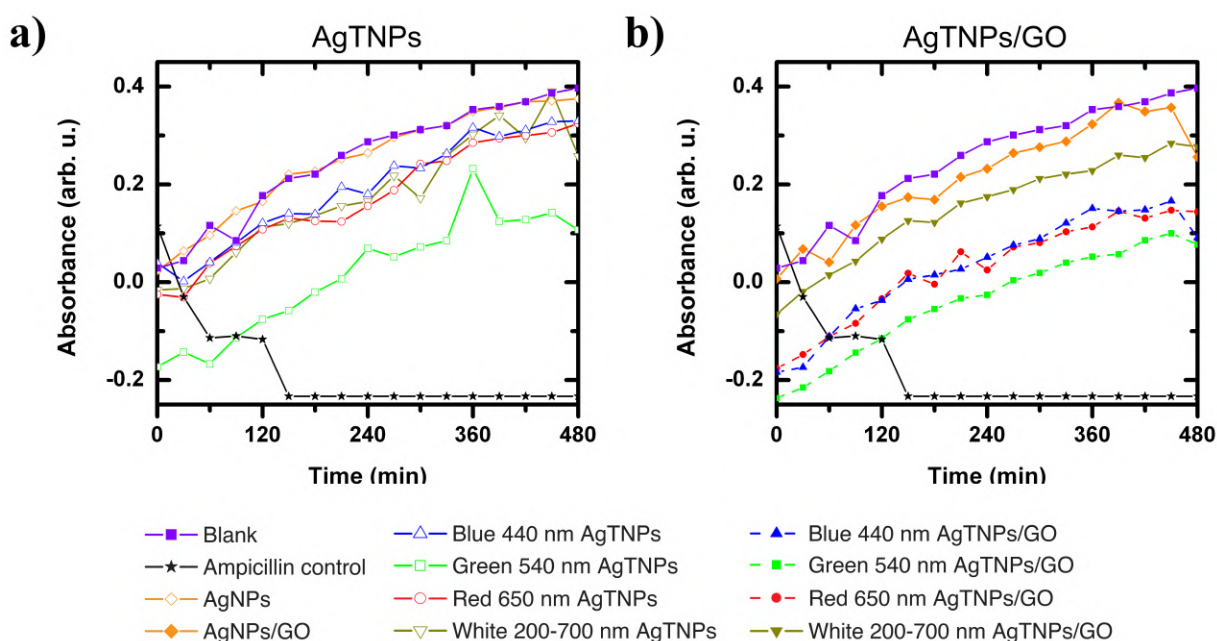
Figure 5.18: Optical density of blank and ampicillin $0.05g/L$ (Amp control)with; a) silver nanoparticles with out graphene oxide (GO): silver nanoparticles (AgNPs) and silver triangular nanoplates (AgTNPs), and b) silver nanoparticles with GO: silver nanoparticles deposited on graphene oxide (AgNPs/GO) and silver triangular nanoplates deposited on graphene oxide (AgTNPs/GO) nanocomposites. AgTNPs and AgTNPs/GO both irradiated at blue 440 nm, green 540 nm, red 650 nm, and white 200-700 nm.

Figure 5.18 reveals bacteria growth curves with a logarithm behavior which is in agreement with Zwietering M. *et al.*[104]. As an exception, ampicillin antibiotic used as control shows a decay curve indicating complete death of the bacteria. The growth curves reveals the exponential phase given by the exponential growth of bacteria cells, and it tends to the stationary phase. The stationary phase reveals the limitation of nutrition sources, and the

accumulation of waste products[103]. Fig. 5.18 (a) presents the growth curves corresponding to silver nanoparticles with out graphene oxide. While 5.18 (b) reveals the curves of silver nanoparticles deposited on graphene oxide (with GO) nanocomposites, to observed the contribution of GO in the antibacterial properties. As can be observed silver nanoparticles with graphene oxide samples shows lower absorbance values compared to silver nanoparticles alone. To analyse quantitatively the antibacterial properties, optical density (OD) was calculated with 3.2 equation, where the initial and final absorbance values are needed. Table 5.8 shows the initial and final absorbance values for each sample: blank, ampicillin control, AgNPs, AgNPs/GO, AgTNPs, and AgTNPs/GO nanocomposites.

Sample	x_2 (arb. u.)	x_1 (arb. u.)
Blank	0.397	0.029
Ampicillin control	0.114	-0.233
AgNPs	0.375	0.023
AgNPs/GO	0.007	0.256
Blue 440 nm AgTNPs	0.039	0.33
Green 540 nm AgTNPs	-0.173	0.107
Red 650 nm AgTNPs	-0.025	0.324
White 200-700 nm AgTNPs	-0.016	0.258
Blue 440 nm AgTNPs/GO	0.091	-0.184
Green 540 nm AgTNPs/GO	0.077	-0.237
Red 650 nm AgTNPs/GO	0.144	-0.176
White 200-700 nm AgTNPs/GO	0.277	-0.065

Table 5.8: Table of initial and final absorbance values for the blank, ampicillin control, silver nanoparticles (Ag-NPs), silver nanoparticles deposited on graphene oxide (AgNPs/GO), silver triangular nanoplates (AgTNPs), and AgTNPs/GO nanocomposites the last two irradiated at blue 440 nm, green 540 nm, red 650 nm, and white 200-700 nm wavelengths.

Absorbance negative values are given by the discalibration of the equipment or by the loss of precision when it is measuring turbid solutions. However, the trend of the growth curve does not change, so we work with these values and calculate the calibrated ones by adding a unit. Table 5.9 shows the calibrated absorbance and optical density (OD) values.

Sample	x_2 (arb. u.)	x_1 (arb. u.)	Optical Density
Blank	1.397	1.029	-0.133
Ampicillin control	1.114	0.767	0.162
AgNPs	1.375	1.023	-0.128
AgNPs/GO	1.007	1.256	-0.096
Blue 440 nm AgTNPs	1.039	1.33	-0.107
Green 540 nm AgTNPs	0.827	1.107	-0.127
Red 650 nm AgTNPs	0.975	1.324	-0.133
White 200-700 nm AgTNPs	0.984	1.258	-0.107
Blue 440 nm AgTNPs/GO	1.091	0.816	-0.126
Green 540 nm AgTNPs/GO	1.077	0.763	-0.149
Red 650 nm AgTNPs/GO	1.144	0.824	-0.142
White 200-700 nm AgTNPs/GO	1.277	0.935	-0.135

Table 5.9: Table of calibrated absorbance initial and final values and optical density (OD) for the blank, ampicillin control, AgNPs, AgNPs/GO, AgTNPs, and AgTNPs/GO nanocomposites the last two irradiated at blue 440 nm, green 540 nm, red 650 nm, and white 200-700 nm wavelengths.

The optical density (OD) calculations reveals values as: for the blank the OD is -0.133, while for ampicillin control is 0.162. Negatives OD values reveals the growth of the bacteria, while positive values, as observed in the ampicillin control, indicates the decline of the curve or that the bacteria did not grow. For AgNPs the OD is -0.128, while for AgNPs/GO is -0.096, indicating that AgNPs/GO has a lower concentration of bacteria cells which means better antibacterial property than AgNPs. For AgTNPs irradiated at different wavelengths the OD are: for blue 440 nm is -0.107, green 540 nm has -0.127 OD, for red 650 nm is -0.133, and for white 200-700 nm is -0.107. The highest negative OD values corresponds to AgTNPs green 540 nm and red 650 nm, showing the lowest concentrations of bacteria cell. Finally, for AgTNPs/GO nanocomposites the OD values are: for blue 440 nm is -0.126, for green 540 nm -0.149, red 650 nm has -0.142, and for white 200-700 nm is -0.135. The highest negative OD values corresponds to green 540 nm and red 650 nm, revealing lower concentrations and better antibacterial property among nanocomposites. These confirms the growth of the bacteria during the experiment, and a previous analysis of the antibacterial efficiency.

To compare the antibacterial efficiency of the samples, the displacement of the curves with respect to the blank was calculated. Each point on the curve was subtracted from the blank, and the results were averaged for each sample. The more curve displacement there is, the more antibacterial efficiency it shows. Table 5.10 shows the displacement values calculated for the ampicillin control, AgNPs, AgNPs/GO, AgTNPs, and AgTNPs/GO nanocomposites.

Sample	Displacement(arb. u.)	Efficiency (%)
Ampicillin control	0.428	100
AgNPs	0.001	1
AgNPs/GO	0.034	8
Blue 440 nm AgTNPs	0.057	13
Green 540 nm AgTNPs	0.233	54
Red 650 nm AgTNPs	0.079	18
White 200-700 nm AgTNPs	0.074	17
Blue 440 nm AgTNPs/GO	0.218	51
Green 540 nm AgTNPs/GO	0.287	67
Red 650 nm AgTNPs/GO	0.220	51
White 200-700 nm AgTNPs/GO	0.097	23

Table 5.10: Table of curve displacements between the blank and: ampicillin control, AgNPs, AgNPs/GO, AgTNPs, and AgTNPs/GO nanocomposites, the last two irradiated at blue 440 nm, green 540 nm, red 650 nm, and white 200-700 nm.

For ampicillin control is 0.428 showing the largest displacement due to the concentration of the antibiotic, and because it was used as a control in this experiment. Then, for AgNPs the displacement is 0.001, while for AgNPs/GO is 0.034 revealing a better antibacterial behaviour when the GO is added. Next, a comparison between AgTNPs and AgTNPs/GO nanocomposite is presented. For blue 440 nm, AgTNPs has a displacement of 0.057, while nanocomposite presents 0.218. Green 540 nm AgTNPs shows a displacement of 0.233, while the nanocomposite reveals 0.287 value. Red 650 nm AgTNPs has 0.079, while the nanocomposite shows 0.220 of displacement. Finally, white 200-700 nm AgTNPs presents 0.074 of displacement, while the nanocomposite reveals 0.097. For all the cases, the addition of GO causes an increase in the displacement value, which is directly related to the antibacterial efficiency as table 5.10 shows. The improvement between AgNPs and AgNPs/GO is 7 %, while for blue 440 nm AgTNPs and AgTNPs/GO nanocomposite is 38 %. Comparing between green 540 nm AgTNPs and AgTNPs/GO the improvement is 13 %. For red 650 nm sample, the increase is 33%, while for white 200-700 nm is 6%. The improvement in the antibacterial efficiency is due to the synergistic effect[50] of AgTNPs and GO[51]. This effect is also called "capturing-killing process" and it is explained in the introduction section.

To better observe the improvement of antibacterial properties of single nanoparticles versus nanoparticles with graphene oxide, a bar graph is shown in Fig. 5.19, taking the absorbance values at the time 420 min for blank, AgNPs, AgNPs/GO, AgTNPs, and AgTNPs/GO nanocomposites.
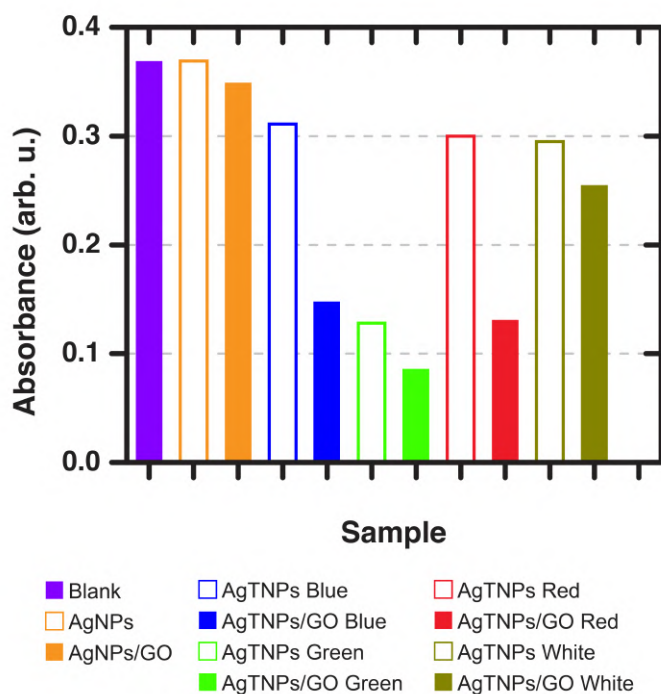
Figure 5.19: Comparison bar graph of absorbance values taken at 420 min from the growth curves shown in Fig. 5.18, for blank, AgNPs, AgNPs/GO, AgTNPs, and AgTNPs/GO nanocomposites, the last two irradiated at blue 440nm, green 540 nm, red 650 nm, and white 200-700 nm.

The absorbance value reveals the concentration of bacterial cell in the solution measured. Therefore, the lower the absorbance values, the less bacteria are present, and the better the antibacterial efficiency. Then, AgNPs does not present significant antibacterial efficiency due to its high absorbance value. Comparing silver nanoparticles with silver nanoparticles deposited on graphene oxide, in all cases there is a decrease in the absorbance value, which means that the addition of graphene oxide improves the antibacterial efficiency.

5.3.3 Dependence of concentration, size, and shape of nanoparticles deposited on graphene oxide, on antibacterial properties

Antibacterial properties is dependent on the concentration of deposited nanoparticles on the graphene oxide[39]. The more nanoparticles there are, the greater the possibility of contact between them and the cell membrane. This results in increased cell membrane permeability[55,56] and as explained in the introduction section, the intracellular passage of nanoparticles and ions results in irreversible damage and eventually the death of the bacterial cell. Another advantage of the high concentration of nanoparticles in the nanocomposite is a decreasing effect in the negative charge of GO,

promoting greater adsorption[47] given by the oxygen functionalities, and therefore is a greater probability of silver nanoparticles-cell membrane contact.

Regarding the size dependence of nanoparticles, it has been reported[121] that nanoparticles by themselves have an antibacterial effect that increases with the reduction of the size of the nanoparticles,[39]. Small nanoparticles can penetrate more easily than the big ones[51]. Besides, it is reported[49] that silver nanoparticles with sizes between 1 and 10 nm (as we saw in Fig. 5.7)showed anisotropic shapes as planar twinned, octahedral, icosahedral, and decahedral. These structures predominantly has (100) facets with small percentage of (111) facets[49]. The (111) facets are high-atom-density facets and therefore, they has high reactivity[49]. Then, silver triangular nanoplates has better antibacterial properties than silver nanoparticles, due to its structural configuration containing (111) facets[49]. The deposition of silver triangular nanoplates on graphene oxide increased the antibacterial efficiency owing to the synergistic effect produced by AgTNPs and GO. AgTNPs containing (111) facets with high reactivity, and GO by their strong adsorption properties.

Among the AgTNPs/GO nanocomposites irradiated with different wavelengths, the green 540 nm nanocomposite had most of its nanoparticles photoconverted to triangular nanoplates, and also it exhibited a high concentration of them. Higher photo conversion to triangular nanoparticles means more high-atom-density facets (111) and more reactivity from the sample[49]. While a high concentration of nanoparticles increase the possibility of contact with cell membrane. With respect to white 200-700 nm nanocomposite, anisotropic structures were also observed in Fig. 5.6. However, these nanoparticles are very large compared to green 540 nm nanocomposite, which does not benefit the antibacterial properties owing to smaller nanoparticles are preferred so that they can penetrate the membrane.

Chapter 6

Conclusions & Outlook

In the photochemical reduction process, the role of the irradiation wavelength is significant, owing to it affect the size and shape of nanoparticles [11]. Since all the samples were irradiated by the same time, the effect on the photoconverison process depends mainly of the irradiation wavelength. Increasing the wavelength of irradiation, increases the anisotropy of the final nanoparticle [108]. To confirm this dependence and the formation of AgTNPs/GO nanocomposite: SEM, TEM, Raman spectroscopy, UV-Vis spectroscopy and PL characterization were done.

SEM micrographs presents AgNPs deposited on GO. The highest AgNPs concentration was seen for green 540 nm AgTNPs nanocomposite. TEM micrographs were measure for blue 440 nm and green 540 nm nanocomposites. It was noted that green 540 nm nanocomposite has more nanoparticles photo converted to triangular nanoplates, while blue 440 nm shows small sizes corresponding to initial silver nanoparticles. UV-Vis espectroscopy exhibited spectra with two characteristic absorption bands coming from the SPR of anisotropic structures. Finally, PL spectra revealed a characteristic peak of silver nanoparticles located at ~400 nm. Characterization techniques demonstrated that effectively the silver nanoparticles are deposited on graphene oxide, and anisotropic structures such as triangular, hexagonal, pentagonal, and cubic were found. The presence of anisotropic structures confirms that the photoreduction method is an efficient and low-cost method to obtain AgTNPs/GO nanocomposite.

Antibacterial properties were tested by antimicrobial disk diffusion and optical density tests. Antimicrobial disk diffusion test confirms that qualitatively the nanoparticles and nanocomposites has antibacterial behavior due to the halo observed. Then, optical density showed growth bacteria curves with the exponential and stationary phases. Curve displacements were calculated with respect to the blank. Comparing between AgNPs and AgTNPs versus AgNPs/GO and AgTNPs/GO respectively, nanocomposites showed increased displacement values which directly influence in the antibacterial efficiency. This is due to the synergistic effect between silver nanoparticles and graphene oxide. AgTNPs/GO nanocomposites improved the antibacterial efficiency as compared to AgNPs/GO, demonstrating that silver triangular nanoplates shape influence in the antibacterial properties. Finally, green 540 nm AgTNPs/GO revealed the larger displacement and the highest antibacterial efficiency, due to it had the greatest photoconversion to triangular nanoplates and highest concentration of nanoparticles.

From the antibacterial point of view, the nanocomposite proposed in this project is an alternative for antibiotics,

since ampicillin is unstable which limits its uses and applications. Besides, an study of toxicity of silver nanoparticles and graphene oxide should be done. From the nanostructural perspective, further investigations about the effect of the photoreduction process on graphene oxide is open. Actually, this project is going in deep analysis of Raman spectra results. Also, complementary techniques as Fourier Transform Infrared Spectroscopy (FTIR), and X-ray Photoelectron Spectroscopy (XPS) can be done, in order to identify any charge transfer between AgNPs and GO.

Appendix A

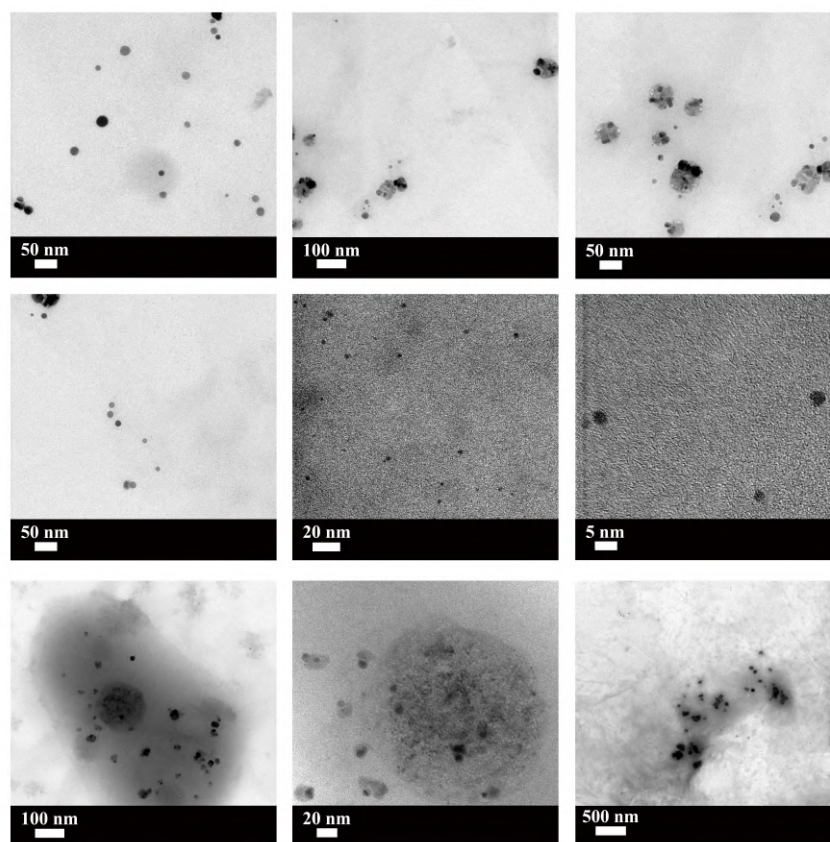# Complementary TEM micrographs for histograms.

Figure A.1: Complementary Bright-field micrographs for blue 440 nm AgTNPs/GO nanocomposite for the performance of the histogram shown in Fig. 5.7(c).
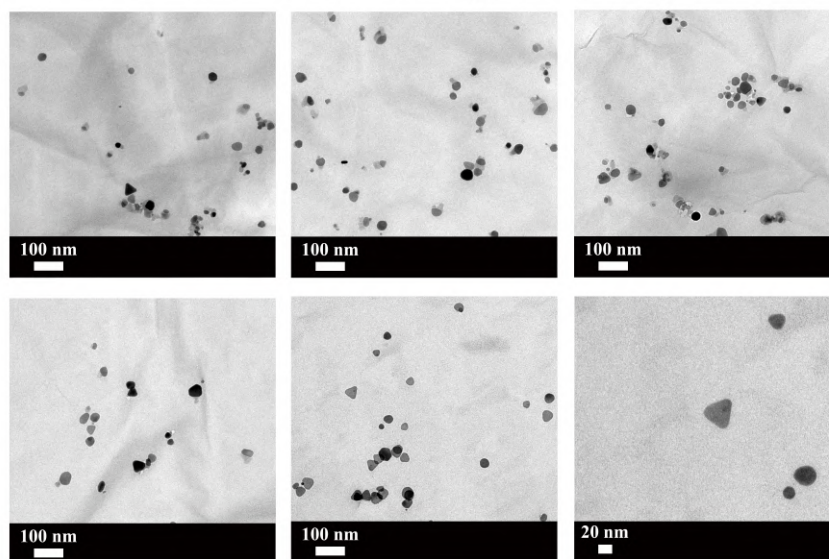
Green 540 nm AgTNPs/GO

Figure A.2: Complementary Bright-field micrographs for green 540 nm AgTNPs/GO nanocomposite for the performance of the histogram shown in Fig. 5.8(c).

Bibliography

[1] Chris Toumey. Plenty of room, plenty of history. *Nature nanotechnology*, 4(12):783, 2009.

[2] Štefan Luby, Martina Lubyová, Peter Šiffalovič, Matej Jergel, and Eva Majková. A brief history of nanoscience and foresight in nanotechnology. In *Nanomaterials and Nanoarchitectures*, pages 63–86. Springer, 2015.

[3] Florence Sanchez and Konstantin Sobolev. Nanotechnology in concrete–a review. *Construction and building materials*, 24(11):2060–2071, 2010.

[4] Chintamani Nagesa Ramachandra Rao, Achim Müller, and Anthony K Cheetham. *The chemistry of nanomaterials: synthesis, properties and applications*. John Wiley & Sons, 2006.

[5] Hari Singh Nalwa. *Nanostructured materials and nanotechnology: concise edition*. Elsevier, 2001.

[6] A Brioude and MP Pileni. Silver nanodisks: optical properties study using the discrete dipole approximation method. *The Journal of Physical Chemistry B*, 109(49):23371–23377, 2005.

[7] Ivan Sondi and Branka Salopek-Sondi. Silver nanoparticles as antimicrobial agent: a case study on e. coli as a model for gram-negative bacteria. *Journal of colloid and interface science*, 275(1):177–182, 2004.

[8] Jill E Millstone, Sarah J Hurst, Gabriella S Metraux, Joshua I Cutler, and Chad A Mirkin. Colloidal gold and silver triangular nanoprisms. *small*, 5(6):646–664, 2009.

[9] Stavroula Foteinopoulou, Jean-Pol Vigneron, and Cedric Vandenbem. Optical near-field excitations on plasmonic nanoparticle-based structures. *Optics Express*, 15(7):4253–4267, 2007.

[10] SATOSHI Horikoshi and NICK Serpone. Introduction to nanoparticles. *Microwaves in nanoparticle synthesis: fundamentals and applications*, pages 1–24, 2013.

[11] Jamil Saade and Cid B de Araújo. Synthesis of silver nanoprisms: a photochemical approach using light emission diodes. *Materials Chemistry and Physics*, 148(3):1184–1193, 2014.

[12] Wei Shao, Xiufeng Liu, Huihua Min, Guanghui Dong, Qingyuan Feng, and Songlin Zuo. Preparation, characterization, and antibacterial activity of silver nanoparticle-decorated graphene oxide nanocomposite. *ACS applied materials & interfaces*, 7(12):6966–6973, 2015.

[13] Jian Zhang, Mark R Langille, and Chad A Mirkin. Photomediated synthesis of silver triangular bipyramids and prisms: the effect of ph and bspp. *Journal of the American Chemical Society*, 132(35):12502–12510, 2010.

[14] K Lance Kelly, Eduardo Coronado, Lin Lin Zhao, and George C Schatz. The optical properties of metal nanoparticles: the influence of size, shape, and dielectric environment, 2003.

[15] María Escudero-Escribano. *Electrocatalysis and surface nanostructuring : atomic ensemble effects and non-covalent interactions*. PhD thesis, 11 2011.

[16] Peng Yang, Hervé Portales, and Marie-Paule Pileni. Identification of multipolar surface plasmon resonances in triangular silver nanoprisms with very high aspect ratios using the dda method. *The Journal of Physical Chemistry C*, 113(27):11597–11604, 2009.

[17] JJ Mock, M Barbic, DR Smith, DA Schultz, and S Schultz. Shape effects in plasmon resonance of individual colloidal silver nanoparticles. *The Journal of Chemical Physics*, 116(15):6755–6759, 2002.

[18] Hiroshi Yao and Taisuke Shiratsu. Multipolar surface magnetoplasmon resonances in triangular silver nanoprisms studied by mcd spectroscopy. *The Journal of Physical Chemistry C*, 121(1):761–768, 2017.

[19] Qiao Zhang, Na Li, James Goebl, Zhenda Lu, and Yadong Yin. A systematic study of the synthesis of silver nanoplates: is citrate a "magic" reagent? *Journal of the American Chemical Society*, 133(46):18931–18939, 2011.

[20] Humberto Palza. Antimicrobial polymers with metal nanoparticles. *International journal of molecular sciences*, 16(1):2099–2116, 2015.

[21] Meagan S Mauter and Menachem Elimelech. Environmental applications of carbon-based nanomaterials. *Environmental Science & Technology*, 42(16):5843–5859, 2008.

[22] Pulickel Madhavapanicker Ajayan. Nanotubes from carbon. *Chemical reviews*, 99(7):1787–1800, 1999.

[23] Diyar Sadyraliev. Graphene Oxide what is it, 2018. URL https://nanografi.com/blog/graphene-oxide-what-is-it/.

[24] Gil Goncalves, Paula AAP Marques, Carlos M Granadeiro, Helena IS Nogueira, MK Singh, and J Gracio. Surface modification of graphene nanosheets with gold nanoparticles: the role of oxygen moieties at graphene surface on gold nucleation and growth. *Chemistry of Materials*, 21(20):4796–4802, 2009.

[25] Chao Xu, Xin Wang, and Junwu Zhu. Graphene- metal particle nanocomposites. *The Journal of Physical Chemistry C*, 112(50):19841–19845, 2008.

[26] Huifang Liu, Linlin Zhong, KyuSik Yun, and Monica Samal. Synthesis, characterization, and antibacterial properties of silver nanoparticles-graphene and graphene oxide composites. *Biotechnology and bioprocess engineering*, 21(1):1–18, 2016.

[27] Jia Tang, Qian Chen, Ligeng Xu, Shuai Zhang, Liangzhu Feng, Liang Cheng, Huan Xu, Zhuang Liu, and Rui Peng. Graphene oxide–silver nanocomposite as a highly effective antibacterial agent with species-specific mechanisms. *ACS applied materials & interfaces*, 5(9):3867–3874, 2013.

[28] Sławomir Jaworski, Mateusz Wierzbicki, Ewa Sawosz, Anna Jung, Grzegorz Gielerak, Joanna Biernat, Henryk Jaremek, Witold Łojkowski, Bartosz Woźniak, Jacek Wojnarowicz, Leszek Stobiński, Artur Małolepszy, Marta Mazurkiewicz-Pawlicka, Maciej Łojkowski, Natalia Kurantowicz1, and André. Chwalibog. Graphene oxide-based nanocomposites decorated with silver nanoparticles as an antibacterial agent. *Nanoscale research letters*, 13:1–17, 2018.

[29] Can Xue, Gabriella S Métraux, Jill E Millstone, and Chad A Mirkin. Mechanistic study of photomediated triangular silver nanoprism growth. *Journal of the American Chemical Society*, 130(26):8337–8344, 2008.

[30] Pulickel M Ajayan, Linda S Schadler, and Paul V Braun. *Nanocomposite science and technology*. John Wiley & Sons, 2006.

[31] Jyotishkumar Parameswaranpillai, Nishar Hameed, Thomas Kurian, and Yingfeng Yu. *Nanocomposite Materials: Synthesis, Properties and Applications*. CRC Press, 2016.

[32] Ignác Capek. *Nanocomposite structures and dispersions*, volume 23. Elsevier, 2019.

[33] Rashmi H Prabhu, Vandana B Patravale, and Medha D Joshi. Polymeric nanoparticles for targeted treatment in oncology: current insights. *International journal of nanomedicine*, 10:1001, 2015.

[34] Farha Masood. Polymeric nanoparticles for targeted drug delivery system for cancer therapy. *Materials Science and Engineering: C*, 60:569–578, 2016.

[35] Jiayi Tang, Dong Chen, Qiaofeng Yao, Jianping Xie, and Jun Yang. Recent advances in noble metal-based nanocomposites for electrochemical reactions. *Materials today energy*, 6:115–127, 2017.

[36] Gopalu Karunakaran, Andrey Grigorjevich Yudin, Matheswaran Jagathambal, Arup Ratan Mandal, Nguyen Van Minh, Alexander Gusev, Evgeny Kolesnikov, and Denis Kuznetsov. Synthesis of five metal based nanocomposite via ultrasonic high temperature spray pyrolysis with excellent antioxidant and antibacterial activity. *RSC advances*, 6(44):37628–37632, 2016.

[37] Omkara Swami Muddineti, Balaram Ghosh, and Swati Biswas. Current trends in using polymer coated gold nanoparticles for cancer therapy. *International journal of pharmaceutics*, 484(1-2):252–267, 2015.

[38] Hyosuk Yun, Ji Dang Kim, Hyun Chul Choi, and Chul Won Lee. Antibacterial activity of cnt-ag and go-ag nanocomposites against gram-negative and gram-positive bacteria. *Bulletin of the Korean Chemical Society*, 34(11):3261–3264, 2013.

[39] Lei Huang, Hongtao Yang, Yanhua Zhang, and Wei Xiao. Study on synthesis and antibacterial properties of ag nps/go nanocomposites. *Journal of Nanomaterials*, 2016, 2016.

[40] Baojiang Jiang, Chungui Tian, Gang Song, Wei Chang, Guofeng Wang, Qian Wu, and Honggang Fu. A novel ag/graphene composite: facile fabrication and enhanced antibacterial properties. *Journal of Materials Science*, 48(5):1980–1985, 2013.

[41] Kai He, Zhuotong Zeng, Anwei Chen, Guangming Zeng, Rong Xiao, Piao Xu, Zhenzhen Huang, Jiangbo Shi, Liang Hu, and Guiqiu Chen. Advancement of ag–graphene based nanocomposites: An overview of synthesis and its applications. *Small*, 14(32):1800871, 2018.

[42] Dimitrios Konios, Minas M Stylianakis, Emmanuel Stratakis, and Emmanuel Kymakis. Dispersion behaviour of graphene oxide and reduced graphene oxide. *Journal of colloid and interface science*, 430:108–112, 2014.

[43] Yiming Zhang, Xun Yuan, Yuan Wang, and Yi Chen. One-pot photochemical synthesis of graphene composites uniformly deposited with silver nanoparticles and their high catalytic activity towards the reduction of 2-nitroaniline. *Journal of Materials Chemistry*, 22(15):7245–7251, 2012.

[44] Danhui Zhang, Xiaoheng Liu, and Xin Wang. Green synthesis of graphene oxide sheets decorated by silver nanoprisms and their anti-bacterial properties. *Journal of inorganic biochemistry*, 105(9):1181–1186, 2011.

[45] Wen Zhang, Ying Yao, Nicole Sullivan, and Yongsheng Chen. Modeling the primary size effects of citrate-coated silver nanoparticles on their ion release kinetics. *Environmental science & technology*, 45(10): 4422–4428, 2011.

[46] Ana Carolina Mazarin Moraes, Bruna Araujo Lima, Andreia Fonseca de Faria, Marcelo Brocchi, and Oswaldo Luiz Alves. Graphene oxide-silver nanocomposite as a promising biocidal agent against methicillin-resistant staphylococcus aureus. *International journal of nanomedicine*, 10:6847, 2015.

[47] Jizhen Ma, Jintao Zhang, Zhigang Xiong, Yu Yong, and XS Zhao. Preparation, characterization and antibacterial properties of silver-modified graphene oxide. *Journal of Materials Chemistry*, 21(10):3350–3352, 2011.

[48] Huanjun Zhang and Guohua Chen. Potent antibacterial activities of ag/tio2 nanocomposite powders synthesized by a one-pot sol- gel method. *Environmental science & technology*, 43(8):2905–2910, 2009.

[49] Sukdeb Pal, Yu Kyung Tak, and Joon Myong Song. Does the antibacterial activity of silver nanoparticles depend on the shape of the nanoparticle? a study of the gram-negative bacterium escherichia coli. *Appl. Environ. Microbiol.*, 73(6):1712–1720, 2007.

[50] Wei-Ping Xu, Le-Cheng Zhang, Jian-Ping Li, Yang Lu, Hui-Hui Li, Yi-Ni Ma, Wei-Di Wang, and Shu-Hong Yu. Facile synthesis of silver@graphene oxide nanocomposites and their enhanced antibacterial properties. *Journal of Materials Chemistry*, 21(12):4593–4597, 2011.

[51] Biao Song, Chang Zhang, Guangming Zeng, Jilai Gong, Yingna Chang, and Yan Jiang. Antibacterial properties and mechanism of graphene oxide-silver nanocomposites as bactericidal agents for water disinfection. *Archives of biochemistry and biophysics*, 604:167–176, 2016.

[52] Mohammad R Elahifard, Sara Rahimnejad, Saeed Haghighi, and Mohammad R Gholami. Apatite-coated ag/agbr/tio2 visible-light photocatalyst for destruction of bacteria. *Journal of the American Chemical Society*, 129(31):9552–9553, 2007.

[53] Parveen Kumar, Peipei Huo, Rongzhao Zhang, and Bo Liu. Antibacterial properties of graphene-based nanomaterials. *Nanomaterials*, 9(5):737, 2019.

[54] Hanaa M Hegab, Ahmed ElMekawy, Linda Zou, Dennis Mulcahy, Christopher P Saint, and Milena Ginic-Markovic. The controversial antibacterial activity of graphene-based materials. *Carbon*, 105:362–376, 2016.

[55] Gaoxing Su, Hongyu Zhou, Qingxin Mu, Yi Zhang, Liwen Li, Peifu Jiao, Guibin Jiang, and Bing Yan. Effective surface charge density determines the electrostatic attraction between nanoparticles and cells. *The Journal of Physical Chemistry C*, 116(8):4993–4998, 2012.

[56] Pavel Dibrov, Judith Dzioba, Khoosheh K Gosink, and Claudia C Häse. Chemiosmotic mechanism of antimicrobial activity of ag+ in vibrio cholerae. *Antimicrobial agents and chemotherapy*, 46(8):2668–2670, 2002.

[57] Katherine B Holt and Allen J Bard. Interaction of silver (i) ions with the respiratory chain of escherichia coli: an electrochemical and scanning electrochemical microscopy study of the antimicrobial mechanism of micromolar ag+. *Biochemistry*, 44(39):13214–13223, 2005.

[58] Thorsten Friedrich. The nadh: ubiquinone oxidoreductase (complex i) from escherichia coli. *Biochimica et Biophysica Acta (BBA)-Bioenergetics*, 1364(2):134–146, 1998.

[59] Qing Ling Feng, Jian Wu, GQ Chen, FZ Cui, TN Kim, and JO Kim. A mechanistic study of the antibacterial effect of silver ions on escherichia coli and staphylococcus aureus. *Journal of biomedical materials research*, 52(4):662–668, 2000.

[60] SY Liau, DC Read, WJ Pugh, JR Furr, and AD Russell. Interaction of silver nitrate with readily identifiable groups: relationship to the antibacterialaction of silver ions. *Letters in applied microbiology*, 25(4):279–283, 1997.

[61] Sasha Stankovich, Dmitriy A Dikin, Geoffrey HB Dommett, Kevin M Kohlhaas, Eric J Zimney, Eric A Stach, Richard D Piner, SonBinh T Nguyen, and Rodney S Ruoff. Graphene-based composite materials. *nature*, 442 (7100):282, 2006.

[62] WGIU Rathnayake, H Ismail, A Baharin, AGND Darsanasiri, and Sanath Rajapakse. Synthesis and characterization of nano silver based natural rubber latex foam for imparting antibacterial and anti-fungal properties. *Polymer Testing*, 31(5):586–592, 2012.

[63] Catalina Marambio-Jones and Eric MV Hoek. A review of the antibacterial effects of silver nanomaterials and potential implications for human health and the environment. *Journal of Nanoparticle Research*, 12(5): 1531–1551, 2010.

[64] Xianghong Lou, Hui Pan, Shenmin Zhu, Chengling Zhu, Yongliang Liao, Yao Li, Di Zhang, and Zhixin Chen. Synthesis of silver nanoprisms on reduced graphene oxide for high-performance catalyst. *Catalysis Communications*, 69:43–47, 2015.

[65] Biraja C Dash and Henry C Hsia. 7 composite scaffolds for skin repair and regeneration. *Biomaterials for Skin Repair and Regeneration*, page 193, 2019.

[66] Harry F Tibbals. *Medical nanotechnology and nanomedicine*. CRC Press, 2010.

[67] Yousuke Moriuchi, Toshinobu Ishida, and Tadashi Kousai. Method of securing a catheter body to a human skin surface, March 6 1990. US Patent 4,906,233.

[68] Junyong Zhu, Jing Wang, Jingwei Hou, Yatao Zhang, Jindun Liu, and Bart Van der Bruggen. Graphene-based antimicrobial polymeric membranes: a review. *Journal of Materials Chemistry A*, 5(15):6776–6793, 2017.

[69] Renu Pasricha, Shweta Gupta, and Avanish Kumar Srivastava. A facile and novel synthesis of ag–graphene-based nanocomposites. *Small*, 5(20):2253–2259, 2009.

[70] Sen Liu, Jingqi Tian, Lei Wang, Hailong Li, Yingwei Zhang, and Xuping Sun. Stable aqueous dispersion of graphene nanosheets: noncovalent functionalization by a polymeric reducing agent and their subsequent decoration with ag nanoparticles for enzymeless hydrogen peroxide detection. *Macromolecules*, 43(23): 10078–10083, 2010.

[71] Peter W Hawkes. *Advances in imaging and electron physics*, volume 133. Elsevier, 2004.

[72] Vladislav Krzyzanek, Sebastian Tacke, N Sporenberg, Monika Schönhoff, and R Reichelt. Mass measurements using electron scattering employing an "in-lens" scanning electron microscope. 01 2012.

[73] Joseph I Goldstein, Dale E Newbury, Joseph R Michael, Nicholas WM Ritchie, John Henry J Scott, and David C Joy. *Scanning electron microscopy and X-ray microanalysis*. Springer, 2017.

[74] Douglas B Murphy. *Fundamentals of light microscopy and electronic imaging*. John Wiley & Sons, 2002.

[75] David B Williams, C Barry Carter, and C Transmission Electron Microscopy. A textbook for materials science. *Transmission Electron Microscope*, 2009.

[76] Ludwig Reimer. *Transmission electron microscopy: physics of image formation and microanalysis*, volume 36. Springer, 2013.

[77] Axel Lubk and Falk Röder. Semiclassical tem image formation in phase space. *Ultramicroscopy*, 151: 136–149, 2015.

[78] C Barry Carter and David B Williams. *Transmission electron microscopy: Diffraction, imaging, and spectrometry*. Springer, 2016.

[79] AT Rhys Williams. *An introduction to fluorescence spectroscopy*. Perkin-Elmer, 1981.

[80] Khan Maaz. *The Transmission Electron Microscope*. BoD–Books on Demand, 2012.

[81] Ewen Smith and Geoffrey Dent. *Modern Raman spectroscopy: a practical approach*. Wiley, 2019.

[82] John R Ferraro. *Introductory raman spectroscopy*. Elsevier, 2003.

[83] Richard L McCreery. *Raman spectroscopy for chemical analysis*, volume 225. John Wiley & Sons, 2005.

[84] Mohammad Jafari. *Application of Vibrational Spectroscopy in Organic Electronics*. PhD thesis, 11 2017.

[85] Andrea C Ferrari. Raman spectroscopy of graphene and graphite: disorder, electron–phonon coupling, doping and nonadiabatic effects. *Solid state communications*, 143(1-2):47–57, 2007.

[86] Stefan Wagner. 2d materials for piezoresistive strain gauges and membrane based nanoelectromechanical systems.

[87] Zhenhua Ni, Yingying Wang, Ting Yu, and Zexiang Shen. Raman spectroscopy and imaging of graphene. *Nano Research*, 1(4):273–291, 2008.

[88] Jukka A Räty, Kai-Erik Peiponen, and Toshimitsu Asakura. *UV-visible reflection spectroscopy of liquids*, volume 92. Springer Science & Business Media, 2004.

[89] Andrew M Ellis, Miklos Feher, and Timothy G Wright. *Electronic and photoelectron spectroscopy: fundamentals and case studies*. Cambridge University Press, 2005.

[90] Heinz-Helmut Perkampus. *UV-VIS Spectroscopy and its Applications*. Springer Science & Business Media, 2013.

[91] Challa SSR Kumar. *UV-VIS and photoluminescence spectroscopy for nanomaterials characterization*. Springer, 2013.

[92] Gustav Mie. A contribution to the optics of turbid media, especially colloidal metallic suspensions. *Ann. Phys*, 25(4):377–445, 1908.

[93] Nguyen Thi Lan, Do Thi Chi, Ngo Xuan Dinh, Nguyen Duy Hung, Hoang Lan, Pham Anh Tuan, Le Hong Thang, Nguyen Ngoc Trung, Nguyen Quang Hoa, Tran Quang Huy, Nguyen Van Quy, Thanh-Tung Duong, Vu Ngoc Phan, and Anh-Tuan Le. Photochemical decoration of silver nanoparticles on graphene oxide nanosheets and their optical characterization. *Journal of Alloys and Compounds*, 615:843–848, 2014.

[94] David Harvey. *Modern analytical chemistry*. McGraw-Hill, 2000.

[95] Daniel C Harris. *Quantitative chemical analysis*. Macmillan, 2010.

[96] Jan Hudzicki. Kirby-bauer disk diffusion susceptibility test protocol. 2009.

[97] James H Jorgensen and John D Turnidge. Susceptibility test methods: dilution and disk diffusion methods. In *Manual of Clinical Microbiology, Eleventh Edition*, pages 1253–1273. American Society of Microbiology, 2015.

[98] WM Kirby, GM Yoshihara, KS Sundsted, and JH Warren. Clinical usefulness of a single disc method for antibiotic sensitivity testing. *Antibiotics Annual*, page 892, 1956.

[99] Alfred W Bauer, David M Perr, and William MM Kirby. Single-disk antibiotic-sensitivity testing of staphylococci: An analysis of technique and results. *AMA archives of internal medicine*, 104(2):208–216, 1959.

[100] L Barth Reller, Melvin Weinstein, James H Jorgensen, and Mary Jane Ferraro. Antimicrobial susceptibility testing: a review of general principles and contemporary practices. *Clinical infectious diseases*, 49(11): 1749–1755, 2009.

[101] Luis Vidal Salgado and Carlos Vargas Hernández. Medición de la absorbancia óptica de soluciones acuosas mediante la instrumentación virtual y el control. *Scientia et technica*, 19(1):49–53, 2014.

[102] Jose Ruben Morones, Jose Luis Elechiguerra, Alejandra Camacho, Katherine Holt, Juan B Kouri, Jose Tapia Ramírez, and Miguel Jose Yacaman. The bactericidal effect of silver nanoparticles. *Nanotechnology*, 16(10): 2346, 2005.

[103] Jacques Monod. The growth of bacterial cultures. *Annual review of microbiology*, 3(1):371–394, 1949.

[104] MH Zwietering, Il Jongenburger, FM Rombouts, and K Van't Riet. Modeling of the bacterial growth curve. *Appl. Environ. Microbiol.*, 56(6):1875–1881, 1990.

[105] Abalonyx. Graphene Oxide and Reduced Graphene Oxide Products for Sale product series, 2013. URL http://www.abalonyx.no/products.42023.en.html.

[106] Santiago Vispo. Combinatoria molecular. *Centro de Ingeniería Genética y Biotecnología*, 2004.

[107] V Germain, Jing Li, D Ingert, ZL Wang, and MP Pileni. Stacking faults in formation of silver nanodisks. *The Journal of Physical Chemistry B*, 107(34):8717–8720, 2003.

[108] Marek Grzelczak and Luis M Liz-Marzán. The relevance of light in the formation of colloidal metal nanoparticles. *Chemical Society Reviews*, 43(7):2089–2097, 2014.

[109] Túlio CR Rocha, Herbert Winnischofer, Eduard Westphal, and Daniela Zanchet. Formation kinetics of silver triangular nanoplates. *The Journal of Physical Chemistry C*, 111(7):2885–2891, 2007.

[110] Yeonjoo Bae, Nam Hoon Kim, Minjung Kim, Kang Yeol Lee, and Sang Woo Han. Anisotropic assembly of ag nanoprisms. *Journal of the American Chemical Society*, 130(16):5432–5433, 2008.

[111] Rongchao Jin, Y Charles Cao, Encai Hao, Gabriella S Métraux, George C Schatz, and Chad A Mirkin. Controlling anisotropic nanoparticle growth through plasmon excitation. *Nature*, 425(6957):487, 2003.

[112] Li Liu, Sunmin Ryu, Michelle R Tomasik, Elena Stolyarova, Naeyoung Jung, Mark S Hybertsen, Michael L Steigerwald, Louis E Brus, and George W Flynn. Graphene oxidation: thickness-dependent etching and strong chemical doping. *Nano letters*, 8(7):1965–1970, 2008.

[113] Zhe Zhang, Fugang Xu, Wenshu Yang, Mingyi Guo, Xiaodan Wang, Bailin Zhang, and Jilin Tang. A facile one-pot method to high-quality ag-graphene composite nanosheets for efficient surface-enhanced raman scattering. *Chemical Communications*, 47(22):6440–6442, 2011.

[114] Sergi Claramunt, Aïda Varea, David López-Díaz, M Mercedes Velázquez, Albert Cornet, and Albert Cirera. The importance of interbands on the interpretation of the raman spectrum of graphene oxide. *The Journal of Physical Chemistry C*, 119(18):10123–10129, 2015.

[115] Xiangping Li, Haoran Ren, Xi Chen, Juan Liu, Qin Li, Chengmingyue Li, Gaolei Xue, Jia Jia, Liangcai Cao, Amit Sahu, Bin Hu, Yongtian Wang, Guofan Jin, and Min Gu. Athermally photoreduced graphene oxides for three-dimensional holographic images. *Nature Communications*, 6:6984, 2015.

[116] Régis YN Gengler, Daniel S Badali, Dongfang Zhang, Konstantinos Dimos, Konstantinos Spyrou, Dimitrios Gournis, and RJ Dwayne Miller. Revealing the ultrafast process behind the photoreduction of graphene oxide. *Nature communications*, 4(1):1–5, 2013.

[117] Amanda J Haes, Christy L Haynes, and Richard P Van Duyne. Nanosphere lithography: self-assembled photonic and magnetic materials. *MRS Online Proceedings Library Archive*, 636, 2000.

[118] Prajwal Chettri and Archana Tiwari. Tuning photoluminescence quenching efficiency of reduced graphene oxide substrates using silver nanoparticles. *Thin Solid Films*, 669:208–214, 2019.

[119] Oleg A Yeshchenko, Igor M Dmitruk, Alexandr A Alexeenko, Mykhaylo Yu Losytskyy, Andriy V Kotko, and Anatoliy O Pinchuk. Size-dependent surface-plasmon-enhanced photoluminescence from silver nanoparticles embedded in silica. *Physical Review B*, 79(23):235438, 2009.

[120] Peter Apell, R Monreal, and Stig Lundqvist. Photoluminescence of noble metals. *Physica Scripta*, 38(2):174, 1988.

[121] S Vijay Kumar, NM Huang, HN Lim, AR Marlinda, I Harrison, and Chin Hua Chia. One-step size-controlled synthesis of functional graphene oxide/silver nanocomposites at room temperature. *Chemical Engineering Journal*, 219:217–224, 2013.